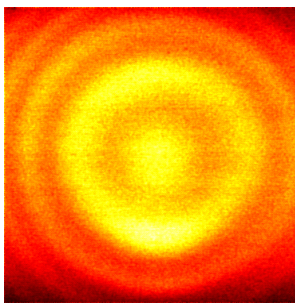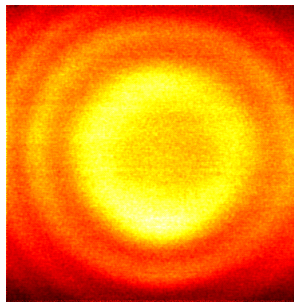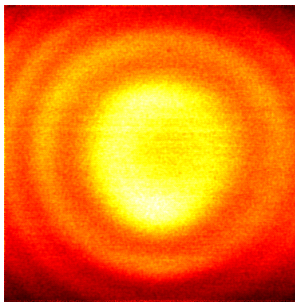# Fiber-based Implementations of Coherent anti-Stokes Raman Scattering Microspectroscopy and Microscopy
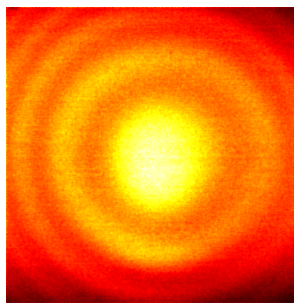
Esben Ravn Andresen
Department of Physics and Astronomy,
University of Aarhus, Denmark

PhD thesis
July, 2007

This thesis is submitted to the Faculty of Science at the University of Aarhus, Denmark, in order to fulfill the requirements for obtaining the PhD degree in Physics. The studies have been carried out at the Department of Physics and Astronomy under the supervision of Prof. Søren Keiding.
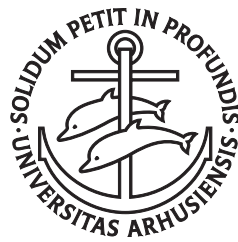
List of publications

This thesis is based on the following publications:

Articles in journals

Esben Ravn Andresen, Henrik Nørgaard Paulsen, Victoria Birkedal, Jan Thøgersen, and Søren Rud Keiding. Broadband multiplex coherent anti-Stokes Raman scattering microscopy employing photonic crystal fibers. *J. Opt. Soc. Am. B*, 22(9):1934–1938, 2005a.

Esben Ravn Andresen, Jan Thøgersen, and Søren Rud Keiding. Spectral compression of femtosecond pulses in photonic crystal fibers. *Opt. Lett.*, 30(15):2025–2027, 2005b.

Esben Ravn Andresen, Victoria Birkedal, Jan Thøgersen, and Søren Rud Keiding. Tunable light source for coherent anti-Stokes Raman scattering microspectroscopy based on the soliton self-frequency shift. *Opt. Lett.*, 31(9):1328–1330, 2006a.

Esben Ravn Andresen, Søren Rud Keiding, and Eric Olaf Potma. Picosecond anti-Stokes generation in a photonic-crystal fiber for interferometric CARS microscopy. *Opt. Exp.*, 14(16):7246–7251, 2006b.

Vishnu Vardhan Krishnamachari, Esben Ravn Andresen, Søren Rud Keiding, and Eric Olaf Potma. An active interferometer-stabilization scheme with linear phase control. *Opt. Exp.*, 14(12):5210–5215, 2006.

Esben Ravn Andresen, Carsten Krogh Nielsen, Jan Thøgersen, and Søren Rud Keiding. Fiber laser-based light source for coherent anti-Stokes Raman scattering microspectroscopy. *Opt. Exp.*, 15(8):4848–4856, 2007.

Conference contributions

Esben Ravn Andresen, Henrik Nørgaard Paulsen, Victoria Birkedal, Jan Thøgersen, and Søren Rud Keiding. Coherent anti-Stokes Raman

scattering microscopy implemented with two photonic-crystal fibers. *presented at CLEO/EQEC Europe, Munich*, 2005.

Esben Ravn Andresen, Carsten Krogh Nielsen, Jan Thøgersen, and Søren Rud Keiding. Fiber laser-based light source for coherent anti-Stokes Raman scattering microspectroscopy. *presented at European Conference on Biomedial Optics, Munich*, 2007a.

Esben Ravn Andresen, Carsten Krogh Nielsen, Jan Thøgersen, and Søren Rud Keiding. Photonic-crystal fibers and fiber lasers as light sources in CARS microspectroscopy. *presented at Focus on Microscopy, Valencia*, 2007b.

Contents

Abstract

Dansk resume

Det centrale tema i denne afhandling er CARS mikrospektroskopi, hvormed det er muligt at danne tre-dimensionelle billeder af en prøves kemiske sammensætning. Det ene emne er udvikling af nye lyskilder til CARS mikrospektroskopi baseret på fiberlasere og en ny type optiske fibre kaldet fotoniske krystalfibre, hvis specielle egenskaber anvendes til frekvenskonvertering af laserpulser. Det andet emne er udvikling af såkaldte interferometriske detektionsteknikker, hvormed følsomheden af CARS mikrospektroskopi kan forbedres. Der udvikles dels en specialiseret stabiliseringsmetode hertil, dels en detektionsteknik, der anvender en fotonisk krystalfiber.

English summary

The central theme in this thesis is CARS microspectroscopy, which makes it possible to form three-dimensional images of the chemical composition of a sample. One subject is the development of new light sources for CARS microspectroscopy based on fiber lasers and a new class of optical fibers called photonic-crystal fibers, whose unique properties are employed to frequency-convert laser pulses. The second subject is the development of so-called interferometric detection techniques, by which is it possible to increase the sensitivity of CARS microspectroscopy. A specialized stabilization scheme for this is developed, as is a detection technique, which uses a photonic-crystal fiber.

Part I

Introduction

Chapter 1

Introduction and outline

1.1 Introduction

The optical microscope has long been the work-horse in many fields of science such as medicine and biology. And although the principle of the microscope has remained the same, a plethora of variations in illumination parameters, sample labelling, and detection techniques have been devised, so that a microscope can to a high degree be optimized towards a very specific application.

CARS microscopy is one example of such a variation optimized for a niche of microscopy applications where one is interested in local chemical information about a sample. CARS microscopy achieves this because the spectroscopic CARS signal is sensitive to Raman-active vibrations. That chemical information can be obtained owes to the fact that molecules have distinct sets of vibration frequencies. Illumination is done by two laser pulse trains of different colour, and the detector measures the intensity of the generated spectroscopic CARS signal in the sample.

At the onset of the present PhD-project in 2003, it had been four years since the CARS microscope in its present form (using two collinear, tightly focussed laser pulse trains) had been realized (Zumbusch et al., 1999). The major challenges posed at that point to researchers in the field were i) to demonstrate that the technique could actually live up to its promise to deliver images from which chemical information could be unequivocally derived; and ii) to develop laser systems that were optimized for CARS microscopy.

The field of has continued to evolve to this day. From the application point of view, CARS imaging has proven useful for some problems that are difficult to adress by other means. It is striking that the single most important driving force in this evolution has not so much

been the improved understanding of the physical principles (because CARS spectroscopy is already well-understood and a widely used laser spectroscopic technique), as it has been the developments in laser technology. Especially the technology to inter-lock the repetition rate of two pulsed lasers (Potma et al., 2002) and the development of easily-tunable synchronously pumped optical parametric oscillators (OPO)s (Ganikhanov et al., 2006) have been major contributing factors.

In the author's view, the two challenges i) and ii) still stand, although in slightly different formulations. With regards to i), although it has been demonstrated numerous times that chemical imaging with CARS microscopy is indeed possible, the results have mostly been of qualitative nature. It remains a challenge to derive information about the quantities of the chemical species in the sample under study and do so without *a priori* knowledge. So this is something that should be adressed, either by developing new methods for data analysis or new detection techniques. With regards to ii), although new laser systems have been developed that are virtually optimal laser systems for CARS microscopy, they remain costly. So, the next challenge for laser technology would be to develop simpler, more compact, and cheaper light sources that can pave the way for a wider spread of CARS microscopes. If this could be realized, it is possible, that the functionality of CARS microscopy could be integrated in commercial microscopes along with other functionalities such as fluorescence microscopy.

In recent years, two other fields have attracted interest, namely photonic-crystal fibers (PCF)s and fiber lasers. PCFs because of their unique frequency converting properties at visible wavelengths and the fact that modern production technology has made it possible to precisely engineer these properties in a reproducible way (Russell, 2003). And fiber lasers because of their environmentally stable operation, compactness, and the possibility to scale them to high powers (Limpert et al., 2006). Both these fields are very active at the moment and could, potentially, comprise the next developments in laser technology, that will drive the spread of CARS microscopy.

1.2   Outline of the thesis

The main aim of this thesis is to address challenge ii), *i.e.* investigate different means of realizing simple, compact, and potentially low-cost light sources based on PCFs and fiber lasers. To some degree, challenge i) of quantitative detection techniques will also be addressed. The thesis is divided into four parts.

In the introduction part, Chap. 2 will give an overview of the theoretical basis for the thesis. Chapter 3 reviews the relevant elements of

the field and accounts for motivations and challenges.

Part 2 concerns my work done at Aarhus University about different aspects of light sources that employ PCFs and use a single laser (either a Ti:sapphire laser or a fiber laser) as the initial illumination source; chapters 4 and 5 describe the utilization of PCFs for spectrally tailoring and spectrally shifting laser pulses, to generate laser light with parameters more suitable for CARS than the laser itself delivers. The following chapters describe actual implementations of PCF-based light-conversion in CARS microspectroscopy based on a single Ti:sapphire laser (Chap. 6) and a single, home-built ytterbium fiber laser (Chap. 7).

Part 3 describes my work done during a three-month stay at the University of California Irvine on a stabilization scheme suitable for interferometrically-detected CARS microscopy and an alternative means of generating a reference pulse by four-wave mixing (FWM) in a PCF.

The final part will conclude and discuss perspectives.

Chapter 2

Theory

2.1 Introduction

Everyday physical phenomena like refraction at interfaces and absorption in a pint of Guiness are examples of linear material responses to optical fields. When pulsed lasers with high peak powers became available, they paved the way for the exploration of a realm of optics beyond linear optics where material responses depend on the magnitude of the optical field; nonlinear optics. The main new thing about that is that light can now interact with light through a material response, transferring energy between different colours and even generating new ones. Nonlinear optics is important in laser technology, where it facilitates different-coloured laser light. Also, many new kinds of spectroscopy have been developed. The field of nonlinear optics is vast and embodies many interesting and useful phenomena. In spite of the difference of these phenomena, physically, all the nonlinear effects are similar.

In this chapter, effects which can be described as purely nonlinear effects will be described: self-phase modulation (SPM), CARS, and the Raman effect. Effects that must be explained by an interplay between linear and nonlinear effects will also be described: phase-matched four-wave mixing (FWM) and solitons.

Light fields

To keep a consistent nomenclature throughout, the description of the i'th electromagnetic fields will be stated as

$$E_i(z,t) = \tilde{E}_i(z,t)e^{i\beta(\omega_i)z - i\omega_i t} + cc. \qquad (2.1)$$

$\tilde{E}_i(z,t)$ is then the complex, slowly-varying envelope of the i'th field, β its propagation constant, z the position coordinate, ω_i its central angular frequency, and t the time coordinate. We will always be considering

pulsed fields, *i.e.*, the slowly-varying envelope is written for a Gaussian pulse as *e.g.*

$$\tilde{E}(t) = E_0 e^{-2\ln 2 \frac{t^2}{\tau_{fwhm}^2}}, \tag{2.2}$$

where τ_{fwhm} is is the pulse duration full width at half-maximum (FWHM) of $|E|^2$, *i.e.* of the intensity envelope. Another pulse shape often encountered is the hyperbolic-secant, which is the shape that solitons take,

$$\tilde{E}(t) = E_0 \text{sech}(\frac{2\ln(1+\sqrt{2})t}{\tau_{fwhm}}). \tag{2.3}$$

In this thesis, pulse shapes will be assumed to be Gaussian unless otherwise noted. In nonlinear optics, it is useful to describe the total field $E(z,t)$ as a sum of several individual fields $E_i(z,t)$ which oscillate at frequency ω_i

$$E(z,t) = \sum_i E_i(z,t). \tag{2.4}$$

In some cases, the pulse envelope will be so long (spectrally narrow) that the pulses for all practical purposes can be thought of as composed of only a single frequency, *i.e.* as a δ-function in frequency. These pulses will be referred to as quasi-monochromatic. We will be working with scalar fields and thus always assume that all fields have the same polarization. Likewise, the position coordinate and propagation constant will be treated as a scalar, implying collinear propagation of all beams. In some cases, the position or time dependence of the fields is irrelevant, in those cases, the dependence will just be omitted from the expression.

2.2 The wave equation

From the Maxwell equations, the wave equation in a polarizable material can be obtained as(Jackson, 1998).

$$-\frac{\partial^2}{\partial z^2} E(z,t) + \frac{1}{c^2} \frac{\partial^2 E(z,t)}{\partial t^2} = -\mu_0 \frac{\partial^2 P(z,t)}{\partial t^2}, \tag{2.5}$$

where $P(z,t)$ is the material polarization induced by the field. The prerequisite for solving Eq. 2.5 is that the material polarization, $P(z,t)$, is known. Of course, the fields in Eq. 2.1 are solutions to Eq. 2.5. The wave equation Eq. 2.5 describes any field propagation in any material. It is the centerpiece of this chapter, where it will be used to describe the signal field generation in CARS (Sec. 2.3) as well as nonlinear pulse propagation in optical fibers (Sec. 2.5).

It is conventional to introduce the optical susceptibility, χ, which is a material parameter that describes, how a material responds to

an electromagnetic field, *i.e.* which polarization a field induces. The n'th order $\chi^{(n)}$ determines the n'th order polarization response of the material, so $\chi^{(1)}$ is responsible for linear and $\chi^{(3)}$ for nonlinear optics. In principle, all higher-order terms encompass nonlinear optics, but in the present context, truncation at third order is sufficient, and the second-order will be assumed to be zero because we restrict ourselves to the isotropic case.

Linear response

For weak fields, it is sufficient to truncate the susceptibility at first order, $\chi \to \chi^{(1)}$. For weak fields, only the linear polarization, $P^{(1)}(z,t)$, contributes to the total polarization, defined as (Mukamel, 1995)

$$P^{(1)}(z,\omega) = \epsilon_0 \chi^{(1)}(\omega) E(z,\omega). \qquad (2.6)$$

The linear, first-order term $\chi^{(1)}(\omega)$ accounts for the refractive index $n(\omega)$ and the absorption $\alpha(\omega)$ through the relations (Agrawal, 1995)

$$n(\omega) = 1 + \frac{1}{2}\text{Re}[\chi^{(1)}(\omega)] \qquad (2.7)$$

$$\alpha(\omega) = \frac{\omega}{nc}\text{Im}[\chi^{(1)}(\omega)]. \qquad (2.8)$$

The propagation constant is related to the refractive index by $\beta(\omega) = (n(\omega)\omega/c)$.

Dispersion

In the propagation of electromagnetic radiation in matter with material resonances, the radiation experiences a frequency-dependent phase shift that is caused by the cumulative effect of all resonances. It is manifested through $n(\omega)$ and is generally frequency-dependent. Equation 2.5 has solution $E_0(z,t) = \tilde{E}_0 e^{i\beta(\omega)z - i\omega_0 t}$, where ω_0 is the center frequency and $\beta(\omega)$ the propagation constant which, because of dispersion,is a function of frequency. It is commonplace to expand $\beta(\omega)$ in the angular frequency ω about the center frequency ω_0

$$\beta(\omega) = \beta_0 + \beta_1(\omega - \omega_0) + \frac{1}{2}\beta_2(\omega - \omega_0)^2 + \dots, \qquad (2.9)$$

where $\beta_n = \partial^n \beta(\omega)/\partial\omega^n$. The zeroth-order term determines the phase velocity, $v_\phi = \omega/\beta_0$; it can be understood as the propagation velocity of an electromagnetic "wave top". The first-order term determines the group velocity, $v_g = \beta_1^{-1}$; it can be understood as the propagation velocity of the pulse envelope. The second-order term, β_2 denotes

the group-velocity dispersion (GVD), and is responsible for chirp, *i.e.* the stretching of a pulse in time while at the same time dispersing its frequency components in time. A chirped pulse envelope is sometimes written using the chirp parameter, α, so that, for a chirped Gaussian pulse,

$$\tilde{E}(t) = E_0 e^{-2\ln 2(1+i\alpha)\frac{t^2}{\tau_{fwhm}^2}}. \tag{2.10}$$

A pulse experiencing in a material with $\beta_2 > 0$ (normal GVD) becomes positively chirped ($\alpha < 0$), so the low frequency components are on the leading edge and the blue on the trailing edge. If $\beta_2 < 0$ (anomalous GVD), the pulse becomes negatively chirped, so $\alpha > 0$ and the blue componenents are on the leading edge. Orders of β higher than 2 are typically referred to under one as higher-order dispersion (HOD).

Nonlinear response

The lowest order of a nonlinear polarization would be the second order. The second-order polarization flips sign under the space inversion operation. We will restrict ourselves to isotropic materials, in which the polarization must be invariant under space inversion. The second-order polarization must thus be zero, and we can proceed to the third order.

   The third-order polarization is defined, analogously to Eq. 2.6, as

$$P^{(3)}(z,\omega) = \epsilon_0 \chi^{(3)}(\omega; \omega_k, \omega_l, \omega_m) E_k(z,\omega_k) E_l(z,\omega_l) E_m(z,\omega_m) \tag{2.11}$$

with the condition $\omega = \omega_k + \omega_l + \omega_m$. Note, Eq. 2.11 has been given for quasi-monochromatic case. In the case of spectrally broad fields, integration over frequency is nessecary to obtain the entire polarization at all frequencies. Also, the E's are a complex number plus its complex conjugate. The tensorial nature of $\chi^{(3)}$ has been left out, because we are only dealing with scalar fields.

   $\chi^{(1)}$ has already been related to the refractive index and absorption coefficient. Initially, to obtain the nonlinear response, we could just generalize the refractive index and the absorption coefficients, introducing the nonlinear refractive index and nonlinear absorption coefficient, n_2 and α_2. $n \rightarrow n + n_2|E|^2$ and $\alpha \rightarrow \alpha + \alpha_2|E|^2$, this gives

$$n_2 = \frac{3}{8n}\text{Re}(\chi^{(3)})|E|^2 \tag{2.12}$$

$$\alpha_2 = \frac{3\omega_0}{4nc}\text{Im}(\chi^{(3)})|E|^2, \tag{2.13}$$

which is applicable in many cases. It should only be used in the case where there are no material resonances, though. A somewhat deeper methodology for calculating nonlinear response and $\chi^{(3)}$ in the presence of material resonances will be given next.
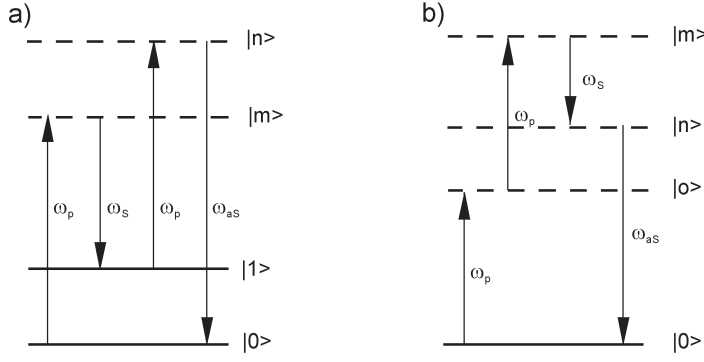
Figure 2.1: (a) Level diagram of the resonant CARS process. $|1\rangle$ is a Raman-active level and $|0\rangle$ the ground level; (b) level diagram of the nonresonant CARS process. The dashed lines at $|m\rangle$, $|n\rangle$, and $|o\rangle$ represent virtual levels.

2.3 Calculating the fields

Resonant CARS

CARS is an example of a third-order nonlinear process, where 2 interactions with a "pump" (p) field and one with a "Stokes" (S) field take place, generating an anti-Stokes (aS) field. Figure 2.1a exemplifies the excitation scheme and the levels involved in CARS spectroscopy. (The diagram is simplistic as it is not possible to discern coherent excitation from population transfer.) The calculation of the third-order susceptibility responsible for CARS is relatively simple. The resonant CARS susceptibility is

$$\chi^{(3)}(-\omega_{aS}; \omega_p, -\omega_S, \omega_p) = \sum_j \frac{A_j}{\Omega_{j0} - (\omega_p - \omega_S) + i\Gamma_{j0}}. \qquad (2.14)$$

Since only one (two-photon) resonance is involved, the expression for $\chi^{(3)}$ resembles that obtained for a one-photon process. In the case of quasi-monochromatic pump and Stokes fields, the expression for the CARS signal becomes very simple in frequency space

$$S_{aS}(\omega_{aS}) = |\chi^{(3)}(-\omega_{aS}; \omega_p, -\omega_S, \omega_p)|^2 I_p^2(\omega_p) I_S(\omega_S). \qquad (2.15)$$

This expression is also valid for long (ps-) pulses.

Another important case is when the first and third interaction fields are long pulses and can be considered δ-functions in frequency. Then

$$S_{aS}(\omega_{aS}) \propto |\chi^{(3)}(-\omega_{aS}; \omega_p, -\omega_S, \omega_p)|^2 I_S(\omega_S). \qquad (2.16)$$

This case is commonly known as muliplex-CARS (MCARS) or CARS microspectroscopy.

Nonresonant CARS

Figure 2.1b is an example of a nonlinear process that also produces a signal at the same CARS frequency as the resonant process in Fig. 2.1a. At this point, a distinction should be made between two types of signal, that can be produced at the CARS wavelength. The resonant CARS signal is that, where a Raman-active level is involved. This means, that only a certain permutation of the time-ordering of the fields results in resonant signal. On the other hand, nonresonant signal does not have to fulfill this requirement. Therefore, there are many more permutations of the fields that produce nonresonant signal than resonant. So even though nonresonant signals are generally weaker than resonant signals, in CARS, nonresonant signal can be very significant for the mere fact that there are many contributions. Because the nonresonant CARS signal has (almost) no dependence of molecular levels (no frequency dependence), the nonresonant susceptibility $\chi_{nr}^{(3)}$ is usually represented as a real number,

$$\chi_{nr}^{(3)} = \text{realnumber}. \tag{2.17}$$

The total signal at the CARS frequency including nonresonant signal is then, again assuming quasi-monochromatic fields

$$S_{aS}(\omega_{aS}) = |\chi_{nr}^{(3)} + \chi^{(3)}(-\omega_{aS}; \omega_p, -\omega_S, \omega_p)|^2 I_p^2(\omega_p) I_S(\omega_S). \tag{2.18}$$

2.4 A more general description

Above, the nonlinear polarization was calculated under the assumption that the material response represented as $\chi^{(3)}$ or n_2 was known and that the excitation fields could be described as quasi-monochromatic. To describe and understand CARS signal generation with complex pump and Stokes pulses *e.g.* phase-tailoured pulses, it is useful to think in terms of a more general description. To evaluate $P^{(3)}$, one has to look quantum-mechanically at the interaction between light and an ensemble of molecules. This interaction is governed by the Liouville equation (Mukamel, 1995)

$$\frac{\partial}{\partial t}\rho = -\frac{i}{\hbar}[H_0, \rho] - \frac{i}{\hbar}[H_{int}, \rho] + \frac{\partial}{\partial t}\rho|_{relax}. \tag{2.19}$$

H_0 is the unperturbed Hamiltonian and H_{int} is the perturbation Hamiltonian in the interaction picture. The last term represents relaxation

processes, due to which, the system relaxes towards an equilibrium state. ρ is the density matrix, given as (Sakurai, 1994)

$$\rho_{nm} = c_n c_m^* |\phi_n\rangle\langle\phi_m| \tag{2.20}$$

c_i and $|\phi_i\rangle$ are the propability amplitudes and eigenstates, respectively. It is required to work within the framework of the density operator to account for dephasing and fully incorporate coherent effects, which are needed to fully describe CARS - a fundamentally coherent process. Here, Eq. 2.19 is solved perturbatively. ρ is expanded as

$$\rho(t) = \rho^{(0)}(t) + \rho^{(1)}(t) + \rho^{(2)}(t) + \rho^{(3)}(t) + \dots. \tag{2.21}$$

From $\rho^{(3)}(t)$, the expression for $P^{(3)}$ can be found:

$$P^{(3)}(t) = \mathrm{Tr}(V\rho^{(3)}(t)), \tag{2.22}$$

where V is a matrix that contains the dipole moments μ between all the involved levels and Tr denotes the trace. Equation 2.19 can be recast, matching perturbative orders p,

$$\rho_{nm}^{(p+1)}(t) = I_{nm}(t) \otimes [E(t) \sum_l (\mu_{nl}\rho_{lm}^{(p)}(t) - \rho_{nl}^{(p)}(t)\mu_{lm})]. \tag{2.23}$$

Where

$$I_{\nu\nu'}(t) = \theta(t)\exp(-i\Omega_{\nu\nu'}t - \Gamma_{\nu\nu'}t), \tag{2.24}$$

and $\theta(t)$ is the Heaviside step-function. In frequency space, it is

$$I_{\nu\nu'}(\omega) = \frac{1}{\omega - \Omega_{\nu\nu'} + i\Gamma_{\nu\nu'}} \tag{2.25}$$

The quantity $1/\Gamma_{\nu\nu'}$ is called the decoherence time of the vibration. In frequency space, $\Gamma_{\nu\nu'}$ is the spectral linewidth (half-width at half-maximum). As it stands in Eq. 2.23, the Liouville equation lends itself to a somewhat intuitive interpretation. To describe a nonlinear interaction between a light field and matter, we let the density matrix start out in a known, unperturbed state, *e.g.* $\rho_{aa}^{(0)} = 1$. Each interaction with a light field raises the order of perturbation by one and contributes one μ and one I to the response function following the pattern:

$$\rho_{aa}^{(0)} \xrightarrow{\mu_{ab}I_{ab}} \rho_{ab}^{(1)} \xrightarrow{\mu_{bc}I_{ac}} \rho_{ac}^{(2)} \xrightarrow{\mu_{cd}I_{ad}} \rho_{ad}^{(3)}$$

The dipole moments, μ, represent the coupling strength between different levels, while the I-functions represent the time evolution of the density matrix. It is generally not enough to do this drill just once. In general, there are many "quantum pathways" like the one exemplified above. Then, one must draw Feynmann diagrams of the interaction

and determine, which ones contribute to the $\rho^{(3)}_{\nu\nu'}$ that one is considering. The rotating-wave approximation (RWA) can be used to determine which field, or its conjugate, should be used in the interaction. Further, it can be realized that the convolution of two functions in time space is the same as multiplying them in frequency space (Press et al., 1992), such that

$$f(t) \otimes g(t) = \mathrm{FT}^{-1}(\mathrm{FT}(f(t)) \cdot \mathrm{FT}(g(t))), \qquad (2.26)$$

which makes it easier to calculate $\rho^{(3)}$ on a computer. And, using Eq. 2.23, the excitation pulses can have complex shapes, *i.e.* be spectrally broad and have non-constant phase (for example chirp). All this is information is contained in the complex, slowly-varying envelope. A Matlab script was written that calculates CARS spectra using equations 2.23 and 2.26 (App. B).

CARS revisited

A more insightful description of CARS based on the level diagram in Fig. 2.1 can now be given. The system starts out in the ground state, $\rho^{(0)}_{00} = 1$, and "ends" in the coherence state, $\rho^{(3)}_{0n}$. One quantum pathway for a CARS process would be (again using the simplified notion of virtual levels, $|m\rangle$ and $|n\rangle$).

$$\rho^{(0)}_{00} \quad \xrightarrow{\mu_{0m}I_{0m}} \quad \rho^{(1)}_{0m} \quad \xrightarrow{\mu_{m1}I_{01}} \quad \rho^{(2)}_{01} \quad \xrightarrow{\mu_{1n}I_{0n}} \quad \rho^{(3)}_{0n}$$

The μ's can be omitted, if one is only interested in the shape of the field (spectrally or temporally) after the interaction. The process of calculating the CARS field is then to assume $\rho^{(0)}_{00} = 1$ and use Eq. 2.23 3 times to calculate $\rho^{(1)}_{0m}$, then $\rho^{(2)}_{01}$, then $\rho^{(3)}_{0n}$. If the field shape rather than the magnitude is interesting, the trace can be omitted, and the nonlinear polarization is just

$$P^{(3)} = \rho^{(3)}_{0n} \qquad (2.27)$$

(Of course, there is an equivalent quantum pathway, where the fields act on the bra side. That will give the contribution of the complex conjugate to the final polarization, to ensure it is real.) Once $P^{(3)}$ is known, the field, it induces, is calculated from the wave equation, Eq. 2.5. The interaction is assumed to occur on a short length scale, so the $\partial^2/\partial z^2$-term can be omitted:

$$\frac{1}{c^2}\frac{\partial^2 E(t)}{\partial t^2} = -\mu_0 \frac{\partial^2 P(t)}{\partial t^2} \qquad (2.28)$$

The third-order polarization is then written as

$$P^{(3)}(t) \quad \propto \quad \int_0^\infty dt_3 \int_0^\infty dt_2 \int_0^\infty dt_1 \delta(t_3)\exp(-i\omega_{10}t_2 - i\Gamma_{10}t_2)\delta(t_1)$$

$$\times E(t-t_3)E(t-t_3-t_2)E(t-t_3-t_2-t_1). \qquad (2.29)$$

The integrations over t_1 and t_3 are trivial and can be performed first, yielding

$$
\begin{aligned}
P^{(3)}(t) \quad \propto \quad & \int_0^\infty dt_2 \exp(-i\omega_{10}t_2 - \Gamma_{10}t_2) \\
& \times E(t)E(t-t_2)E(t-t_2). \qquad (2.30)
\end{aligned}
$$

The t_2 is then integrated out, and $P^{(3)}(t)$ will oscillate with the sum of the three participating field frequencies.

Nonresonant CARS revisited

Suppose that in the material-field interaction, there are no resonances that coincide in frequency with the field frequency. The RWA can not be invoked in this case. So, in principle, we should consider the contribution from all levels. However, the interaction is highly nonresonant, which means that the "decay time" is short (the decoherence time is inversely proportional to the detuning). This is the case for all the off-resonance interactions. So, this can be implemented in the response function by letting the I contributed from a nonresonant process be a δ-function in time. A nonresonant process can thus be envisioned as a "resonant" process with a "virtual level", which decays infinitely fast that is, it is only present when a field is present. $I_{\nu\nu'}(t) \propto \delta(t)$.

In the special case that there are no resonances at all in the 3 interactions, the response function is proportional to $\delta(t_1)\delta(t_2)\delta(t_3)$, and consequently, upon performing the integration of Eq. 2.30,

$$P^{(3)} \propto E_p^2 E_S^*. \qquad (2.31)$$

2.5 Nonlinear optics in fibers

Nonlinear optics in optical fibers is not phenomenologically different from CARS spectroscopy which is described above. The wave equation Eq. 2.5 also governs the evolution of the field in fibers. The calculation of the nonlinear polarization in the fiber is greatly simplified, because at optical frequencies, there are no material resonances. That means that the nonlinear response can be treated as instantaneous, just like the nonresonant processes described in the previous section. This also means that it is never required to invoke the RWA or discuss quantum pathways. The big methodological difference is that the length of material-field interaction is now finite, so that an integration over distance is required to obtain the final field.

Helmholtz equation

In the frequency domain, and truncating χ at first order, the generalisation to 3 dimensions of Eq. 2.5 becomes (Jackson, 1998)

$$\nabla^2 E(\mathbf{r}, \omega) = -\epsilon(\omega)\frac{\omega^2}{c^2}E(\mathbf{r}, \omega), \qquad (2.32)$$

where $\epsilon(\omega) = 1 + \chi^{(1)}(\omega)$. $\chi^{(3)}$ can be included later as a perturbation. With the choice of propagation along the z-axis, the field can be written as $E(\mathbf{r}, \omega) = F(x,y)\tilde{E}(z,\omega)e^{i(\beta_0 z) - i\omega t}$, where the slowly-varying envelope, $\tilde{E}$, is introduced. Then the wave equation can be written as two separate differential equations (Agrawal, 1995)

$$(\frac{\partial^2}{\partial x^2} + \frac{\partial^2}{\partial y^2})F(x,y) + n^2(\omega)\frac{\omega^2}{c^2}F(x,y) \;=\; \beta^2(\omega)F(x,y) \quad (2.33)$$

$$2i\beta_0\frac{\partial}{\partial z}\tilde{E}(z,\omega) + 2\beta_0(\beta(\omega) - \beta_0)\tilde{E}(z,\omega) \;=\; 0 \qquad (2.34)$$

The first equation is the Helmholtz equation, an eigenvalue problem, and $\beta(\omega)$ is the eigenvalue. This equation must just be solved once and for all to yield the eigenvalues $\beta(\omega)$ and the transverse eigenmodes $F(x,y)$. Then $\beta_0 = \beta(\omega_0)$ is determined, and the second equation, which governs pulse propagation (*i.e.* the evolution of the slowly-varying envelope), can be solved. In practice, $\beta(\omega)$ is measured rather than calculated. Here, we restrict ourselved to single-mode fibers (SMF), which means there is only one eigenmode with one corresponding $\beta(\omega)$ in which the field can propagate inside the fiber.

Nonlinearities are included through standard first-order perturbation theory. Thus, the solutions $F(x,y)$ are assumed not to change, while the eigenvalues, $\beta(\omega)$ do. Then, we split n into a linear and a nonlinear term $n^2 \rightarrow (n + \Delta n)^2 \approx n^2 + 2n\Delta n$, where $\Delta n = 3/(8n)\mathrm{Re}\chi^{(3)}|E|^2 = n_2|E|^2$. The far-from-resonance condition is invoked, then $\chi^{(3)}$ is just a real number (in accordance with Eq. 2.31). Here, absorption can be neglected because we are always working with short fibers. Then $\beta(\omega) \rightarrow \beta(\omega) + \Delta\beta$. Correspondingly, Eq. 2.34 should be altered to accomodate $\Delta\beta$, using $(\beta(\omega) + \Delta\beta)^2 - \beta_0^2 \approx 2\beta_0(\beta(\omega) + \Delta\beta - \beta_0)$, likewise splitting β in a linear and a nonlinear component.

$$\frac{\partial\tilde{E}}{\partial z} = i[\beta(\omega) + \Delta\beta - \beta_0]\tilde{E}, \qquad (2.35)$$

and in time space

$$\begin{aligned}\frac{\partial\tilde{E}}{\partial z} &= i[\beta(\omega) - \beta_0]\tilde{E} + i\gamma|\tilde{E}|^2\tilde{E} \\ &\approx \frac{1}{2}\beta_2\frac{\partial^2}{\partial t^2}\tilde{E} + i\gamma|\tilde{E}|^2\tilde{E}, \qquad (2.36)\end{aligned}$$

where the conventional nonlinearity parameter $\gamma = (n_2\omega_0)/(cA_{eff})$ is introduced. Equation 2.36 is commonly referred to as the nonlinear Schrödinger equation. Next, the manifestations of the dispersion term and the nonlinear term, the first and second terms on the right-hand side, respectively, will be described. The dispersive term manifests itself as GVD and HOD; the nonlinear term as SPM; and the interplay between them results in FWM and soliton formation.

Dispersion

The propagation constant $\beta(\omega)$ and its frequency dependence determine the linear response. As in the previous section, we expand $\beta(\omega)$ in the angular frequency ω about the center frequency ω_0

$$\beta(\omega) = \beta_0 + \beta_1(\omega - \omega_0) + \frac{1}{2}\beta_2(\omega - \omega_0)^2, \qquad (2.37)$$

In the absence of nonlinear response (the $i\gamma|\tilde{E}|^2\tilde{E}$ term), the fields after linear propagation can be found exactly in the frequency domain:

$$\tilde{E}(z,\omega) = \tilde{E}(0,\omega)\exp[\frac{1}{2}\beta_2(\omega)(\omega - \omega_0)^2 z]. \qquad (2.38)$$

Self-phase modulation

Equation 2.36 can be solved exactly in the time domain in the absence of dispersion.

$$\tilde{E}(z,t) = \tilde{E}(0,t)e^{i\gamma|\tilde{E}(0,t)|^2 z}. \qquad (2.39)$$

An intensity-dependant, and thus time-dependant phase shift is imposed on the pulse during propagation.

Four-wave mixing

Discussions concerning four-wave mixing (FWM) in this context will be limited to a special case of degenerate FWM (Agrawal, 1995), which will become relevant in Chap. 8. Here, strong pump E_p and weak Stokes and anti-Stokes E_S and E_{aS} fields at frequencies ω_p, ω_S, and ω_{aS} are propagating in the fiber, interacting through the nonlinearity term. Degenerate FWM under this particular choice of fields is actually one of the processes that contribute to the nonresonant signal in CARS.

Because the pump is considered strong and undepleted, the anti-Stokes field can be treated as a perturbation. That is, the solution for the pump field can be found first, and the presence of the Stokes and

anti-Stokes will be assumed not to change these solutions. The wave
equation to be solved is

$$\frac{\partial E(z,t)}{\partial z} = i\gamma|E(z,t)|^2 E(z,t) \tag{2.40}$$

where $E(z,t) = \sum_{i=p,S,aS} E_i(z,t)$. In this equation, the fast-oscillating
fields rather than just the slowly-varying envelope. Solving first for the
strong pump in absence of other fields and in the quasi-monochromatic
case:

$$\tilde{E}_p = \sqrt{P_p}\exp(i\gamma P_p z), \tag{2.41}$$

keeping only terms of second order and higher in E_p, matching terms
that oscillate at the same frequencies, and collecting the exponentials
with the propagation constants on the right side,

$$\begin{aligned}
\frac{\partial \tilde{E}_S}{\partial z} &= i\gamma(2|\tilde{E}_p|^2 \tilde{E}_S + \tilde{E}_p \tilde{E}_p \tilde{E}_{aS}^*) \\
&\quad \times \exp[i(\Delta\beta + 2\gamma P_p)z] \tag{2.42} \\
\frac{\partial \tilde{E}_{aS}^*}{\partial z} &= -i\gamma(2|\tilde{E}_p|^2 \tilde{E}_{aS}^* + \tilde{E}_p^* \tilde{E}_p^* \tilde{E}_S) \\
&\quad \times \exp[-i(\Delta\beta + 2\gamma P_p)z]. \tag{2.43}
\end{aligned}$$

Introducing a phase on all the fields, $\tilde{E} \to \tilde{E}\exp[2i\gamma P_p z]$, the first term
on the right-hand side can be cancelled out.

$$\begin{aligned}
\frac{\partial \tilde{E}_S}{\partial z} &= i\gamma\tilde{E}_p\tilde{E}_p\tilde{E}_{aS}^*\exp[-i(\Delta\beta + 2\gamma P_p)z] \tag{2.44} \\
\frac{\partial \tilde{E}_{aS}^*}{\partial z} &= -i\gamma\tilde{E}_p^*\tilde{E}_p^*\tilde{E}_S\exp[i(\Delta\beta + 2\gamma P_p)z]. \tag{2.45}
\end{aligned}$$

The general solution is given by

$$\begin{aligned}
\tilde{E}_S &= (A_S e^{gz} + B_S e^{-gz})\exp(-i\kappa z/2) \tag{2.46} \\
\tilde{E}_{aS}^* &= (A_{aS} e^{gz} + B_{aS} e^{-gz})\exp(i\kappa z/2), \tag{2.47}
\end{aligned}$$

$$\tag{2.48}$$

where

$$\begin{aligned}
\kappa &= \Delta\beta + 2\gamma P_p \tag{2.49} \\
\Delta\beta &= 2\beta_p - \beta_S - \beta_{aS} \tag{2.50} \\
g &= \sqrt{(\gamma P_p)^2 - (\kappa/2)^2} \tag{2.51}
\end{aligned}$$

A consequence of the finite interaction distance is that phasematching
becomes important. $\Delta\beta$ is the wavevector mismatch between pump,

Stokes, and anti-Stokes fields. κ is the generalized wavevector mismatch, which also includes the "nonlinear phase" $2\gamma P_p$, created by the strong pump field. For perfect phasematching, $\kappa = 0$ and small P_p, the parametric gain reduces to the small-signal gain $g \approx \gamma P_p$.

Solitons

It is possible to solve Eq. 2.36 exactly (Agrawal, 1995), provided $\beta_2 < 0$. The function

$$\tilde{E}(z,t) = E_0 \text{sech}(\frac{2\ln(1+\sqrt{2})t}{\tau_{fwhm}})\exp(i\frac{3.11|\beta_2|}{\tau_{fwhm}^2}z) \qquad (2.52)$$

is a solution, which can be verified by insertion. Equation 2.52 is the functional form of a type of pulse known as a fundamental soliton. It has the special feat that it propagates in z and t without changing its shape. Other kinds of solitons are also a solution to Eq. 2.36. They are not stable upon propagation, but exhibit a periodic evolution. These are known as higher-order solitons. A dimensionless number N determines the order of the soliton, $N = 1$ corresponds to the fundamental soliton. It is given as

$$N^2 = 0.321\frac{\gamma P_0 \tau_{fwhm}^2}{|\beta_2|}. \qquad (2.53)$$

The soliton can be understood intuitively as a pulse, which is balanced by the competing effects of self-phase modulation and anomalous ($\beta_2 < 0$) GVD. Anomalous GVD imposes a negative chirp on a pulse, SPM broadens the spectrum. If the pulse gets a little "too short", SPM broadens the spectrum and increases the pulse stretching due to GVD. If the pulse gets a little "too long", the pulse stretching due to GVD gets less and SPM can broaden the spectrum once again. This scheme works only because SPM in addition to broadening the spectrum, also introduces a positive chirp.

Higher-order effects and delayed response

The nonlinear Schrödinger equation Eq. 2.36 is not generally applicable to short pulses with durations below ~ 100 fs. And specifically are solitons generally not exact solutions *i.e.* not generally stable inside fibers. For a full treatment of short pulses in optical fibers, more terms must be added. A more correct equation, the generalized nonlinear Schrödinger equation is typically used (Agrawal, 1995). It includes HOD, which is not conceptually different from GVD which is included in Eq. 2.36. It also includes delayed nonlinear response whereas the nonlinear response in Eq. 2.36 is instantaneous. The inclusion of delayed nonlinear

response amounts to recognizing that there are resonances in the fiber with which propagating light can interact, specifically there are Raman-active transitions. This means that the material-field interaction can not in general be considered instantaneous, and some response function must be included to the Schrödinger equation to account for this. The standard response function for silica fibers is well known, but it will not be discussed further here. Instead, the consequences of it will be stated. An important manifestation of the Raman effect in fibers is the soliton self-frequency shift (SSFS); if a soliton has sufficient spectral bandwidth, the blue components can act as Raman pump for the red components, which act as a Raman seed. This leads to a redshift of the soliton, which can be very large, it will be treated in Sec. 5.4.

2.6 Photonic crystal fibers
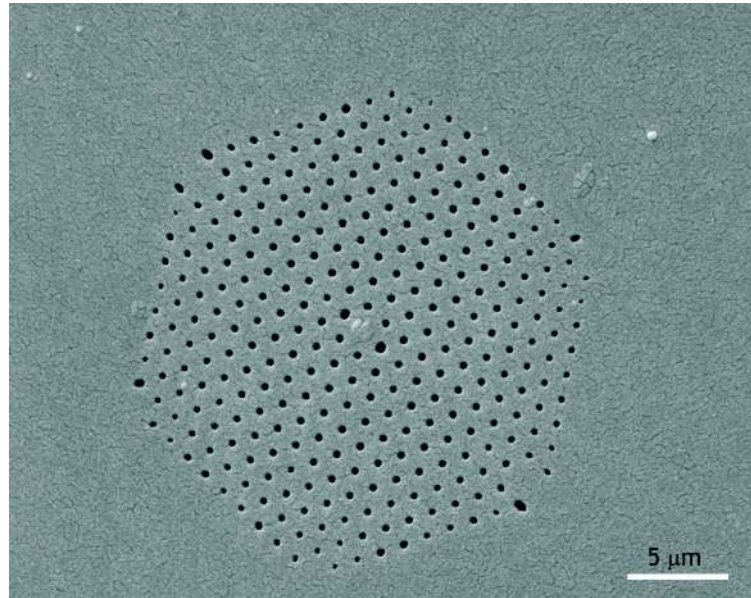
Introduction

Figure 2.2: Scanning electron micrograph of the endface of a PCF.

PCFs are a new class of microstructured fibers, which consist of a solid core surrounded by a regular array of air holes running along the entire length of the fiber. An example of a scanning electron mi-

crograph of one of the PCFs that were used in this thesis is shown in
Fig. 2.2. This structure leads to some interesting new light-guiding
and dispersion properties.

Light guidance

Modified total internal reflection

The first working realization of a PCF happened in 1996 (Knight et al.,
1996, 1997). PCFs guide light by the mechanism known as "modified
total internal reflection". In a sense, it is very similar to the way by
which standard step-index fibers guide light. The holey region around
the solid core can be thought of as a region with an effective refractive
index equal to the average refractive index in that region. The effective
index step in a PCF thus becomes very large compared to standard
fibers. There is one important difference between the two classes of
fibers, though. In PCFs, the core is connected by thin bridges of silica
to the cladding, which provides a way by which light can escape from
the core. This is responsible for the fact, that PCFs are "endlessly
single-moded". The PCF acts as a "modal sieve"; the fundamental
mode is so big that it cannot escape along the silica bridges. But the
higher order modes have smaller lobe sizes than the fundamental, so
they can escape more easily. (Birks et al., 1997).

Dispersion

In bulk silica, the zero-dispersion wavelength (ZDW) is at 1.3 μm with
GVD being "normal" below ($\beta_2 > 0$) and "anomalous" above ($\beta_2 < 0$).
The dispersion of standard fibers deviate little from the dispersion of
bulk silica. The dispersion of PCFs on the other hand can deviate
significantly from bulk silica. Because of the large refractive index dif-
ference between core and cladding, waveguide dispersion becomes very
important. Mathematically, the boundary conditions in the Helmholtz
equation Eq. 2.32 are changed significantly in comparison to standard
silica fibers. This gives rise to significantly different eigenvalues $\beta(\omega)$.
One effect of the waveguide dispersion is to shift the ZDW towards
lower wavelengths, ZDWs at a wavelength as low as 560 nm have been
reported (Knight et al., 2000). Fibers with two close-lying ZDWs have
also been fabricated, in which there is anomalous dispersion between
the two ZDWs [1]. And even PCFs with no ZDWs and normal dispersion
for all wavelengths have been demonstrated [2].

---

[1]For example the fiber NL-1.4-775 from Crystal Fibre A/S (www.crystal-fibre.com)

[2]For example the fiber NL-1050-NEG-1 from Crystal Fibre A/S, (www.crystal-fibre.com)

Nonlinear PCFs

PCFs with small core diameters (μm) are referred to as nonlinear PCFs. Their small core diameter and endlessly single-mode nature mean that optical pulses of very high intensity can propagate long distances in the fiber leading to very significant nonlinear effects. The magnitude of the nonlinear interaction by itself is not unique to PCFs, as similar nonlinearities are seen in standard fibers and tapered fibers. Nonlinearities in PCFs are interesting, because PCFs display unique dispersion properties. Specifically, the ZDW can be brought down to, or even below, 800 nm, the wavelength of the common Ti:Sapphire laser. This also means that the anomalous-dispersion region can be brought into the range of the Ti:Sapphire laser. All this means that nonlinear effects like solitons and FWM in fibers can be pushed towards the visible range.

Chapter 3

Review

3.1 Historical review

The first reports of the use of CARS for generating constrast in a scanning microscopy setup were in 1982 and 1984 (Duncan et al., 1982; Duncan, 1984). Here, two synchronously pumped picosecond dye lasers were used for exciting a sample of onion cells in a non-collinear geometry. The angle of the beams had to be adjusted in order to satisfy the phase-matching condition and the spatial resolution was therefore limited to 20 μm. This solution had limited potential. In 1999, a folded BoxCARS phasematching geometry was presented (Müller et al., 2000), which allowed for tighter focusing and better spatial resolution. This solution was still difficult, and only with the demonstration of CARS microscopy under collinear tight-focusing conditions, which relaxed the phase-matching requirement, CARS microscopy was realized in its current, most widely-used form (Zumbusch et al., 1999; Hashimoto et al., 2000). The vast majority of later work has been done in this geometry, an exception being a report of wide-field imaging (Heinrich et al., 2004).

Several experimental variations with different excitation and detection parameters have also been presented (Dudovich et al., 2002; Gershgoren et al., 2003; Lim et al., 2006; Ogilvie et al., 2006; Potma et al., 2006; Evans et al., 2004). But only the two presently most popular variations will be mentioned in this chapter, which will be referred to as CARS microscopy (Zumbusch et al., 1999) and CARS microspectroscopy (Müller and Schins, 2002; Cheng et al., 2002). They will be discussed in the context of their advantages, the present state of the field and the challenges posed at the moment.

3.2 Principle

Imaging based on CARS spectroscopy uses the pump and Stokes pulses to drive Raman-active vibrations at the pump-Stokes frequency difference, $\omega_p - \omega_S$, generating a blueshifted anti-Stokes signal at ω_{aS}. The resulting image is basically a map of the CARS signal at a certain pump-Stokes frequency difference. Due to the dependency of the CARS signal intensity upon molecular vibration frequencies, the CARS image represents an image with information about the distribution of molecules. The various implementations of CARS imaging can be divided into two main sub-groups, which will be reffered to as CARS microscopy and CARS microspectroscopy. They constitute the presently most popular implementations and distinguish themselves through choice of pump and Stokes pulses and detection scheme.
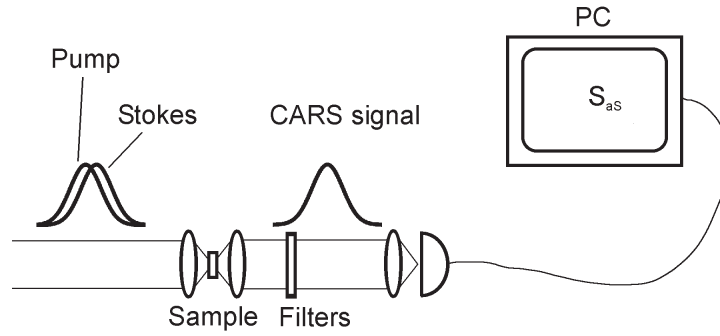
CARS microscopy

Figure 3.1: Sketch of a typical CARS microscope

CARS microscopy refers to the CARS imaging setup, where the pump and Stokes pulses both have a duration of few picoseconds. The detection of the blue-shifted CARS signal is done by a one-channel detector, such as an avalanche photo diode or a photomultiplier tube. These pulses can be considered quasi-monochromatic, so that the CARS signal is simply given by

$$S_{aS} = |\chi_{nr}^{(3)} + \chi^{(3)}(-\omega_{aS}; \omega_p, -\omega_S, \omega_p)|^2 I_p^2 I_S. \qquad (3.1)$$

A sketch of such a CARS microscope is seen in Fig. 3.1. The main feature of CARS microscopy is the ability for rapid sequential measure-

ment of S_{aS}, which in turn facilitates rapid (up to video rate) acquisition of images when scanning mirrors are used to scan the beams across the sample.
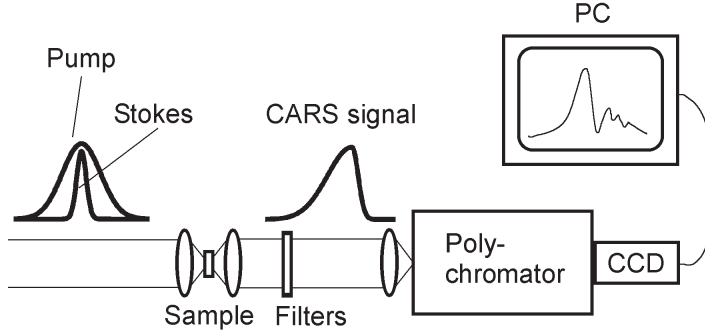
CARS microspectroscopy

Figure 3.2: Sketch of a typical CARS microspectroscope

In CARS microspectroscopy (or MCARS microscopy), the pump pulse is a picosecond pulse, while the Stokes pulse is femtosecond. The pump pulse can be regarded as quasi-monochromatic, but the Stokes pulse is now spectrally broad, which is reflected in the expression for the CARS signal,

$$S_{aS}(\omega_{aS}) = |\chi_{nr}^{(3)} + \chi^{(3)}(-\omega_{aS}; \omega_p, -\omega_S, \omega_p)|^2 I_p^2 I_S(\omega_S). \qquad (3.2)$$

The CARS signal now contains spectral information, so detection is done by sending the signal through a polychromator and detecting the CARS spectrum with a CCD camera. The main feature about CARS microspectroscopy is the parallel nature of the data acquisition; many molecular frequencies are interrogated at once, facilitating rapid acquisition of CARS spectra (milliseconds) *i.e.* rapid acquisition of local chemical information. A sketch of a CARS microspectroscope is seen in Fig. 3.2.

3.3 Motivation

CARS vs. Raman

Conventionally, chemical imaging would be linked with Raman microspectroscopy, where a single, narrowband laser is focussed onto a

sample and the red-shifted Stokes spectrum is detected and used to generate images with chemical contrast. CARS spectroscopy is an advanced method for obtaining the same vibrational information that can be obtained by Raman spectroscopy, so the two should be compared. The signals obtained in CARS spectroscopy (S_{aS}) as opposed to spontaneous Raman spectroscopy (S_{SRS}) are

$$S_{aS} \quad \propto \quad |\chi^{(3)}(-\omega_{aS}; \omega_p, -\omega_S, \omega_p)|^2 I_p^2 I_S, \qquad (3.3)$$

$$S_{SRS} \quad \propto \quad \text{Im}[\chi^{(3)}(-\omega_S; \omega_p, -\omega_S, \omega_p)] I_p. \qquad (3.4)$$

Possibly the biggest, single reason for favouring CARS over Raman in imaging setups is the big difference in CARS over Raman signal yield. The key to this difference is the spontaneous nature of Raman spectroscopy, whereas CARS is a coherent, or driven, process. Furthermore, the spontaneous Raman signal consists of signal at many frequencies, the system has a finite possibility of ending up in any Raman-active level. In CARS, the evolution of the system is directed. The presence of the Stokes pulse greatly enhances the propability of the system going through the Raman-active level at $\Omega_{vib} = \omega_p - \omega_S$. This "focussing" of the excitation partially explains the difference in signal yield. The different dependences on the excitation laser(s) opens up some interesting opportunities in CARS that are not present in Raman spectroscopy. S_{aS} is nonlinearly dependent on the laser intensities, so that if the average power is fixed, S_{aS} can be increased or decreased by varying the peak power (*i.e.* the repetition rate). This additional degree of freedom has important implications for optimizing the CARS signal yield while at the same time minimising the risk of damage to a sample. The average power can be fixed below the linear damage threshold, the peak power can then be increased (the repetition rate is decreased) to just below the nonlinear damage threshold, thus maximising the CARS signal. It is a hard to quantify, how big the difference in crosssections is, because the excitation schemes in CARS and Raman spectroscopy are different. However, in Kee and Cicerone (2004), a comparison of CARS and Raman spectra acquired with similar laser average power was done. The result was that the CARS spectrum required 60 times less acquisition time to achieve the same signal-to-noise level as the Raman spectrum.

Labeling

Because the CARS intensity depends on molecular vibrational resonances, the contrast in CARS images derives from properties that are intrinsic to the sample under study. This is yet another high-profile advantage of CARS imaging; there is no need to label the sample prior to

examining it in the microscope. This is particularly useful in the study of transport of small molecules. If this were to be accomplished in fluorescence microscopy, the small molecules would have to be stained with a fluorescent dye, which would most likely alter their transport properties and result in a measurement with low confidence.
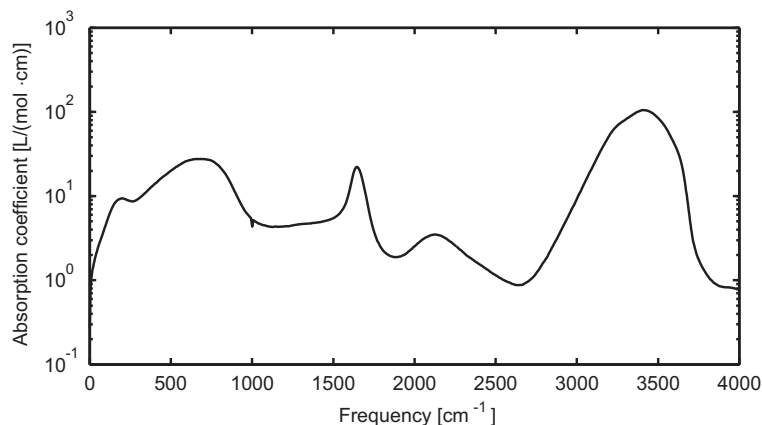
Wavelength regime

Figure 3.3: Absorption coeffient of water in the infrared region. From Bertie et al. (1989).

In the context of vibrational microscopy on biological samples, the absorption of the ubiquitous water must be considered. The interesting part of the vibrational spectrum is often in the 1600 cm^{-1}- (amide bands) and 3000 cm^{-1}-regions (C-H bands). Water absorbs strongly throughout the infrared region, as can be seen in Fig. 3.3, so an IR absorption approach to vibrational microscopy would be hampered by this fact, since the absorption of bands of interest would be obscured by the massive water background absorption. CARS circumvents this difficulty by employing visible or near-infrared lasers as pump and Stokes pulses to probe infrared transitions at the difference frequency. In the choice of laser wavelength, of course, water absorption should still be taken into account. Figure 3.4 shows the visible and NIR absorbance of typical biological sample constituents. It is apparent that to minimize effects of water absorption, the laser wavelengths are best kept below 1350 nm or, even better, below 1100 nm. There is also a lower limit to the pump and Stokes wavelengths, if absorption is to be minimized. Another important consideration is the importance of scattering of the laser beams. The cross-section for Rayleigh scattering is proportional
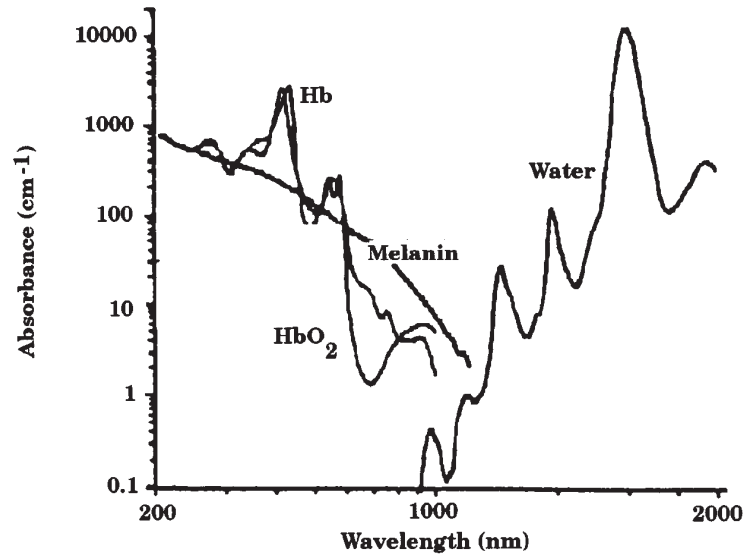
Figure 3.4: Absorption coefficient of typical biological sample constituents in the visible region. From Richards-Kortum and Sevick-Muraca (1996)

to λ^{-4}, so the impact of scattering is minimized for long wavelengths. The best compromise between these two considerations regarding optimal wavelengths is to use pump and Stokes wavelengths in the range 800 nm to 1100 nm, which corresponds to the difference frequencies lying in the range 0-3400 cm^{-1}.

Spatial resolution

It is expected that CARS microscopy and microspectroscopy in the tight-focusing collinear geometry has spatial resolution below the diffraction limit due to the cubed dependence upon excitation pulse intensity. The diffraction limit in the Rayleigh criterion is $0.61\lambda_P/NA$ transversely and $2n\lambda/NA$ axially (Born and Wolf, 1999). As the CARS intensity is proportional to the cube, the volume in which it is generated, should be less than the focal volume. Another consequence of the nonlinear intensity dependence is that axial spatial resolution is inherent, similar to multi-photon microscopy techniques. In Cheng et al. (2002), the spatial resolution has been investigated theoretically. Indeed, it was found that a scatterer of diameter $0.2\lambda_P$ should show have an FWHM of $0.25\lambda_P$ in a CARS image with a 1.4 NA microscope ob-

jective. This is well below the diffraction limit, which in this case is $0.44\lambda_P$. However, a CARS image is still formed as the coherent sum of signal from contributing scatterers, so this resolution must be taken with a grain of salt. If there are several scatteres in close proximity, the resulting image will not just be the sum of the individual contributions. There will be interference between the contributions, making interpretation of images difficult.

Autofluorescence

Samples illuminated by laser light typically gives off some fluorescence, even when not stained with fluorescent dyes. This is known as autofluorescence. By the Frank-Condon principle, this autofluorescence is given off at lower frequencies than the exciting laser. This means that in *e.g.* Raman microspectroscopy, where the signal frequency is smaller than the pump frequency, there will be fluorescent background. CARS circumvents this problem, because signal is detected at the blue-shifted anti-Stokes frequency.

Photodamage

As discussed above, the nonlinear dependence of the CARS signal S_{aS} upon excitation intensities provides us with "knobs" for increasing CARS signal while tweaking the average power and peak power to optimize sample viability. With the emergence of two-photon fluorescence microscopy (2PF), numerous advantages in terms of sample viability were put forward (Denk et al., 1990; Denk and Svoboda, 1997), these can also be used on CARS microscopy. Propably the single most important advantage of 2PF and CARS is the fact that no signal is produced outside the focus so no confocal pinhole is needed. In one-photon fluorescence microscopy, excitation power would get wasted outside the focus and in the pinhole, so that higher laser powers are needed, increasing the risk of (linear) photodamage. As previously noted, the prospect of less linear photodamage is one of the quoted advantages of CARS. However, in multiphoton microscopy, much higher intensities are employed, so the risk of nonlinear photodamage should be considered. This has been the subject for several papers. Several papers have quite consistently established the threshold for linear damage at around 10 mW (König et al., 1997; Fu et al., 2006; Nan et al., 2006b). For femto- and picosecond excitation, it has been established, that damage rate increases nonlinearly with excitation peak power, with exponents lying in the range 1.81-2.5 (König et al., 1999; Hopt and Neher, 2001; Fu et al., 2006; Koester et al., 1999). Damage thresholds in CARS microscopy of 1-2 nJ pulse energy for picosecond pulses have been reported (Nan

et al., 2006b; Fu et al., 2006). In CARS, it has been found that stimulated Raman processes actually enhance the damage rate (Fu et al., 2006). The wavelength dependence of the damage rate has also been studied, showing that damage rate increases with shorter wavelength. (Fu et al., 2006; König et al., 1995). Damage increases with pixel dwell time, so that image acquisition should occur as fast as possible.

3.4   Challenges

Nonresonant background

Results from a numerical calculation of resonant and nonresonant signal intensities as well as their ratio are presented in Fig. 3.5 for both CARS and MCARS. The calculations were done using the method outlined in Chap. 2, using Eq. 2.23 and 2.26 (the Matlab script in App. B. The pump and Stokes pulses are assumed to be transform-limited. Spectra were calculated for various durations of the pump and Stokes pulses. In Fig. 3.5a, the plotted S_{aS} is the spectrally integrated intensity while in Fig. 3.5b, it is the spectral intensity at $\omega_{aS} = 15500 \ \mathrm{cm}^{-1}$. The nonresonant spectra were calculated assuming a purely nonresonant response, while the resonant spectra were done assuming a purely resonant response. In particular the ratio is of interest and in both cases, the ratio reaches a plateau, when the pulse duration comes close to the decoherence time of the vibration, $1/\Gamma$

Noise

The impact of the nonresonant background is profound, when it comes to the sensitivity of CARS, because the nonresonant background does not only contribute as a background; it also contributes Poisson noise (or shot-noise). In a shot-noise limited measurement, the measured value is $< N > \pm\sigma(< N >)$, where the standard deviation is given as $\sigma(< N >) = \sqrt{< N >}$. The impact of this is illustrated with simple calculations in Fig. 3.6 for 3 different signal counts in the case of CARS microspectroscopy. To obtain $\chi^{(3)}$ from the CARS spectra, one must calculate the normalized CARS signal S

$$S = \frac{S_{aS} - S_{ref}}{S_{ref}} \propto |\chi_r^{(3)} + \chi_{nr}^{(3)}|^2, \tag{3.5}$$

where S_{ref} is the spectrum of the purely nonresonant signal. The noise increases in the normalisation process, because it involves both a subtraction and a division The Poisson noise cannot be done away with, and is an intrinsic problem of detection at low light levels. The only way to do away with it is to increase the signal count so as to minimize
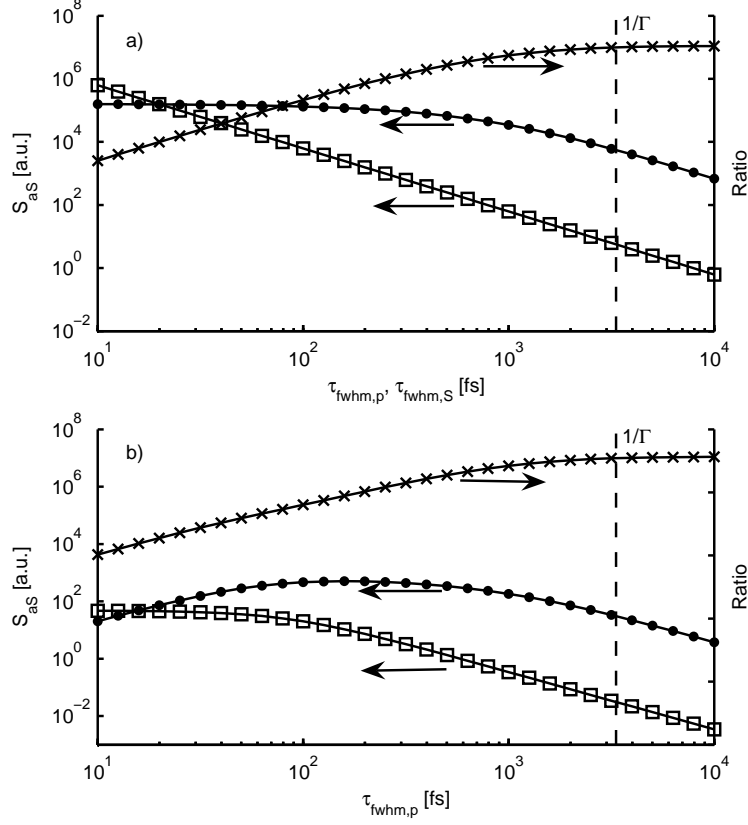
Figure 3.5: Calculation of CARS signal intensities from a single resonance in (a) CARS vs. $\tau_{fwhm,p} = \tau_{fwhm,S}$ and (b) MCARS vs $\tau_{fwhm,p}$ for fixed $\tau_{fwhm,S} = 60$ fs. Parameters were $\Gamma_0 = 10$ cm^{-1}; $\nu_0 = 3000$ cm^{-1}; $\nu_p = 12500$ cm^{-1}; $\nu_S = 9500$ cm^{-1} ($\nu_p - \nu_S$=3000). Dots: resonant signal; squares: Nonresonant signal; crosses: resonant-to-nonresonant signal ratio. The average power was the same for all calculations.
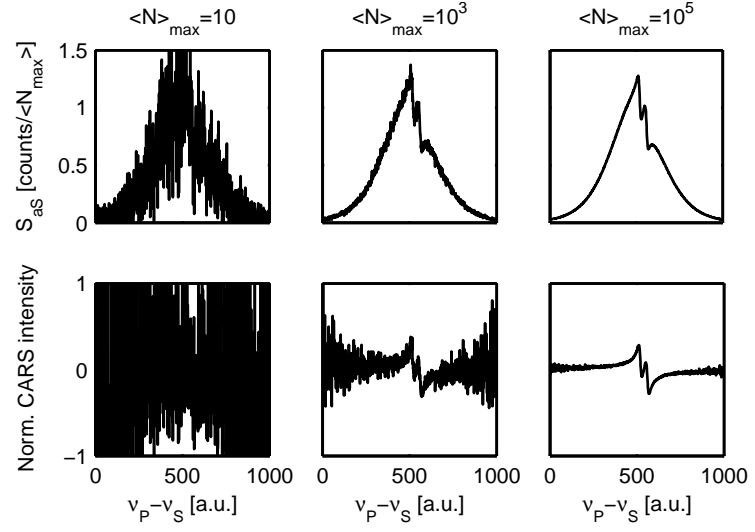
Figure 3.6: (Top row) examples of (calculated) CARS spectra with resonant and nonresonant contributions and Poisson noise; (bottom row) corresponding normalized CARS spectra. $< N >_{max}$ is defined as the highest count in one channel in the nonresonant spectrum.
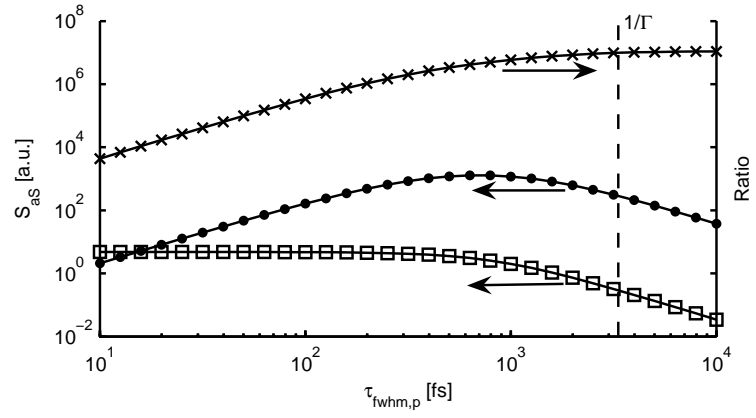

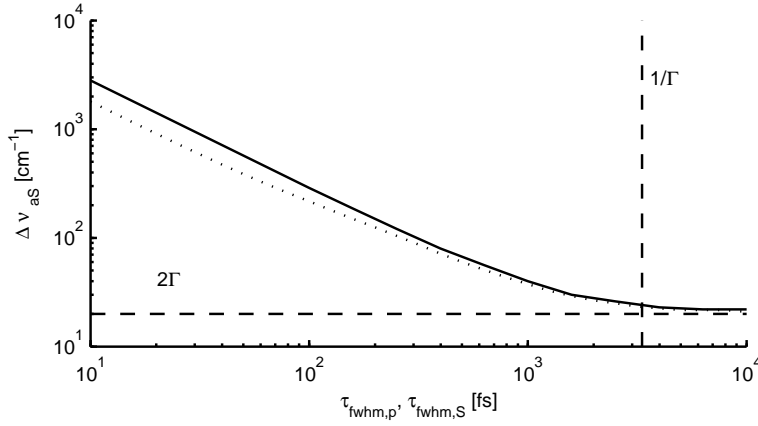Figure 3.7: Same as Fig. 3.5b, but with $\tau_{fwhm,S} = 600$ fs.

Figure 3.8: Calculation of measured anti-Stokes spectrum in (solid line) CARS spectroscopy versus pump and Stokes pulse durations FWHM; and in (dashed line) MCARS spectroscopy versus pump pulse duration FWHM. In both cases, Γ was 10 cm^{-1}.

the relative noise. Examining Fig. 3.5, we find that, generally, signal intensity is maximized for shortest possible pump and Stokes pulses. we find that the CARS signal is significantly stronger than the MCARS signal. This is remeniscent of the fact that the plotted MCARS signal is the signal in one of many channels, where the CARS signal is the (spectrally) integrated signal. Still, this is important in terms of Poisson noise. Figure 3.7 shows the MCARS signal with a ten times longer Stokes pulse than in Fig. 3.5b. The result is an increase in the maximum resonant signal intensity and that the resonant signal is maximized for pump pulse durations closer to the decoherence time of the vibration than was the case in Fig. 3.5b. Put in other terms, the spectral resolution in this case is better at the maximum of the resonant signal than in Fig. 3.5b.

Spectral resolution

The calculated spectral resolution (defined as the width FWHM of a single anti-Stokes line in absence of nonresonant background) versus pump (and Stokes) pulse durations in CARS and MCARS spectroscopy is shown in Fig. 3.8. In CARS, spectroscopy is done sequentially, by scanning the pump or Stokes frequency. In MCARS, it is done just by recording the anti-Stokes spectrum. This difference in detection gives MCARS a small advantage in terms of spectral resolution.
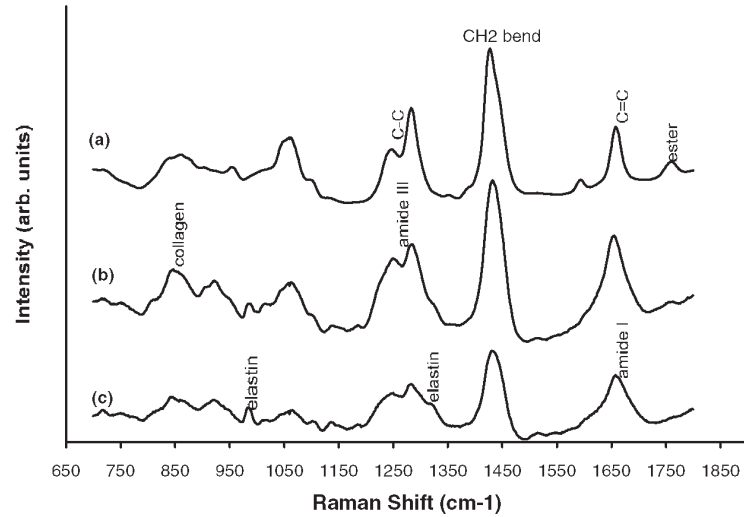
Figure 3.9: Raman spectra of (a) normal, (b) benign, and (c) malignant breast tissue. From Manoharan et al. (1998).

3.5   Conclusion

We are now in a position to start discussing, how the optimal laser for CARS microscopy and microscopy should look. So far, this chapter has reviewed the advantages of the nonlinear Raman approach as well as the challenges posed at the moment. In view of this, we are now in a position to consider just how, these points should be reflected in the choice of the optimal laser source, if the aim is CARS microscopy or CARS microspectroscopy.

i) The optimal operating wavelength region would be the near-infrared ca. 800 - 1100 nm, at the red edge of the "water window" to minimize absorption and scattering losses.

ii) In the context of resonant to nonresonant signal ratio, it was discussed in Sec. 3.4 that a pump spectral width similar to the width of the Raman line under study yields simultaneously high signal strength and good resonant to nonresonant signal ratio. It would therefore be desirable to have the control over the spectral width of the pump, so as to always be able to adapt the setup to the experimental conditions. The pump, which determines spectral resolution should have spectral width ≈ 5 cm^{-1}, given by the typical Raman linewidth in condensed samples (an example is shown in Fig. 3.9). In CARS microscopy, the same goes for the Stokes pulse. In CARS microspectroscopy, it is desirable to have a Stokes pulse with spectral width as wide as is needed

to study a particular sample, but no wider to maintain high resonant signal.

iii) Both average power and peak power should be as high as the sample damage threshold allows to get the most intense anti-Stokes signal in order to reduce Poisson noise and allow for fast data acquisition. In view of the discussion of sample damage above, pulse energies in the nJ-range are desired. This corresponds to the pulse energies from typical Ti:sapphire oscillator with repetition rates ≈ 80 MHz.

The remainder of the thesis is devoted to the question whether it is possible to realize these requirements using a single laser approach relying on PCFs for spectral shaping and conversion. It will be investigated whether it can be done to such a degree of satisfaction that it is feasible for use in a working CARS microspectroscopy setup.

Part II

Single-laser light sources

Chapter 4

Spectral compression

4.1 Introduction

This focus of this chapter is the application of PCFs to spectrally tailor laser pulses into pulses suitable for CARS microspectroscopy. Specifically, it will be presented, how we have succeded in spectrally compressing fs pulses at 800 nm from a Ti:sapphire laser oscillator.

A CARS light source based on a single, unamplified laser runs into the problem that the frequency-shifted Stokes pulse is most easily created by a nonlinear effect when starting out with a fs pulse because of its high peak power, yet a ps pulse is required as the pump pulse to assure satisfactory spectral resolution. So, the somewhat paradoxial situation is, that we would like the laser to be both a fs-laser and a ps-laser at the same time. A solution to this problem is to spectrally compress the pulses in nonlinear PCFs which, in effect, converts fs pulses to near-transform-limited ps pulses. Spectral compression has the advantage over spectral filtering that the spectral brightness is increased significantly.

The effect has previously been employed to create picosecond pulses in a fiber amplifier (Limpert et al., 2002, 2005). spectral compression in a single-mode fiber was first observed in 1978 (Stolen and Lin, 1978), but not satisfactorily explained until 1993 (Oberthaler and Höpfel, 1993; Planas et al., 1993), where the cause of the spectrum narrowing was ascribed to self-phase modulation (SPM). Earlier studies of spectral compression were performed in standard single-mode fibers. At 1060 nm, a compression factor of 16 was reached (Limpert et al., 2002) and at 1030 nm, 7.4 (Limpert et al., 2005). At 800 nm, more modest factors of 4 and 3 have been reported (Oberthaler and Höpfel, 1993; Washburn et al., 2000).

Spectral compression in PCFs is more versatile than in standard

silica fibers. Quoting Sec. 2.6, the ZDW of PCFs can be tuned over a wide range. This means that spectral compression can be performed in a PCF with low GVD at the laser wavelength, minimizing the detrimental effects of dispersion and allowing for more efficient compression. Furthermore, as the ZDW can be pushed down into the visible region, spectral compression can be performed efficiently at lower wavelengths than previously. The high nonlinearity and low dispersion is expected to beget high efficiency for spectral compression and, indeed, this turns out to be the case; the compression factor in PCFs can be dramatically increased over standard fibers. Here, we observe compression factors up to 28.

This chapter is arranged as follows. Section 4.2 will provide the theoretical description of spectral compression and give an analytical description of its dependency on relevant parameters; Sec. 4.3 will examine more deeply the dependencies by numerical methods; Sec. 4.4 describes the actual experiments done by us; finally, sections 4.5 and 4.6 will discuss future prospects and conclude.

4.2 Theory

The equation describing pulse evolution in a fiber is the NLSE Eq. 2.36, which only includes GVD and nonlinearity. Spectral compression occurs, when the input pulse is highly negatively chirped. The action of SPM on a Gaussian pulse amounts to a time-dependent frequency shift. The shift near the center of the pulse has a nearly linear slope whose sign is opposite to the chirp. In the leading and falling edge, it has the same sign. Near the center of the pulse, SPM thus compensates the chirp, and the central part of the pulse spectrum is compressed towards the central frequency, while the wings of the spectrum are broadened. To a given input pulse chirp corresponds one optimal value of the product of the pulse peak power and fiber length, that gives rise to the minimum output pulse width.

Scaling of spectral compression

The nonlinear problem (*i.e.* setting $\beta_2=0$ in Eq. 2.36) can be solved exactly in the time-domain,

$$\tilde{E}(L) = \tilde{E}(0)\exp(i\gamma L|\tilde{E}(0)|^2), \tag{4.1}$$

where L is the length of the fiber. In this context, chirp is best treated in the time-domain. Then, the chirped, Gaussian pulse, $\tilde{E}(0)$, can be written as

$$\tilde{E}(0) = \sqrt{P_0}\exp\Big(-\frac{2\ln2}{\tau_{fwhm}^2}t^2\Big)\cdot\exp\Big(-i\alpha\frac{2\ln2}{\tau_{fwhm}^2}t^2\Big), \tag{4.2}$$

where τ_{fwhm} is the duration FWHM of the chirped intensity envelope, P_0 the peak power, and α a dimensionless chirp parameter, that says something about the linear chirp. By Fourier transformation of the time-domain expression, α can be related to the pulse spectral width FWHM, $\Delta\omega$,

$$\Delta\omega = 4\ln2\frac{\sqrt{1+\alpha^2}}{\tau_{fwhm}}, \tag{4.3}$$

or

$$\alpha = \sqrt{\left(\frac{\Delta\omega\tau_{fwhm}}{4\ln2}\right)^2 - 1}. \tag{4.4}$$

And for pulses far from the transform-limit:

$$\alpha \approx \frac{\Delta\omega\tau_{fwhm}}{4\ln2} \tag{4.5}$$

At this point it can be realized, that the narrowest peak in the spectrally compressed spectrum is obtained, when the double derivatives of the arguments of the complex exponential functions in Eq. 4.1 and 4.2 are equal, but opposite, evaluated at the pulse center $t=0$. This amounts to requiring that the slope of the frequency shift imposed by SPM is equal but opposite to the slope of the chirped pulse instantaneous frequency. Actually, the condition that flat instantaneous frequency corresponds to the minimum spectral width is not true; the minimum width occurs for slightly positive chirp, but we will use the condition here, because it is a rigorous condition that can be used in the analytical treatment. The double derivatives give:

$$\frac{d^2}{dt^2}(\gamma L|\tilde{E}(0)|^2)\Big|_{t=0} = \frac{d^2}{dt^2}\left(\alpha\frac{2\ln2}{\tau_{fwhm}^2}t^2\right)\Big|_{t=0} \Leftrightarrow \tag{4.6}$$

$$\frac{\alpha}{\gamma LP_0} = 1. \tag{4.7}$$

Or, for very non-transform-limited pulses

$$\frac{\Delta\omega\tau_{fwhm}}{\gamma LP_0} = 4\ln2. \tag{4.8}$$

From these identities, Eq. 4.7 and 4.8, the scaling of spectral compression can immediately be deduced. The approach of this section has completely neglected the effects of dispersion in the PCF. If dispersion and nonlinearities are acting at the same time, numerical simulations are needed, such as the split-step Fourier method.

4.3   Numerical simulations

The split-step Fourier method

The numerical calculations performed in this section are done by finding the solution of Eq. 2.36. This equation is generally not analytically solvable, so other methods must be used. It can be written in the form

$$\frac{\partial \tilde{E}}{\partial z} = (\hat{D} + \hat{N})\tilde{E}, \qquad (4.9)$$

where

$$\hat{D} = -\frac{i}{2}\beta_2\frac{\partial^2}{\partial t^2} + \frac{1}{6}\beta_3\frac{\partial^3}{\partial t^3} + \ldots \qquad (4.10)$$

$$\hat{N} = i\gamma|\tilde{E}|^2. \qquad (4.11)$$

$\hat{D}$ is the operator responsible for dispersion, $\hat{N}$ for nonlinearities. It is apparent that equation

$$\frac{\partial \tilde{E}}{\partial z} = \hat{N}\tilde{E} \qquad (4.12)$$

is exactly solvable in the time domain, while the equation

$$\frac{\partial \tilde{E}}{\partial z} = \hat{D}\tilde{E} \qquad (4.13)$$

is exactly solvable in the frequency domain (with $\frac{\partial}{\partial t}$ becoming $i\omega$ upon going from the time to the frequency domain). A numerical method taking into account both $\hat{N}$ and $\hat{D}$ is the "split-step Fourier method" (Agrawal, 1995). Briefly, to propagate the solution one step from $\tilde{E}(z)$ to $\tilde{E}(z+dz)$, $\tilde{E}(z)$ is first Fourier-transformed into the frequency domain and the dispersion operator $\hat{D}$ is applied. Then the result is Fourier-transformed back into the time domain and the nonlinearity operator, $\hat{N}$, is applied. A Matlab script was written (App. C) to simulate the propagation of pulses in fibers utilizing the split-step Fourier method. The integration along z is done using the fourth-order Runge-Kutta method (Press et al., 1992). For optimization of execution speed, a Cash-Carp adaptive step size algorithm is used (Press et al., 1992).

A note on parameters

In the numerical simulations to follow, the pulse energy, E_{pulse}, and the chirped pulse duration FWHM, τ_{fwhm}, will be considered as parameters, because in the experiment, they are the ones that are most easily controlled of all the relevant parameters. The parameter L, the PCF length will be considered fixed at 1 m, because in practise, it can only be changed irreversibly.
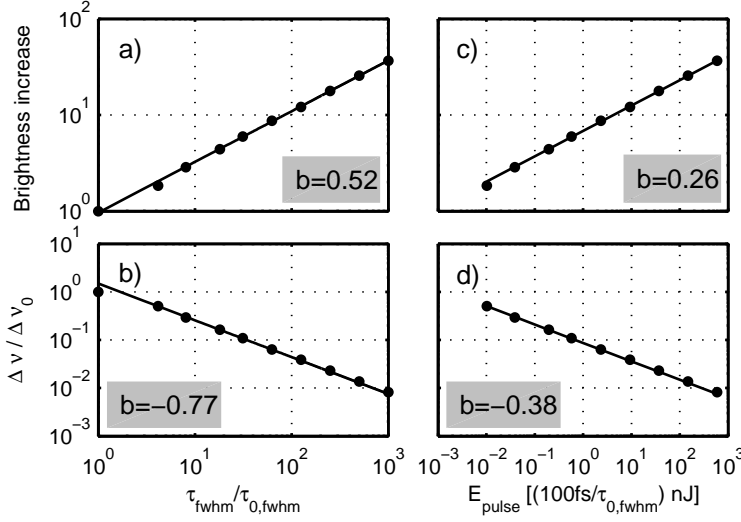
Brightness and spectral width

Figure 4.1: Calculations of spectrally compressed pulse parameters in the absence of GVD and HOD. (a) Brightness increase factor vs. chirped pulse duration; (b) spectral compression factor vs. chirped pulse duration; (c) brightness increase factor vs. pulse energy; (d) spectral compression factor vs. pulse energy. Dots represent calculated values; the lines represent fits of power functions, $y = ax^b$. $\tau_{0,fwhm}$ is defined as the FWHM of the pulse if it were transform-limited. Other parameteres were fixed at $\gamma = 0.09$ $(\mathrm{Wm})^{-1}$; $L = 1$ m.

Figure 4.1 further elaborates on the scaling in spectral compression, which was touched upon in Sec. 4.2. The compressed pulses are calculated by simply using Eq. 4.1, using as a constraint that the resulting pulses have flat instantaneous frequency at the pulse center (Eq. 4.7). The compressed pulses are described by the two parameters, the spectral width FWHM, $\Delta\nu$ (initial spectral width is denoted $\Delta\nu_0$). The brightness increase is defined as $B/B_0 = x\Delta\nu_0/\Delta\nu$, where x is the fraction of the spectrum contained in the central peak.

Figure 4.1 thus gives graphical substance to Eq. 4.8. The compression factor stays the same, no matter the initial laser bandwidth (Fig. 4.1b), and so does the brightness increase (Fig. 4.1a). The scaling of these two parameters with pulse energy is slightly more interesting and slightly less obvious, because x decreases with higher compression factors. The result is that the compressed spectral width increases slowly

with pulse energy as a power function with exponent -0.38 (Fig. 4.1d). And the brightness increases even slower with exponent 0.26 (Fig. 4.1c). The mild dependence upon the pulse energy means that the available pulse energy of the laser soon becomes a deciding factor (typically ≈ 10 nJ for a Ti:Sapphire oscillator). The normalized energy axis makes it evident that spectral compression is most economical with short pulses.

The impact of higher-order chirp

The parameters of the calculations above were modified to include third-order chirp, or cubic phase, on the initial pulse. Initial pulses with $\tau_{0,fwhm} = 100$ fs, $\tau_{fwhm} = 10000$ fs, and cubic phases in the range $\Phi_3 = \pm 2 \cdot 10^6$ fs^3. The impact on spectral compression and brightness was negligible. The only noticeable effect was a small frequency shift of the compressed pulse of 12 cm^{-1} for $\Phi_3 = 2 \cdot 10^6$ fs^3, which corresponds to the TOD in a 46 m-long piece of PCF 1 (to be introduced in Sec. 4.4.

The impact of GVD and HOD

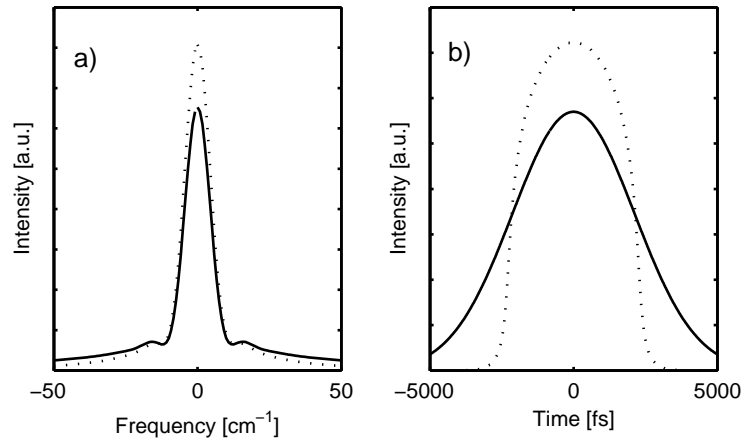Figure 4.2: Calculated (a) compressed spectra and (b) temporal intensities of 100 fs pulses initially chirped to 5 ps in 1 m PCF in the absence of GVD (solid line); and for $\beta_2 = 10^5$fs^2/m (dotted line).

So far, the dispersion of the PCF has been left out in the calculations. Although the reason stated above for using PCFs for spectral compression was, that the GVD could be controlled, it is important to

notice that GVD is not in general detrimental to spectral compression. Figure 4.2 shows a calculation, which demonstrates that in the presence of GVD, the brightness of the compressed pulse can be improved. As can be seen from the temporal intensities, Fig. 4.2, GVD in this case makes the pulse resemble a parabola more than a Gaussian. Which is why the frequency shift caused by SPM becomes more linear. It should be noted, that this is a special case - only certain combinations of GVD and initial chirp cause the beneficial effect. If the initial chirp is too small for a given GVD, then it becomes impossible to get a flat instantaneous frequency of the compressed pulse. GVD will not be treated in anymore detail here, rather, this example should serve as a motivation for studying spectral compression of pulses that initially have parabolic temporal envelopes (to be discussed in Sec. 4.5).

4.4 Experimental
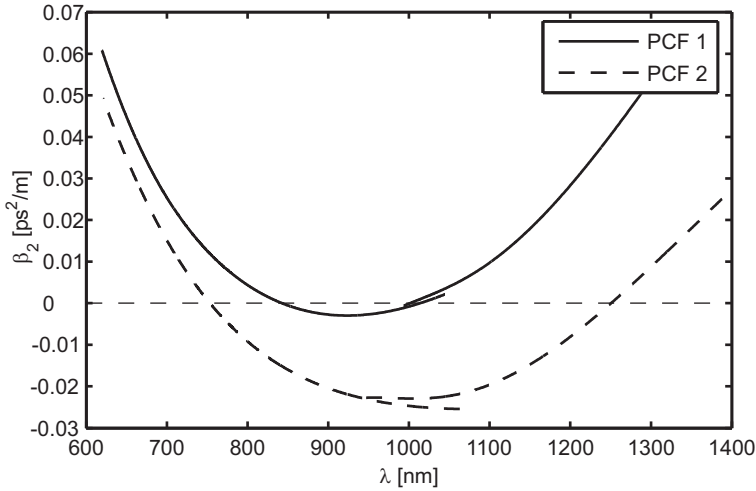
Photonic-crystal fibers

Figure 4.3: Dispersion curves of the NL-800-PM-testfiber #5 (PCF 1) and NL-800-PM-testfiber #2 (PCF 2). Data obtained from Crystal Fibre A/S.

The PCFs employed here are two polarization maintaining (PM) nonlinear test fibres from Crystal Fibre A/S, "NL-800-PM-testfiber #5" and "NL-800-PM-testfiber #2", henceforth denoted "PCF 1" and

	PCF 1	PCF 2
β_2 [fs^2/m]	$3.4 \cdot 10^3$	$-9.5 \cdot 10^3$
β_3 [fs^3/m]	$4.3 \cdot 10^4$	$5.8 \cdot 10^4$
β_4 [fs^4/m]	$1.3 \cdot 10^5$	$9.7 \cdot 10^4$
γ [(Wm)$^{-1}$]	0.09	0.09
L_D [m]	0.28	0.10
L'_D [m]	0.69	0.51
L'_D [m]	7.1	9.5

Table 4.1: Parameters at 800 nm of the photonic-crystal fibers PCF 1 and PCF 2. L_D, L'_D, and L''_D are given for a pulse with $\tau_{0,fwhm} = 52$ fs. Data obtained from Crystal Fibre A/S.

"PCF 2". Both are solid-core PCFs with two ZDWs with core diameter 1.8 μm. The dispersion curves are depicted in Fig. 4.3. The parameters of the fibers are presented in Table 4.1. The "dispersion lengths" in the table are defined as $L_D = \tau_0^2/|\beta_2|$, $L'_D = \tau_0^3/|\beta_3|$, and $L''_D = \tau_0^4/|\beta_4|$. τ_0 is the transform-limited temporal width($\tau_{0,fwhm} = 2\sqrt{\ln 2}\tau_0$). The L_D's in the table are given for a pulse with $\tau_{0,fwhm} = 52$ fs or spectral width FWHM 18 nm, which corresponds to the parameterers later to be used experimentally (Sec. 4.4). Higher-order dispersion (and even GVD) can to a good approximation be neglected; the fiber lengths employed here are of the order of meters. The impact of GVD and HOD is mitigated somewhat by the the fact that, as the pulse is spectrally compressed, the spectral width actually reduces down the length of the PCF.

Setup

The experimental setup is detailed in Fig. 4.4. A Ti:Sapphire oscillator at 76 MHz is used as the light source delivering the 810 nm fs pulses with spectral width 18 nm to be spectrally compressed. The laser pulse is given a negative chirp by a prism pair. The chirped pulse duration can be tuned by varying the interprism distance (Zhu et al., 1996). For each prism setting, the pulse duration is measured by interferometric autocorrelation, and PCF output spectra are acquired with a fiber-coupled spectrometer (ANDO AQ6312B) for a series of optical powers. The spectral width of the pulses can be changed by changing the output spectral width of the laser itself.
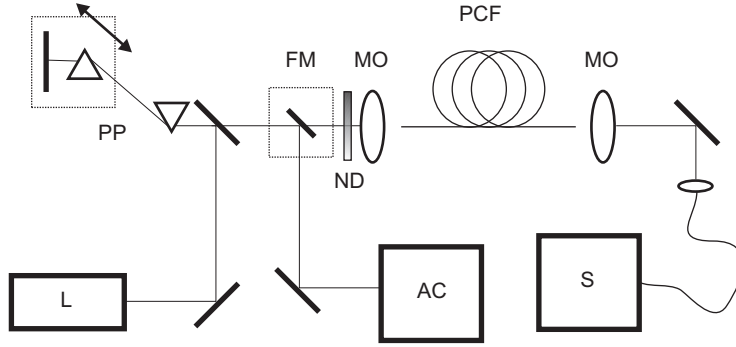
Figure 4.4: Sketch of the experimental setup. L: Laser; PP: Prism pair; FM: Flip mirror; ND: Graded neutral-density filter; MO: Microscope objective; PCF: Photonic crystal fiber; S: Fiber-coupled spectrometer; AC: Autocorrelator;

Results

Typical output spectra of the two PCFs vs. power are shown in Fig. 4.5a for PCF 1 and 4.5b for PCF 2. Both figures show the initial narrowing of the spectrum that can be accredited to SPM. Subsequently, both spectra broaden. In PCF 2, which has anomalous GVD at 800 nm, the spectrum is more "messy" than in PCF 1. In particular, sidebands start to show around 15 mW. These are caused by modulation instability (Agrawal, 1995). Modulation instability can be thought of as FWM phasematched by the nonlinearity, it only takes place, if the GVD is anomalous. It is the manifestation of the fact that a pulse propagating in anomalous GVD is inherently unstable and will tend to break up in a periodic train, hence the appearance of the sidebands. This example merely goes to show that though spectral compression is possible in anomalous GVD, one should do so with caution, and a PCF with normal GVD is the preferred choice. So, no more measurements on PCF 2 with anomalous dispersion will be presented here.

In Fig. 4.5c and d calculations based on eq. 2.36 with the same dispersion parameters as the two fibers are shown. Good correspondance is observed between experiment and simulation. This nice agreement is encouraging, as it indicates that the numerical method of Sec. 4.3 is accurate.

That the observed narrowing is indeed a frequency conversion rather than spectral filtering is substantiated by observing that the PCF output power is proportional to the input power. The best total transmission through the input objective, fiber, and output objective was around 40%.
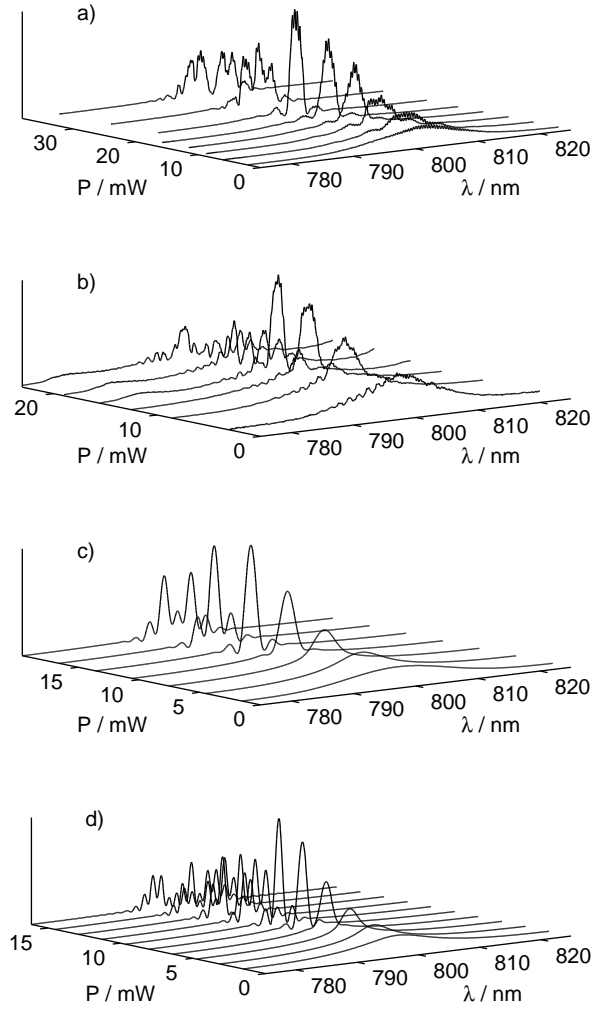
Figure 4.5: PCF output spectra vs. power (a) Measurement, 60 cm PCF 1; (b) Measurement, 60 cm PCF 2; (c) Calculation with parameters as PCF 1; (d) Calculation with parameters as PCF 2.

Figure 4.6 shows the result of measurements on spectral compression in a 210 cm-long piece of PCF 1 for differently chirped input pulses with fixed spectral width. Input spectral width was 18 nm or 280 cm^{-1}. The measured points all lie below the theoretical line (dashed), which
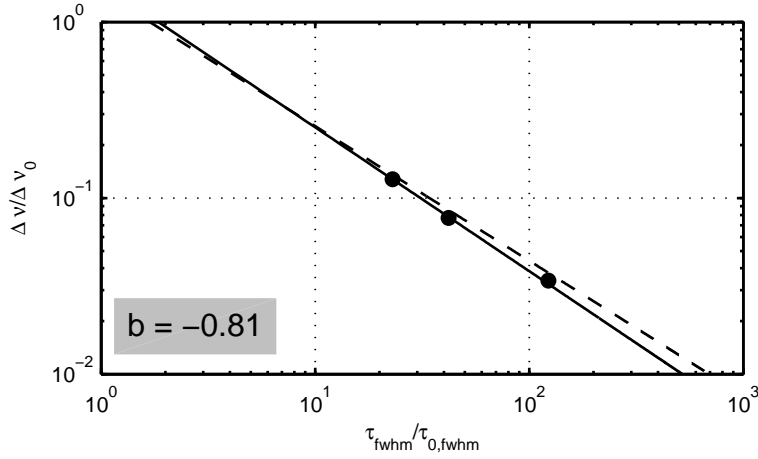
Figure 4.6: (Dots) Measured spectral compression factor vs. chirped pulse duration in 210 cm PCF 1; (solid line) fit of $y = ax^b$ to the data; (dashed line) fit to the theoretical results in Fig. 4.1b.

marks the compressed spectral width in absence of dispersion. There are several possible explanations for this. It may be caused simply by measurement uncertainty due to the fact that the compressed spectrum was determined by eye. Second, it may be that only a part of the input spectrum was actually coupled into the fiber because of spatial chirp in the laser beam. Finally, it may be the manifestation of the beneficial effect of GVD (discussed in Sec. 4.3). The best compression factor is achieved for an input pulse chirped to 6.4 ps duration FWHM with a PCF output power of 27.1 mW. In this case, the compressed spectral width is 0.6 nm or 10 cm^{-1}, a compression factor of 28. The corresponding brightness increase (disregarding any coupling losses) would be $B/B_0 \approx 17$. Practical conditions set the limit for, how high compression factors could be achieved. For chirped pulses >3 ps, an SF10 prism pair could be used to produce the chirp, the prisms introduced only a small power loss, but the chirp that could be produced was set by the prism dimensions and the spatial dispersion of the beam. For chirped pulses >3 ps, a pair of transmission gratings was employed (1200 lines/mm, blazed at 1000 nm), the overall transmission of the pair was 30 %, leaving 130 mW for coupling into the PCF. Clearly, either gratings with lower loss or simply larger prisms would allow for chirping pulses with lower loss and allow for even greater compression factors. It is furthermore seen from Fig. 4.6, that detrimental effects of PCF dispersion have not begun to set in at this fiber length; *i.e.* the

impact of dispersion is not so big that it reduces the impact of SPM to any significant degree. An alternative to increasing fiber input power to achieve greater compression factors would be to increase fiber length instead of laser power.

4.5 Future prospects

Self-similar pulses

For reasons that will become apparent in the next subsection, self-similar pulses will be briefly described here. Self-similar pulses was first experimentally demonstrated and theoretically described by Fermann et al. (2000). The NLSE with gain and $\beta_2 > 0$ (relevant in fiber amplifiers and some fiber lasers) is given by

$$i\frac{\partial \tilde{E}}{\partial z} = \frac{1}{2}\beta_2\frac{\partial^2 \tilde{E}}{\partial T^2} - \gamma|\tilde{E}|^2\tilde{E} + i\frac{g}{2}\tilde{E}, \qquad (4.14)$$

where g is the gain. Equation 4.14 has asymptotic solutions with parabolic temporal intensity profiles and linear chirp. These solutions are called self-similar pulses. It should be noted that only the form of these pulses is preserved under propagation, the temporal width and the peak power increases with distance. The solutions can be written as (Fermann et al., 2000)

$$
\begin{aligned}
\tilde{E}(z,T) &= \tilde{E}_0(z)\{1 - [T/T_0]^2\}^{1/2}\exp[i\phi(z,T)] & (4.15)\\
\phi(z,T) &= \phi_0 + 3\gamma(2g)^{-1}\tilde{E}_0^2(z) - g(6\beta_2)^{-1}T^2 & (4.16)\\
\tilde{E}_0(z) &= 0.5(gE_{in})^{1/3}(\gamma\beta_2/2)^{-1/6}\exp(gz/3) & (4.17)\\
T_0(z) &= 3g^{-2/3}(\gamma\beta_2/2)^{1/3}E_{in}^{1/3}\exp(gz/3). & (4.18)
\end{aligned}
$$

Self-similar pulse evolution is promising, because it allows fiber amplifiers to be scaled to higher powers, extended beyond those attainable in chirped-pulse amplifiers, where nonlinearity sets the limit. (Limpert et al., 2002, 2006). Since the chirp of the self-similar solution is linear, the pulse can be efficiently compressed using standard pulse-compression techniques such as a grating pair.

Spectral compression of self-similar pulses

The Gaussian pulse-shape is not really optimal for spectral compression, because the SPM-induced frequency shift is not linear. This becomes especially apparent as one goes to larger chirps, where the gain in brightness becomes less and less (Fig. 4.1). The instantaneous frequency of a spectrally compressed Gaussian pulse is sketched in Fig. 4.7a.
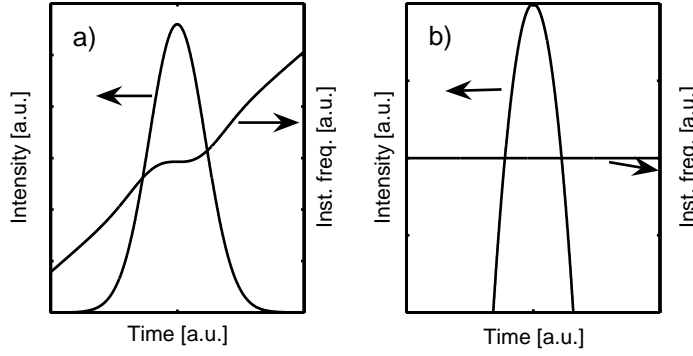
Figure 4.7: Sketch of (a) the intensity envelope and instantaneous phase for a spectrally compressed Gaussian pulse; and (b) same for a parabolic pulse.

It is expected that pulses from a self-similar amplifier are ideally suited for spectral compression, because they have a linear chirp, which can be compensated and a parabolic shape, which means that the SPM-induced frequency shift is linear. Inherent to the self-similar pulses is that as they propagate in an amplifier, they also increase the spectral width. So, if amplified narrow-band pulses are desired, self-similar amplifiers are a poor choice. Therefore, it seems useful to merge self-similar amplifiers with spectral compression to introduce flexibility in the spectral width and allow generation of truly transform-limited pulses with varying spectral widths. Parabolic pulses with linear, negative chirp can be made to compress down to the transform-limit, when letting SPM act on them. Ideally, the instantaneous frequency of a spectrally compressed parabolic pulse would look like the sketch in Fig. 4.7b.

The proposal for an experimental setup for spectrally compressing self-similar pulses would thus be to impose a (linear) negative chirp on the pulses exiting the amplifier using a pair of gratings and then send them through a PCF with $\beta_2 \approx 0$. Previous experiments have shown that the linear chirp of an amplified parabolic pulse can be almost completely compensated for by a grating pair. (Nielsen et al., 2005; Limpert et al., 2002). Thus it should also be possible to impose a linear, negative chirp using the very same grating pair to allow for spectral compression.

Another option would be to apply a pulse shaper (Weiner, 2000) to shape an arbitrary pulse into a parabolic pulse with negative chirp, prior to sending the pulse through a fiber to spectrally compress it. Like the approach with self-similar pulses outlined above, this approach is also

expected to result in spectrally compressed pulses that are transform-limited.

4.6   Discussion and conclusion

Other approaches to spectral compression

Other schemes for spectrally compressing pulses with high efficiency have been demonstrated. For instance by frequency mixing of two similarly chirped pulses (Veitas and Danielius, 1999; Osvay and Ross, 1999; Raoult et al., 1998). These schemes, however, are restricted by the phase-matching requirement to a relatively narrow bandwidth and can only be efficiently performed with high-intensity laser pulses. The solution of SPM-induced SC in PCFs as described in this chapter is more generally applicable, especially to low-intensity pulses.

Conclusion

The spectrum of a Gaussian pulse can be compressed significantly by sending it through a PCF. The resulting pulse is close to being transform-limited but has residual chirp on the leading and trailing edge. It was investigated, analytically and numerically, how spectral compression scales with pulse energy, pulse duration, and initial spectral width. The experiments done were nicely described by the theory, and the best achieved compression factor was 28, from 280 to 10 cm^{-1}, which corresponds to a brightness increase of 17. It is expected that future work using parabolic rather than Gaussian pulses will provide spectrally compressed pulses without residual chirp which are closer to the transform-limit than in the case of Gaussian pulses. The ability to produce a near-transform-limited ps pulse is a significant step towards a CARS light source based on a single fs-laser, because it can be employed as a pump pulse in CARS microspectroscopy as will become apparent in Chap. 6.

Chapter 5

Red-shifted Stokes pulse

5.1 Introduction

This chapter will present my work on the development of new ways of generating light pulses with PCFs that can be used as a Stokes pulse for CARS microspectroscopy. The laser that will be used throughout the chapter is a Ti:sapphire fs-laser oscillator with a repetition rate of 76 MHz.

A Stokes pulse for CARS microspectroscopy should fulfill some requirements, which have been discussed in Chap. 3. It is stressed that this chapter is dealing with the generation of a Stokes pulse for CARS microspectroscopy rather than CARS microscopy, *i.e.* the Stokes pulse must be broadband. The ability to span a spectral region from ν_p to $\approx \nu_p - 3500$ cm^{-1} is crucial in that is makes it possible to adress molecular vibrations over the entire Raman spectrum of condensed samples. This ability can be achieved either by creating a broadband Stokes pulse that spans the entire region (800 nm-1100 nm with a Ti:Sapphire laser as pump), or by creating a Stokes pulse that can simply be tuned across the entire region. The temporal shape - most importantly the temporal duration - has an impact on the CARS signal intensity. The duration should be smaller than the pump pulse duration. The temporal and spectral stability should be good. Most important is the long-term stability (minutes), which should be good enough that nothing drifts during an image acquisition. On the very fast timescale, fluctuations, if any, should average out. We are dealing here with a light source based on a single, unamplified laser, which means that both the available average power and peak power is scarce, compared to most other pulsed laser systems, because part of the laser power must also go into creating the pump pulse. This means that the efficiency in creating the Stokes pulse must be as high as possible.

This chapter is arranged as follows. Section 5.2 will briefly describe attempts done by us at employing continuum generation in 3 different PCFs to create a Stokes pulse; Sec. 5.3 discusses the question of the coherence properties of supercontinua; Sec. 5.4 describes experimental results on a method to generate more well-defined, redshifted pulses in a PCF and gives a characterization of the method as a Stokes pulse source. Section 5.5 summarizes and concludes.

5.2   Continuum generation

The field of continuum generation in optical fibers is too complex to allow an in-depth description or review here. For the purpose of this thesis it suffices it to say that as people started studying continuum generation in PCFs, it was found that under some conditions, extremely wide and flat spectra could be produced when pumping with pulses at NIR wavelengths, such as 800 nm, the typical wavelength of the Ti:Sapphire laser. These new observations are coupled to the properties of PCFs discussed in Chap. 2; PCFs push the ZDW and the anomalous-dispersion regime down to NIR and visible regions, allowing FWM and soliton dynamics to take place in a wavelength regime, where lasers like Ti:Sapphire lasers (800 nm) or Nd-lasers (1064 nm) are available. That is, lasers that are present in numerous laboratories, serving other purposes.

The nonlinear effects causing the broad spectra (SPM, FWM, and soliton dynamics) are most often coupled and occur at the same time during propagation, so intuitive description of the generated spectra is often extremely difficult. Nevertheless, in the following subsections, it will be attempted to review each nonlinear effect separately by presenting continuum spectra from three different PCFs, where one effect is dominant.

Self-phase modulation

We have attempted to locate a PCF that generates a continuum broadened purely by SPM. Such a PCF should have normal GVD for all wavelengths; this arrests the two competing effects, because soliton formation requires anomalous dispersion, and FWM requires the presence of a ZDW. A typical broadened output of the PCF NL1050-NEG-1 from Crystal Fibre A/S is shown in Fig. 5.1a. The GVD curve of the PCF is seen in the inset. The core diameter is 2.3 μm and the nonlinear coefficient is $\gamma = 0.037$ (Wm)$^{-1}$. The GVD is numerically low in the NIR region, which helps to keep the spectrally broadened output short in time.
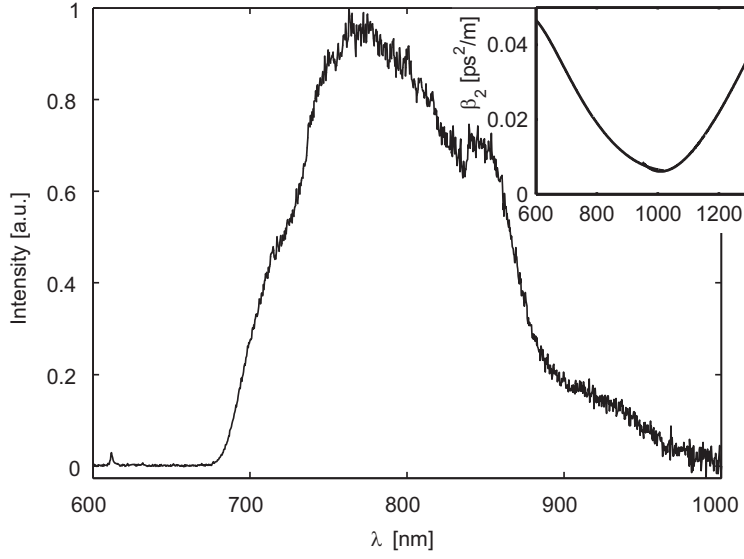
Figure 5.1: Typical output spectrum from 10 cm NL-1050-NEG-1 pumped with a near-transform-limited 800 nm pulse with $\Delta\nu = 340$ cm^{-1} and $P_{ave} = 350$ mW; (inset) dispersion curve of NL-1050-NEG-1. Dispersion data obtained from Crystal Fibre A/S.

The spectrum broadens to almost 200 nm spectral width. Most of the energy is on the blue side of the pump wavelength, the Stokes pulse is desired on the red side. The spectrum is extremely inhomogenous in the 800 nm-1100 nm-region, while the Stokes pulse should have high spectral density. The problem is fundamental to SPM. A rule-of-thumb for SPM-broadened spectra in fibers in the absence of GVD is, that the spectrum broadens by a factor (Agrawal, 1995)

$$\frac{(\Delta\omega)_{rms}}{(\Delta\omega)_0} = \left(1 + \frac{4}{3\sqrt{3}}\gamma P_0 z\right), \tag{5.1}$$

where $(\Delta\omega)_{rms}$ is the broadened pulse spectral rms-width and $(\Delta\omega)_0$ its initial rms-width. It is deemed that with the available peak powers from the Ti:sapphire oscillator, SPM alone can not produce the tunability required for the Stokes pulse.

Higher-order solitons

Accounts of continuum generation in the litterature have pointed out that soliton dynamics in a PCF can result in broader spectra than SPM
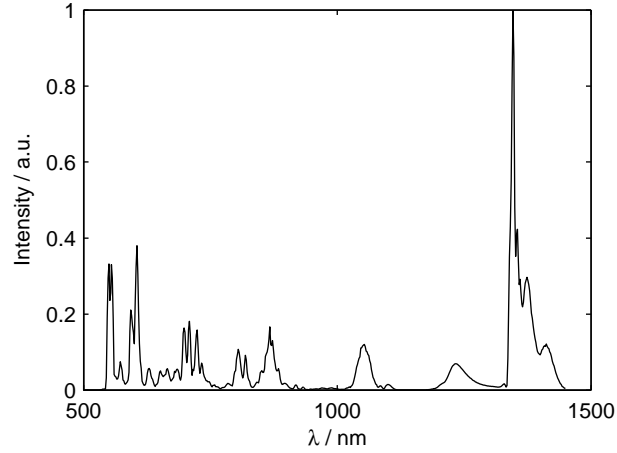
Figure 5.2: Typical output spectrum from PCF 2 pumped with a near-transform-limited 800 nm pulse with $\Delta\nu_0 = 470$ cm^{-1} and $P_{\text{ave}} = 215$ mW. The GVD curve of the fiber is shown in Fig. 4.3

alone. Therefore, we attempted to generate a continuum in a PCF that would allow soliton dynamics to occur. The PCF chosen for this was PCF 2 (introduced in Chap. 4).

In Fig. 4.3, the dispersion curve for this fiber is shown. There are two ZDWs at 750 nm and 1250 nm so the Ti:sapphire laser wavelength is in the anomalous GVD-region. In Fig. 5.2 is shown a typical continuum output. The spectra generated in this PCF are, already at low powers, very wide albeit quite spiky. This is characteristic for propagation in anomalous GVD (Agrawal, 1995). The most important broadening mechanism in this case is the formation of higher-order solitons. Due to the presence of higher-order dispersion, an Nth-order soliton breaks up into fundamental ($N = 1$) solitons accompanied by non-solitonic radiation. That is, energy that does not "belong" to the fundamental solitons is shed and emitted in the visible, phase-matched to the solitonic radiation. (Husakou and Herrmann, 2002). The fundamental solitons redshift under the soliton self-frequency shift (to be discussed in Sec. 5.4), further broadening the spectrum. The spectral density is highest at the spectral positions of the fundamental solitons. And the spectral density is fixed by the relation $1 = N^2 = (\gamma P_0 \tau_0)/|\beta_2|$. As will become apparent in Sec. 5.4, this continuum approach cannot really rival selective "excitation" of a single, fundamental soliton. The inhomogeniety and excessive spectral width of the output pulses from this kind of PCF are prohibitive for their use as Stokes pulse.
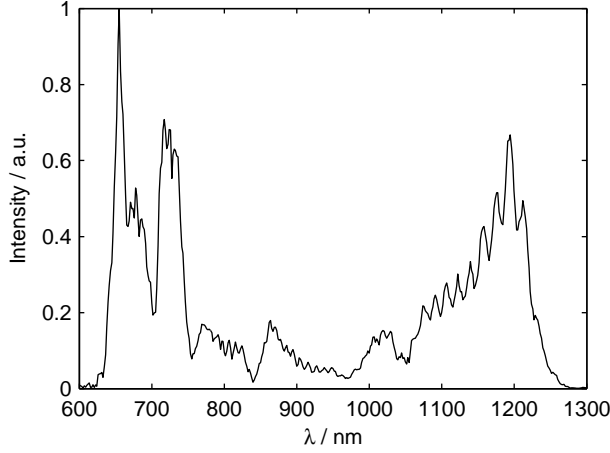
Four-wave mixing

Figure 5.3: Typical output spectrum from NL-800-PM-testfiber #
5 pumped with a near-transform-limited 795 nm pulse with $\Delta\nu_0$
= 470 cm^{-1} and P_{ave} = 312 mW. The GVD curve for the fiber is
shown in Fig. 4.3

In the litterature, FWM has been identified as another broadening
effect in continuum generation that can result in broader spectra than
SPM and flatter spectra than soliton dynamics. We therefore sought
a PCF in which FWM would be the dominant effect. FWM can be
favoured over soliton dynamics and SPM by letting the laser wavelength
be close to a ZDW. The reason for this is that the gain and the gain
bandwidth for degenerate FWM is maximized when this is the case
(details about the gain will be discussed in more detail in Chap. 8).
For this purpose, we chose PCF 1 (introduced in Chap. 4. In Fig. 4.3,
the dispersion curve for this fiber is shown. There are two ZDWs at 830
nm and 1030 nm. In Fig. 5.3 is shown a typical output spectrum for
this fiber. The spectrum does span the entire 800 nm - 1100 nm region
and is more flat than the spectrum generated by PCF 2. But most
of the energy is located outside this region. The gain for degenerate
FWM, over which one has little control, because it is decided by the
PCF GVD curve, plays a decisive role in this. But the influence of
soliton dynamics is propably still present as a contributing factor to
the low spectral density in the region 830 nm - 1030 nm between the
ZDWs - because solitons created in this region redshift up to the red
ZDW.

Of the PCFs discussed in this section, this one represents the most

suitable for the continuum approach to generating a Stokes pulse for CARS microspectroscopy. In the spectrum in Fig. 5.3, the average spectral density is $\approx 2 \cdot 10^{-13}$ J/cm^{-1} assuming 40 % transmission. But in the 800 nm - 1100 nm region, it is much lower $\approx 4 \cdot 10^{-14}$ J/cm^{-1}.

5.3   Stability

Coherence

The complex nonlinear evolution of fiber-generated continua raises a valid question of their stability and coherence. This problem is treated in several papers (Kubota et al., 1999; Dudley and Coen, 2002). In these papers, the pulse-to-pulse coherence is examined by numerical simulations The general find is that when pumping in the normal GVD region, there is nearly perfect pulse-to-pulse coherence. On the other hand, when pumping in the anomalous region, pulse-to-pulse coherence degrades rapidly as the pulse transform-limited duration increases. The criticial pulse duration is approximately 100 fs. The reason for coherence degradation is an interplay between modulation instability and soliton dynamics. Modulation instability can amplify small, random fluctuations in the input power, which means that the initial conditions for the further pulse evolution can be very different from pulse to pulse. This means that the concurrent soliton breakup can also vary significantly from pulse to pulse. This can be remedied to a certain extent by using shorter input pulses, which reduces the soliton number and hence the unceartainty in the final pulse.

Of the continuum-generating PCFs mentioned in this chapter, the discussion about coherence is relevant to PCF 2, because spectral shaping in that PCF depends on higher-order solitons.

It is important to notice, though, that poor interpulse coherence needs not be detrimental to CARS signal generation. Interpulse coherence degradation basically means that two consequtive pulses are not similar in time and frequency, rather, they fluctuate. If a Stokes pulse with poor interpulse coherence is employed, and the fluctuations are fast and random, they should in principle average out, so as to leave the generated CARS spectra unaffected, if the acquisition time is long enough. And - indeed - there are reports from groups, who have generated continua in PCFs with anomalous GVD and employed them as Stokes pulses in CARS microspectroscopy. (Kee and Cicerone, 2004; Kano and Hamaguchi, 2005b,a,c, 2006a,b; Ivanov et al., 2006; Sidorov-Biryukov et al., 2006).

Fiber damage

Another degradation effect that has been found in continuum generation is the long-term degradation of the ends of the PCF. Short, high-intensity pulses are used, which damage the fiber ends over the course of days or weeks. It is not fully understood, what actually causes this damage, but most likely, dust gets burnt onto the fiber endface after having been sucked in by the optical tweezer effect of the focussed input beam.

5.4 Soliton self-frequency shift

Introduction

This section will describe a means of generating a Stokes pulse that does not rely on continuum generation but on an isolated nonlinear effect, the SSFS. SSFS was mentioned briefly in Sec. 5.2 and Sec. 2.5. The advantages of this approach are: A fundamental soliton redshifts under the SSFS, and the redshift relative to the original frequency can be very large (4000 cm^{-1} or more), thus spanning the entire Raman spectrum. A large portion of the input energy is converted into the redshifted soliton, ensuring large spectral density (relative to the input energy). The high conversion efficiency frees up energy for the pump pulse. And the risk of damaging the PCF end facet decreases, because lower input power is used. And the temporal characteristics of the redshifted pulse are more well-defined and can be understood in a more straightforward way than the continuum approaches outlined above.

Experimental

A PCF, "NL-800-PM-testfiber #4", henceforth denoted PCF3, is employed here, which has ZDWs at 760 nm and 1165 nm, core diameter of $d = 1.8~\mu$m, and a nonlinearity parameter of $\gamma = 0.090$ (Wm)$^{-1}$. A first order soliton can be generated in a fiber with negative β_2. The soliton order, N, is given by $N^2 = 0.321(\gamma P_0 \tau_{fwhm}^2)/(|\beta_2|)$, where P_0 is the soliton's peak power and τ_{fwhm} its duration. The percentage of the input laser pulse that is converted to the first-order soliton is determined by its overlap with the soliton. Just exactly how large a portion of the input pulse goes into forming the fundamental soliton is not a trivial question to answer, because soliton dynamics occurs in both the time-domain (nonlinearity) and the frequency domain simultaneously (dispersion), and because there is higher-order dispersion, due to which, a soliton is only an approximate solution. But, most often, a majority of the input light goes into forming a fundamental soliton, if only $N \approx$
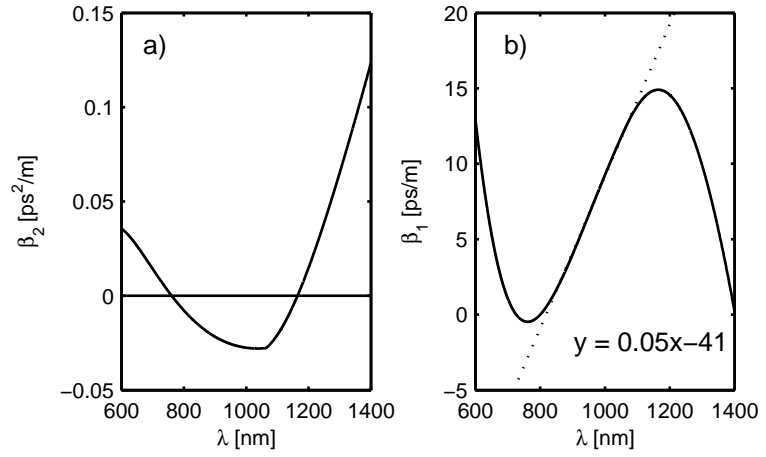
Figure 5.4: (a) GVD curve for the fiber NL-800-PM-testfiber #4 (PCF3); (b) β_1 for the same PCF. The dashed line is a fit to β_1 in the 800 nm-1100 nm region. Dispersion data obtained from Crystal Fibre A/S.
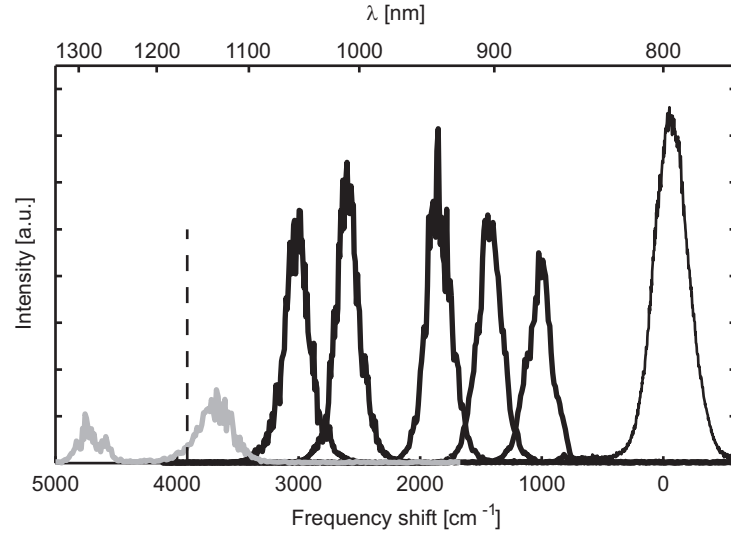

Figure 5.5: Spectra of Stokes pulses. (Thin solid line) spectrum of the laser; (thick solid lines) spectra of six different Stokes pulses; the grey line consists of a solitonic and a dispersive part. The vertical dashed line denotes the ZDW.
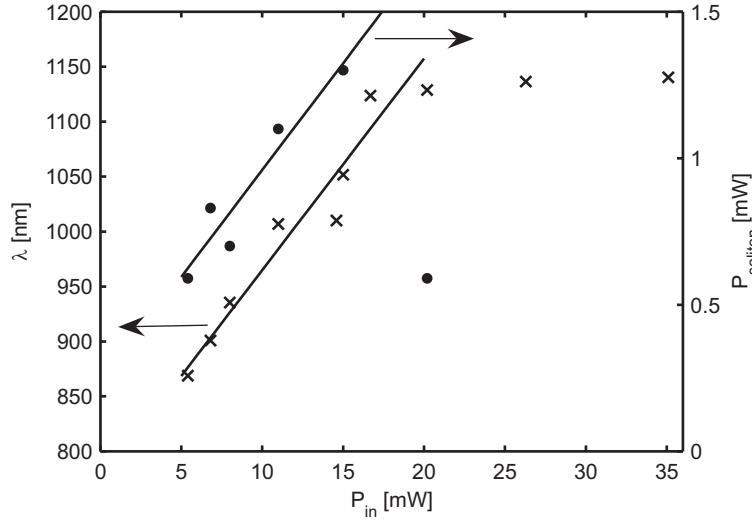
Figure 5.6: Redshifted soliton wavelength (crosses) and power (dots) versus input power

1. For short pulses, efficient intrapulse stimulated Raman scattering occurs, where the blue parts of the pulse act as Raman pump for the red parts. On the same time scale, soliton dynamic acts, maintaining the solitonic shape of the (redshifted) pulse, resulting in the adiabatic, continous red-shift of the soliton along the length of the fiber.

The input pulse at 800 nm comes from the Ti:sapphire laser oscillator and is close to the transform limit with a FWHM duration of $\approx 60 fs$, measured by interferometric autocorrellation.

It is found that a practical Stokes pulse light source can be realized by employing a 190 cm-long piece of PCF3. For typical values of input pulse energy and spectral width FWHM of 100 pJ and 350 cm^{-1}, respectively, a first-order soliton is formed at 800 nm that redshifts down the length of the fiber. The redshift is controlled by varying the fiber input power. Fig. 5.5 shows an ensemble of six different redshifted pulses along with the input pulse spectrum. The soliton stops redshifting upon reaching the red ZDW. When the redshifting soliton reaches the red ZDW, a part of the soliton energy is shed as a dispersive wave on the other side of the ZDW. Figure 5.6 shows the dependency between the red-shift and power. A redshift of almost 4000 cm^{-1} can be achieved, which allows the pump-Stokes frequency difference to span most of the vibrational Raman spectrum. Figure 5.6 shows the redshift and the soliton average power vs. PCF input power. The conversion

efficiency decreases with redshift. There are several reasons for this. First, energy is lost to the lattice as an intrinsic consequence of the Raman process. Secondly, as pulse power is increased to obtain higher redshift, N increases, and a smaller percentage of the input pulse goes into forming the first-order soliton. The total energy in the red-shifted pulse is low, < 10 pJ, but the conversion efficiency is excellent, ≈ 10 %.

The redshifted pulse in our experiment has a spectral density of approximately $3 \cdot 10^{-14}$ J/cm^{-1} with fiber input pulse energy of less than 15 pJ. This spectral density is comparable to the spectral density of the continuum generated by PCF1 (Sec. 5.2. The major difference is that continuum generation requires much more input power to generate that than the SSFS does.

Soliton stability - calculated

The temporal and spectral stability of the redshifted Stokes pulse should be considered. As it is apparent from Fig. 5.6, the center wavelength of the redshifted pulses is coupled to the input power and - because of dispersion in the fiber - so is the delay of the pulses. A fluctuation in laser power therefore mantifests itself as a fluctuation in the wavelength and delay of the Stokes pulse.

The dependency of group delay upon wavelength can be derived from a fit to Fig. 5.4b, and the dependency of the redshifted soliton's wavelength can be derived from a fit to Fig. 5.6. With these dependencies known, the law of propagation of errors can be used to relate the standard deviation on the soliton center wavelengths, $\sigma(\lambda_S)$, and delay, $\sigma(\tau_S)$, to the standard deviation on the fiber input average power, $\sigma(P)$. We find:

$$\sigma(\tau_{soliton}) = 0.92 \frac{[ps]}{[mW]} \sigma(P_{in}) \tag{5.2}$$

$$\sigma(\lambda_{soliton}) = 19.3 \frac{[nm]}{[mW]} \sigma(P_{in}). \tag{5.3}$$

For typical parameters, $\lambda_S = 1050$ nm and $\sigma(P)/P = 0.01$ (according to the operator's manual for the Mira Ti:sapphire laser, Coherent Inc.), these numbers are $\sigma(\tau_S) = 140$ fs and $\sigma(\lambda_S) = 2.9$ nm. The calculated uncertainty in λ_S is quite large compared to the spectral width of the soliton itself. But the uncertainty in delay is still well below the pump pulse duration. So it can be hoped that the spectral fluctuations will simply average out, if the CARS signal is averaged over enough pulses. It should be pointed out at this point, that it is quite important that the delay uncertainty be small. If the spectral fluctuation are accompanied

by large temporal fluctuations, the pump-Stokes overlap is affected, and different Stokes wavelengths are "weighted" differently, so that the CARS signal is no longer linear in the Stokes pulse.

5.5 Conclusion and outlook

Future prospects

At this point, it is evident that SSFS provides a Stokes pulse, which is widely tunable; temporally and spectrally well-defined; generated with high efficiency; and reasonably stable temporally and spectrally. What remains to address is the total soliton power. The soliton peak power is determined by $1 = N^2 = (\gamma P_0 \tau_{fwhm}^2)/(|\beta_2|)$, *i.e.* is intrinsically limited by PCF parameters. And as can be seen from Fig. 5.6, the corresponding average power is in the mW-range. This is not a lot for CARS microspectroscopy, at least a factor 10 more is desired. Ideally, the Stokes pulse power should be just below the damage threshold for the sample under study in order to maximize the CARS signal.. Higher pulse energy could be reached by decreasing the ratio $\gamma/|\beta_2|$ in order for N to remain invariant equal to 1. Preferably, the ratio should be improved by decreasing γ, because increasing β_2 would likely lead to increased temporal fluctuations. The current problem is, that γ and β are not independent; increasing γ by decreasing the PCF core size typically leads to a numerically increased β_2 because of increased waveguide dispersion.

Another approach for increasing Stokes power would be to devise some kind of amplification using the redshifted soliton as a seed. For example in a non-collinear optical parametric amplifier (Aguergaray et al., 2007). If the redshifted soliton could be amplified over the entire range 800 nm-1100 nm, this would significantly push the light source in the direction of practical applications.

Conclusion

Various ways of generating a Stokes pulse for CARS microscopy based on a Ti:sapphire oscillator and PCFs were presented. Results on continuum generation in three different PCFs representing three different predominant broadening mechanisms were presented. With the fiber PCF1, a broad, reasonably flat and stable continuum could be generated that was suited for a Stokes pulse. An alternative way of generating a Stokes pulse through the SSFS in a PCFs was then described and characterized. This approach can deliver tunable, stable, transform-limited Stokes pulses with durations $\approx$ 50 fs and spectral density comparable

to those obtained by continuum generation. Fundamental limitations to the soliton peak power were discussed.

Chapter 6

Single Ti:Sapphire laser

6.1 Introduction

This chapter will first attempt to characterize one of the two single-laser light sources for CARS microspectroscopy devised in this thesis; the one relying on a Ti:Sapphire laser oscillator, a spectrally compressed pump pulse, and a redshifted soliton Stokes pulse. Second, a proof-of-principle experiment will be briefly given on an alternative scheme, selective excitation, which uses the same light source, but with pump and Stokes pulses tailored in a different way. This chapter proceeds by describing the experimental setup in Sec. 6.2; then, an example of CARS microspectroscopy with the present light source is given in Sec. 6.3; the effects of using a non-transform-limited pulse as pump pulse are investigated in Sec. 6.4; the detection sensitivity is discussed in Sec. 6.5, and measurements on dilute samples are presented in Sec. 6.6; Sec. 6.7 presents the proof-of-principle of the alternative approach of selective excitation; finally, Sec. 6.8 will summarize and conclude.

6.2 Setup

The setup is sketched in Fig. 6.1. The same Ti:Sapphire laser as in chapters 4 and 5 is employed. 30 cm PCF1 and ≈ 190 cm PCF3 were used. The laser output is split in two by a beamsplitter. A prism pair with interprism distance 190 cm imposes a negative chirp on one part, resulting in negatively chirped pulses of 1.9 ps duration FWHM, the spectral width FWHM was 15 nm at 810 nm. The chirped pulse is then spectrally compressed in PCF1. The other, transform-limited part is coupled into PCF3 to produce the red-shifted Stokes pulse. A graded neutral-density filter provides control over the input power and hence over the redshift. The pump and Stokes pulses are combined on
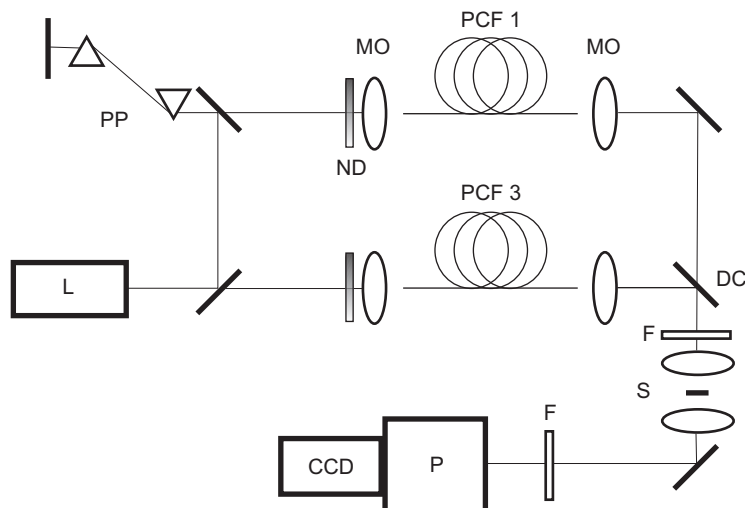
Figure 6.1: Setup. (L) laser; (BS) beam splitter; (PP) prism pair; (MO) microscope objective; (ND) graded neutral-density filter; (PCF) photonic-crystal fiber; (DC) dichroic mirror; (F) filters; (S) sample mounted on a 3D piezo stage; (P) polychromator; (CCD) CCD camera.

a dichroic mirror and focussed onto the sample using a 20x 0.50 NA microscope objective. This step takes place in a commercial inverted microscope adapted for CARS. The CARS signal is collimated by another microscope objective and sent through a polychromator, after which the spectrum is detected by a CCD camera.

6.3   Example of microspectroscopy

Figure 6.2 shows an example of a CARS image of a yeast cell fixed on an APES-covered glass coverslip. Examples of spectra at three different positions inside the cell are also shown, both before and after subtraction of the background signal from the surrounding water. Note that spectra (e,f,g) are not the normalized signal S. They are the raw CARS spectra where the spectrum of water has been subtracted. The spectra have not been divided by the water signal, because this only really makes sense in the dilute limit and introduces a lot of noise. At position 1, only background signal from water contributes to the CARS signal. In the interiour of the cell, at position 2, the spectrum is clearly different, with a peak appearing at ≈ 2900 cm^{-1}, indicative of C-H bonds. The ultimate aim of CARS microspectroscopy would be
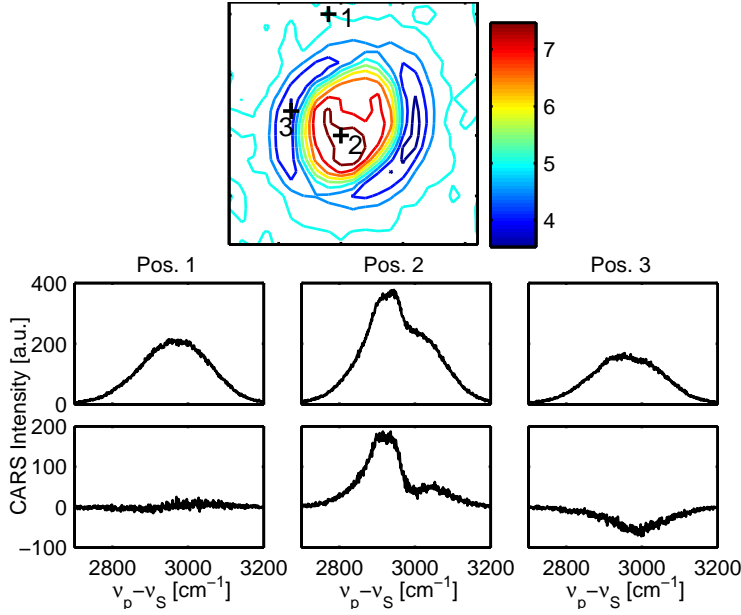
Figure 6.2: (a) 10×10 μm^2 image of the spectrally integrated CARS signal from a yeast cell; crosses indicates the origin point of the spectra below. Acquisition time per pixel was 0.1 s; $P_p = 55$ mW; $P_S \approx 0.5$ mW; $\lambda_p = 796.4$ nm. (b,c,d) raw CARS spectra; (e,f,g) spectra in (b,c,d) with water signal subtracted.

to do quantitative chemical imaging. In this case, however, it is not immediately apparent how one can achieve this. Quantitative analysis requires a normalized spectrum S which is proportional to $\chi_r^{(3)}$, and this in turn requires a perfect reference measurement of the nonresonant background. And this is the problem, because it cannot be assumed that $\chi_{nr}^{(3)}$ is constant throughout the sample. This is exemplified by the spectrum at position 3 - the background-subtracted signal is actually negative. This could be due to differences in $\chi_{nr}^{(3)}$. It could just as well be caused by shadow, refractive, or interference effects. But in any case, it is non-trivial to acquire an unamiguous nonresonant reference spectrum. To compensate for this, one might assume that the nonresonant signals in all pixels have the same frequency dependence, *i.e.* they are proportional. This way, the nonresonant spectrum would have to be multiplied by some constant prior to doing the normalization. But this would rely on subjective judgement, which rules out a rigourous, automated deconvolution of CARS spectra.

6.4   Impact of residual chirp

Due to the nonlinear chirp of the spectrally compressed pump pulse, it should be considered, which detrimental effects this might have on CARS spectra.
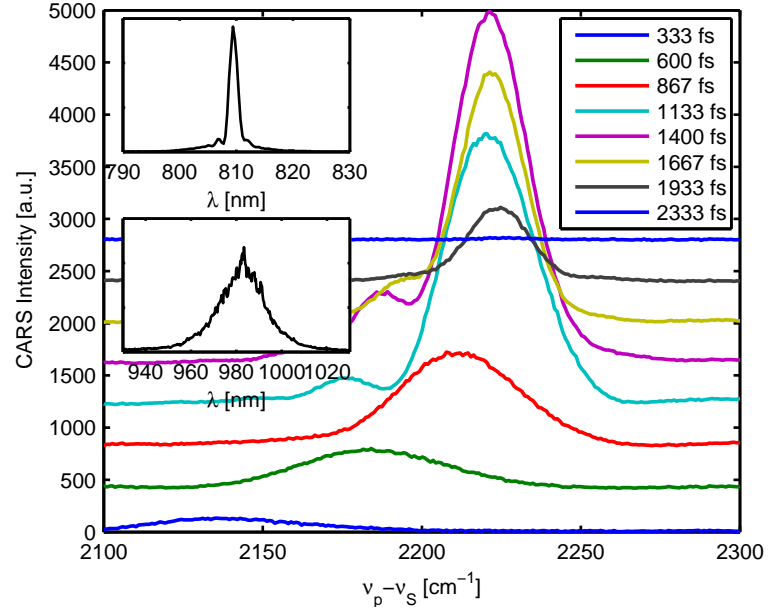
Measurements, benzonitrile

Figure 6.3: Raw CARS spectra of benzonitrile at different pump-Stokes delays. (Top inset) pump spectrum; (bottom inset) Stokes spectrum; (legend) pump-Stokes delay. Acquisition time was 1s.

The Raman spectrum of benzonitrile has a single, narrow peak at 2229 cm^{-1} owing to the C≡N vibration. The CARS spectrum should thus also only display a single peak. This simplicity makes the molecule good for diagnostics purposes. Figure 6.3 shows CARS spectra of benzonitrile taken at different pump-Stokes delays, $\tau_p - \tau_S$. The larger $\tau_p - \tau_S$, the later the pump pulse arrives relative to the Stokes pulse. Several points can be made from Fig. 6.3.

Remember first that the pulse is essentially negatively chirped (blue components on the leading edge and red components on the trailing edge), but at the center the instantaneous frequency is constant. The instantaneous frequency was sketched in Fig. 4.7a. At small $\tau_p - \tau_S$,
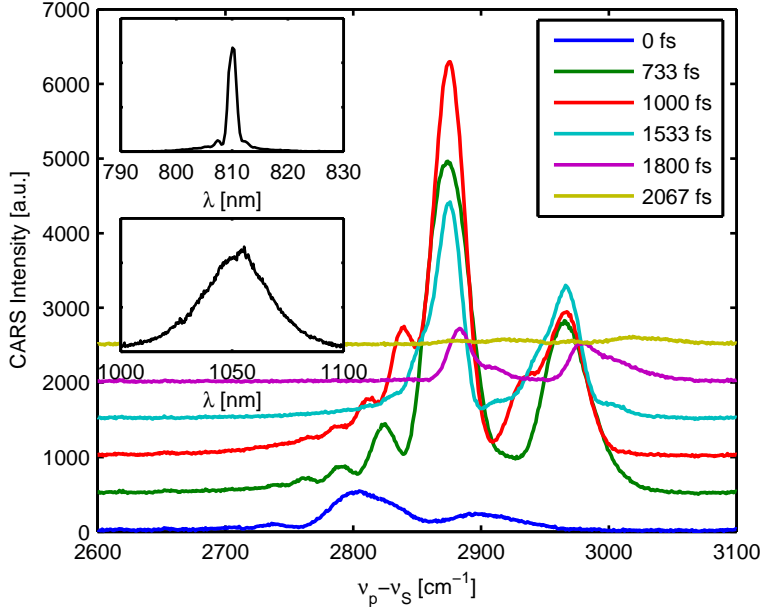
Figure 6.4: Raw CARS spectra of methanol at different pump-Stokes delays. (Top inset) pump spectrum; (bottom inset) Stokes spectrum; (legend) pump-Stokes delay. Acquisition time was 1 s.

the CARS spectrum is very redshifted. This is caused by the fact that in this case, the pump pulse arrives before the Stokes pulse, which then only interacts with the trailing edge of the pump pulse, which contains red spectral components. The opposite happens, albeit to a lesser degree, at large $\tau_p - \tau_S$. The lesser effect is due to the fact that the second-order polarization induced at the pump-Stokes overlap on the leading edge is now probed by the center of the pump pulse, where the instantaneous frequency is constant; hence the blueshift at large $\tau_p - \tau_S$ is smaller than the redshift at small $\tau_p - \tau_S$.

Second, it is apparent from the spectra, that the instantaneous frequency of the pump pulse at the center is indeed constant: The position of the peak remains virtually unchanged over an 800 fs-range of pump-Stokes delay.

Last, it can be observed, that small additional features appear on the red side of the largest peak. They appear as little peaks that grow smaller, the larger the pump-Stokes delay. Side-peaks like these appear generally in CARS when a chirped pulse interacts with the induced second-order polarization, and their origin is thus linked to the residual

chirp on the pump pulse.

Measurements, methanol

Figure 6.4 shows CARS spectra of methanol in the 2900 cm^{-1}-region at different pump-Stokes delays. The Raman spectrum of methanol in that region is slightly more complex than the one of benzonitrile, having several peaks, though two dominant ones of slightly larger width than benzonitrile.

The conclusions that can be drawn from these spectra mimic the ones in the previous subsection. The CARS spectrum is redshifted at small $\tau_p - \tau_S$ and blueshifted at large $\tau_p - \tau_S$. The peak positions are unaltered over ca. 800 fs. And there are little side-peaks on the red side of the peaks. In this case, though, they are more closely spaced than in the case of benzonitrile. This is due to the shorter decoherence time of methanol as compared to benzonitrile.
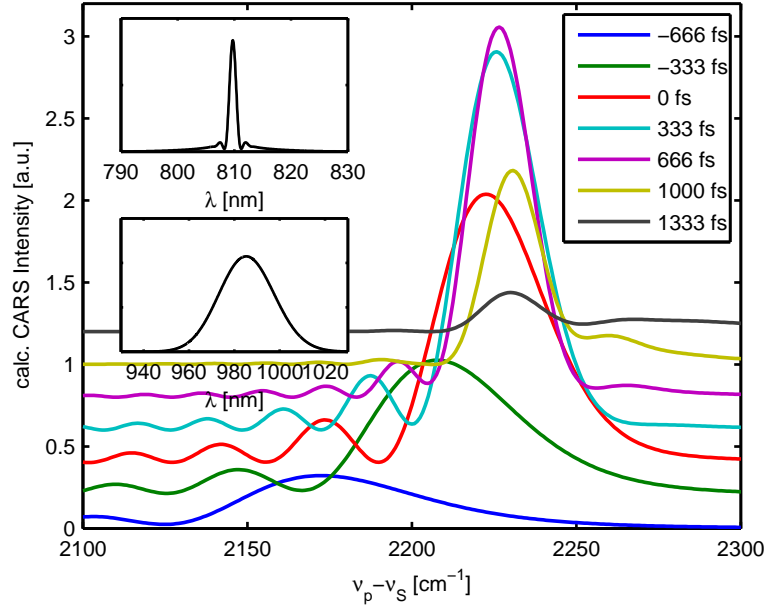
Calculations

Figure 6.5: $\lambda_p = 810$ nm; $\lambda_S = 985$ nm; $\tau_{0,fwhm,p} = 64$ fs; $\tau_{fwhm,p} = 1.9$ ps; $\tau_{0,fwhm,S} = 50$ fs; $\Omega_{vib} = 2229$ cm^{-1}; $\Gamma_{vib} = 9.9$ cm^{-1}.
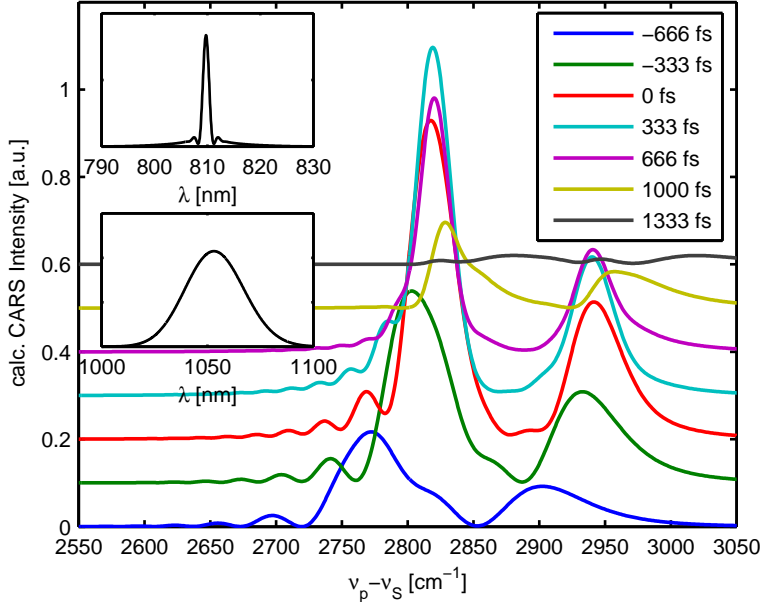
Figure 6.6: $\lambda_p = 810$ nm; $\lambda_S = 1053$ nm; $\tau_{0,fwhm,p} = 64$ fs; $\tau_{fwhm,p} = 1.9$ ps; $\tau_{0,fwhm,S} = 50$ fs; $\Omega_1 = 2825$ cm^{-1}; $\Gamma_1 = 25$ cm^{-1}; $\Omega_2 = 2940$ cm^{-1}; $\Gamma_2 = 38$ cm^{-1}.

To substantiate the claims in the previous two subsections, we attempt to perform a series of calculations using the method outlined in Chap. 2, *i.e.* using Eq. 2.23 and 2.26, the method is incorporated in the Matlab script in App. B.

In Fig. 6.5 and 6.6 the results of calculations of CARS spectra of benzonitrile and methanol are shown. It has been attempted to match the parameters of the calculations as closely with the experimental parameters as possible. The line centers and line widths were deduced from Raman spectra. The pump pulse was modelled as a linearly chirped pulse with identical duration, center wavelength, and spectral width as in the experiment. This pulse was then numerically subjected to SPM, the same way it was done in Sec. 4.3, to form the spectrally compressed pump pulse. The Stokes pulse was modelled as a transform-limited (Gaussian) pulse with spectral width and center wavelength idential to the experiment. Parameters are listed in the figure captions. The calculated spectra show good qualitative agreement with the measured spectra; they display a redshift for small $\tau_p - \tau_S$ and blueshift for large $\tau_p - \tau_S$; peak positions are unaltered in a ≈ 700 fs-range; and the qualitative behaviour of the chirp-induced, redshifted

side-peaks is well-reproduced. The period of the side peaks is longer for benzonitrile, and the peaks are smallest for large pump-Stokes delays.

A quantitative comparison between measurement and calculation has not been attempted, because the large parameter space and the coupling between the parameters renders quantitative comparison somewhat arbitrary. The examples above have merely gone to show that all the features of CARS spectra acquired using complex pulse shapes can be explained. It is expected that if all the relevant parameters (instantaneous frequencies, pulse shapes, linewidth, etc.) were known, the calculations would match the measurements.

6.5   Seeking the sensitivity limit

Introduction

The question of how sensitive CARS is or, equivalently, how small dilutions of a certain molecule can be detected, comes down to a question of signal-to-noise ratio (introduced in Sec. 3.4). This section will adress the sensitivity limit for the single laser-based setup described earlier in this chapter. The sensitivity limit can not simply be given as a single number, because many parameters contribute to the resonant/nonresonant ratio and the background (noise). Here, a semi-empirical approach will be taken. The scaling of the signal-to-noise (S/N) ratio with most relevant parameters is known: Acquisition time, pump and Stokes power, concentration, and resonant and nonresonant susceptibilities. So a reference measurement of a pure "solute" and a pure "solvent" will be taken. From this, a proportionality constant can be determined and the S/N ratio as a function of the stated parameters can be deduced. C-H bonds are very abundant in (organic) molecules and a they typically generate a strong CARS signal. The most abundant solvent in (biological) samples is water. Hence, we choose the reference solute to be methanol and the reference solvent to be water.

Scaling of S/N ratio

The CARS signal from a solution (S_{aS}) of concentration c (normalized molar fraction) and the reference CARS signal from a sample of pure solute (S_{ref}) scale as

$$
\begin{align}
S_{aS} &\propto tP_p^2 P_S |c\chi_r + (1-c)\chi_{nr}|^2 \tag{6.1}\\
&= tP_p^2 P_S (2c\mathrm{Re}[\chi_r]\chi_{nr} + \chi_{nr}^2) \tag{6.2}\\
S_{ref} &\propto tP_p^2 P_S \chi_{nr}^2 \tag{6.3}
\end{align}
$$

for small c. The normalized CARS signal S then scales as

$$S \;=\; \frac{S_{aS} - S_{ref}}{S_{ref}} \qquad (6.4)$$

$$\propto\; 2c\frac{\text{Re}[\chi_r]}{\chi_{nr}}, \qquad (6.5)$$

The most optimistic estimate for the noise is, when the measurement is Poisson-limited. By using the law of propagation of errors and letting $\sigma(S_{aS}) = \sqrt{S_{aS}}$ and $\sigma(S_{ref}) = \sqrt{S_{ref}}$, the noise of the normalized CARS signal S can be found, $\sigma(S)$ is then

$$\sigma(S) = \frac{\sqrt{2}}{\sqrt{S_{ref}}}, \qquad (6.6)$$

for very small c. and consequently, the signal-to-noise level is

$$\frac{S}{\sigma(S)} \propto \sqrt{2}c\sqrt{t}\sqrt{P_S}P_p\text{Re}[\chi_r]. \qquad (6.7)$$

With the scaling of the S/N ratio Eq. 6.7 known, a reference measurement can determine the proportionality factor in the equation.

Measurement

A CARS spectrum of pure methanol and pure water were acquired with acquisition times 1 s. The maximum CARS signals were 3500 counts and 250 counts, so $\sigma(S) = 0.066$. These numbers were used to calibrate the numeric model of methanol from Sec. 6.4 (App. B), such that the model reproduced the ratio and absolute signals. As a measure of S, we will use $S_+ - S_-$, defined as the difference between the maximum and minimum values that pertains to a given vibration in the spectrum of S.

Model

The model gives $S_+ - S_- = 0.081$ at 2825 cm^{-1} and $S_+ - S_- = 0.051$ at 2940 cm^{-1}. The other parameters used in the model were $t = 1$ s; $P_p = 27$ mW; $P_S = 0.5$ mW; $c = 0.01$; The expression for the signal-to-noise ratio can then be written

$$\frac{S_+ - S_-}{\sigma(S)} \;=\; 6.52c\sqrt{t}\sqrt{P_S[\text{mW}]}P_p[\text{mW}]; \quad 2825\text{cm}^{-1}; \quad (6.8)$$

$$\frac{S_+ - S_-}{\sigma(S)} \;=\; 4.09c\sqrt{t}\sqrt{P_S[\text{mW}]}P_p[\text{mW}]; \quad 2940\text{cm}^{-1}. \quad (6.9)$$

$(S_+ - S_-)/\sigma(S) = 1$ corresponds to the situation, where the difference between the maximum and minimum of S for a given vibration is equal to the amplitude of the noise. So, if $(S_+ - S_-)/\sigma(S) = 1$ is taken as the limit for a visible feature in the normalized CARS signal S, the present experimental parameters would permit detection of a 0.008 volume fraction of methanol in water, if only Poisson noise contributed to the noise.

It is interesting to note that in the ideal case where Poisson noise is the only noise contribution, the signal-to-noise ratio does not depend on χ_{nr}; the solvent can have arbitrarily large χ_{nr} without changing the detection sensitivity. This conclusion should be changed a bit, though, in the non-ideal case, where there are other noise or background sources. Consider the case, where reading out a spectrum from the CCD camera, gives a one-time contribution to the noise, "readout noise", and a background contribution from *e.g.* ambient light to the CARS signal that grows linearly in time,

$$\sigma^2(S) \to \sigma^2_{Poisson}(S) + \sigma^2_{readout} + a_{bg}t. \tag{6.10}$$

In this case, a large χ_{nr} is actually beneficial, because it decreases the relative importance of the (constant) readout noise and the background noise.

In conclusion, it should be noted, that the signal-to-noise ratio is actually dependent on many more parameters than the ones that enter the equation above. Parameters like detector efficiency and temporal, spectral and spatial overlap, and focussing also have profound importance. Because these parameters are not easily measured, the most accurate prediction of sensitivity is propably obtained by following the approach of this section; by acquiring CARS spectra of pure solute and solvent under the relevant experimental conditions and from that, calculate the proportionality factor in the expression for signal-to-noise ratio.

In principle, it is possible to gain a factor $\sqrt{2}$ in signal-to-noise level if S_{ref} is known to absolute precision (because then only the noise on S_{aS} would contribute). When the Stokes pulse is generated by means of the SSFS (Sec. 5.4), it is known to have a sech^2-spectrum, which should produce a well-defined S_{ref}, if the pump pulse is well-defined (transform-limited ps-pulse). If that were the case, S_{ref} could be fitted with a sech^2-function and and the fit could be used in finding S. But this is just equivalent to measuring S_{ref} with long acquisition time, which would have the same effect.
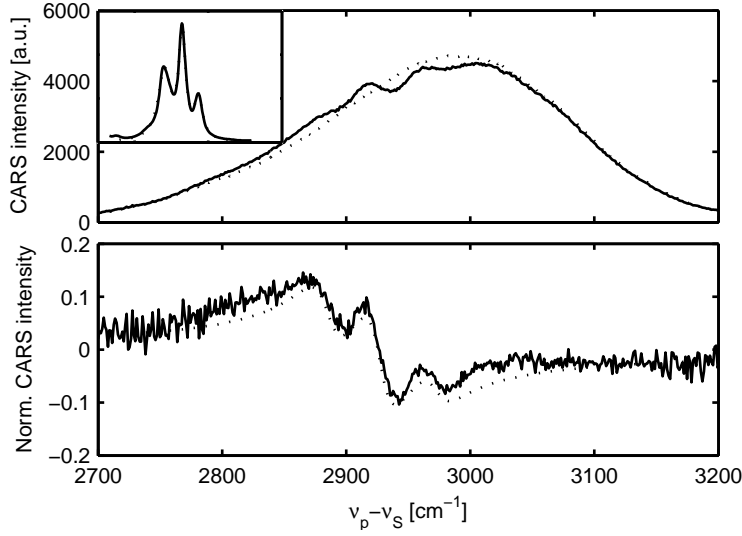
Figure 6.7: CARS microspectroscopy on a 4 vol% ethanol-water solution. (a) Raw CARS spectrum of the solution (solid); reference measurement on pure water (dashed), acquisition time was 2 s; (b) normalized CARS signal S (solid); fit of $\mathrm{Re}[\chi_r]$ with 3 resonances. The inset shows the Raman spectrum (solid line) and fit (dotted line).

	CARS	Raman
ν_1	2885	2881
Γ_1	16	21
ν_2	2927	2929
Γ_2	14	11
ν_3	2973	2973
Γ_3	15	13

Table 6.1: (Left) results of the fit to the normalized CARS signal and; (right) results of the fit to the Raman spectrum. Units are cm^{-1}

6.6 Measurements on dilutions

An example of a CARS spectrum of a dilute sample of 4 vol% ethanol in water is shown in Fig. 6.7. The normalized spectrum, S is also shown. According to Eq. 6.5, S is proportional to $\mathrm{Re}[\chi_r^{(3)}]$ in the dilute regime, so we attempt to fit the real part of a $\chi_r^{(3)}$ consisting

of 3 Lorentzians to it. As a comparison, we fit the imaginary part of a similar $\chi_r^{(3)}$ to the Raman spectrum of pure ethanol. The result of both fits is summarized in Table 6.1. The fit in Fig. 6.7b is not all too convincing. This could be caused by several factors. The non-transform-limited nature of the pump pulse is propably one (Sec. 6.4). It also can be completely ruled out that the Stokes pulse drifted during the acquisition of the two spectra, although it was checked that the Stokes spectra measured before and after the acquisition of the CARS spectra were identical. The model $\chi_r^{(3)}$ may be too simplistic; Raman peaks in the ethanol spectrum at ≈ 2700 cm^{-1} and ≈ 3200 cm^{-1} may have an influence on Re$[\chi_r^{(3)}]$ in the 2900 cm^{-1}-region. Apart from the imperfect fit, the agreement of peak positions and linewidths is fairly good.

6.7   Spectral focussing

Introduction

There are some important distinctions to be made between CARS microscopy and CARS microspectroscopy. In CARS microscopy, two (transform-limited) picosecond pulses are used, this provides optimized signal from one particular vibrational and allows for rapid spatial scanning with minimum laser power on the sample. Microspectroscopy, on the other hand, employs picosecond and femtosecond excitation to acquire CARS signal at many frequencies simultaneously. This was discussed in Chap. 3,

It has been reported that a broadband laser approach, where both pump and Stokes pulses are fs-pulses, can be merged with CARS microscopy by imposing similar chirps on two broadband (femtosecond) pulses. Particularly, in Hellerer et al. (2004) a chirped pump pulse of 12.4 ps duration and a Stokes pulse of 5 ps duration from a 250 kHz regeneratively amplified laser system and OPA were used. This way, the entire energy in the broadband pulses gets "focussed" on a frequency window much narrower than the pulse bandwidths. It should thus be noted that spectral resolution in this case comes from the selective "excitation" of a narrow window of frequencies, just as it is the case in CARS microscopy (ps pump and Stokes). In contrast, CARS microspectroscopy derives its spectral resolution from narrowband probing. The approach of chirping both pump and Stokes pulses is termed "spectral focussing" and, in principle, opens for rapid microscopy with broadband pulses. It is expected that, ideally, spectral focussing and CARS microscopy can be directly compared, *i.e.* for similar pulse durations and pulse powers, the generated CARS signals should be similar.
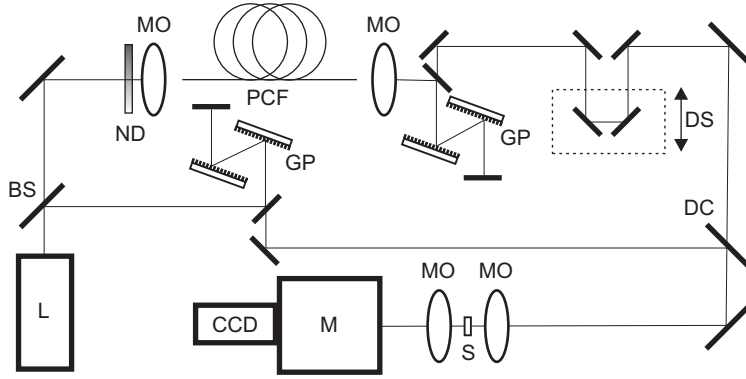
Figure 6.8: Experimental setup for CARS with two chirped pulses. L: Laser; BS: Beam splitter; ND: Graded ND filter; MO: Microscope objective; GP: Grating pair (600 lines/mm); DS: Delay stage; DC: Dichroic mirror; S: Sample; M: Monochromator; CCD: cooled CCD camera.

We have tried to build a setup similar in principle to that of Hellerer et al. (2004) with the exception that we will be using as Stokes pulse a redshifted soliton. This serves the purpose of demonstrating that spectral compression is not nessecarily essential to achieve spectral resolution in our single-laser setup.

Experimental setup

The setup is detailed in Fig. 6.8. The laser is the same Ti:sapphire oscillator that was used in earlier sections, and the Stokes pulse is generated by the SSFS in the same way as previously described. The broadband fs laser pulse thus functions as pump pulse and the broadband redshifted soliton as the Stokes pulse. They are separately given negative chirps by grating pairs. They are focused onto the sample and the generated CARS signal is detected through a monochromator by a CCD camera. The monochromator serves the purpose of discriminating against background light, a photomultiplier tube and band filters could just as well be used, since we are only interested in the spectrally integrated intensity. The sample is chosen to be methanol because of its simple spectrum with two distinct peaks.

In order to test whether the chirps are actually similar, we acquire a spectrum of methanol by scanning the pump-Stokes delay. This amounts to scanning the instantaneous pump-Stokes frequency difference. If the chirps are matched, the integrated intensity vs. delay
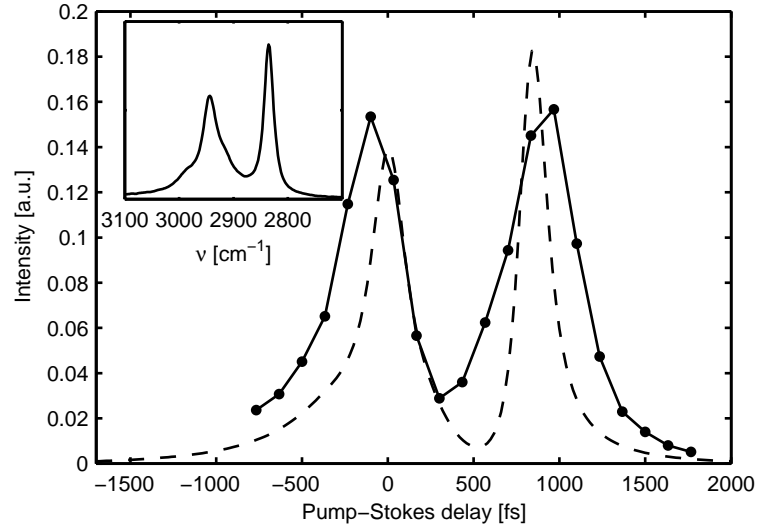
Figure 6.9: Example of measured CARS spectrum with chirped pump and Stokes (solid line and dots) and calculated spectrum with the same parameters (dashed). The inset shows the Raman spectrum.

should provide a CARS spectrum convoluted by some function that depends on the pump and Stokes pulse envelopes.

As an initial guess for the grating separations, formulas from Inchauspe and Martinez (1997) were used, from which the second- third- and fourth order spectral phases can be calculated, if the grating angle, distance, and groove spacing are known.

$$\Phi_2 = -\frac{Z}{c}\frac{\omega_g^2}{\omega^3}\frac{1}{\cos^3\theta}(1+\cos^2\theta). \tag{6.11}$$

θ is the angle of the diffracted beam; Z is the (normal) distance between the gratings; ω is the central angular frequency of the pulse; and $\omega_g = 2\pi c/d$, where d is the groove spacing.

Results

A series of spectra at different Stokes grating separations were acquired. The problem of optimizing the Stokes grating separation is then just a problem of finding the grating separation that gives the narrowest peaks in the CARS spectrum.

The CARS spectrum that is presented in Fig. 6.9 is the best spectrum that we could achieve. The experimental parameters were: Pump

grating separation 80 mm; Stokes grating separation 30.5 mm; pump central wavelength 806 nm; $\Delta\lambda_P = 23$ nm; Stokes central wavelength 1057 nm; $\Delta\lambda_S = 27$ nm; acquisition time 10 s/point. The separation of the peaks in the measured spectrum is consistent with a chirp rate of $0.109\,\mathrm{cm}^{-1}$/s. This corresponds to a second-order spectral phase of $|\Phi_2|$ = 39700 fs^2. A calculation is made using Equations 2.23 and 2.26 (the Matlab script in App. B) with parameters similar to the experimental ones to check if there is consistency. The calculated spectrum is presented in Fig. 6.9. The agreement is not superb, especially the width is off. But it should be noted that the Stokes central wavelength was not stable, it had a tendency to drift slowly. And due to the long acquisition time of 10 s, it was not at all certain that the Stokes wavelength was unchanged from measurement to measurement.

Calculation of Φ_2 imposed by the grating pair (Eq. 6.11) gives $\Phi_2^{(p)}$ = -32000 fs^2 and $\Phi_2^{(S)}$ = -38000 fs^2. This amounts to pulse durations of $\tau_{fwhm,p} = 2.2$ ps (FWHM assuming Gaussian) and $\tau_{fwhm,S} = 1.8$ ps (FWHM assuming Gaussian envelope).

Conclusion

All in all, the proof-of-principle for CARS with a chirped laser pulse and a chirped red-shifted soliton has been demonstrated.

However, there were some major downsides to our experiment. First, excitation power gets significantly reduced by the four incidences on the grating pairs. This is especially a problem for the Stokes pulses, whose power is already limited by fiber parameters. The pump grating (GR50-0608, Thorlabs) has reflection coefficient 0.70 at 800 nm; the Stokes grating (GR50-0610, Thorlabs) has 0.88 at 1050 nm. This leads to maximum overall efficiencies of 0.24 for the pump and 0.60 for the Stokes.

Secondly, as has been discussed previously, the wavelength and the delay of the red-shifted soliton vary with laser power, so they fluctuate a bit pulse to pulse. This smears out the CARS signal vs. delay, and might very well be a contributor to the poor spectral resolution in Fig. 6.9. A third complication is the fact that matching the chirps of the two pulses is quite difficult. No methodology for doing this other than trial-and-error has been devised.

6.8   Discussion and conclusion

Discussion

Clearly, interpretation of CARS spectra, especially in complicated environments like cells, is a non-trivial task because of the nonresonant

background. A detection technique which discriminates against the nonresonant background would be of significant interest for making quantitative analysis less complex. One such solution to completely discriminate against nonresonant background is polarization-sensitive CARS, which is well-known from spectroscopy experiments (Oudar et al., 1979) and has also been demonstrated in CARS microscopy (Cheng et al., 2001). The approach relies on a small difference in the depolarization ratio between the resonant and nonresonant signal, so detection of the CARS signal polarized perpendicularly to the nonresonant signal will yield purely resonant signal. However, this has the disadvantage that the polarizer in front of the detector cuts away a large portion of the resonant signal as well.

A different approach is to detect the CARS signal interferometrically; by mixing the CARS signal with a pre-generated signal at the same frequency, one can eliminate the nonresonant contribution entirely. This will be the topic of Chap. 8.

Conclusion

The setup for single-laser CARS microspectroscopy was described. It relies on a single Ti:sapphire oscillator at 76 MHz. The pump pulse is generated by spectral compression of the laser pulse in a PCF. The Stokes pulse is generated by redshifting the laser pulse in a PCF by the SSFS. An example of a CARS microspectroscopy image of a yeast cell was presented. The impact of the nonlinear chirp of the spectrally compressed pump pulse was investigated experimentally and numerically. The sensitivity limit of CARS microscopy was adressed in a semi-empirical way. It was attempted to deconvolve a CARS spectrum of ethanol in water and to obtain the Raman center frequencies and linewidths. The proof-of-principle of spectral focussing, which can potentially merge CARS microspectroscopy with CARS microscopy was presented. Finally, ways of improving S/N ratio and detection sensitivity were discussed.

Chapter 7

A fiber laser-based light source

7.1 Introduction

As the potential of CARS imaging has unfolded, so have efforts to reduce the complexity, cost, and bulkynesss of the light source. Over time, it is likely that interest in very compact, fiber-coupled, modular light sources for CARS will arise, *i.e.* a light source, that comes in a small box and can be swiftly connected to an input port of a commercial laser-scanning microscope to facilitate immediate CARS imaging. To embark on the route of creating such a light source nessecitates not only a single-laser approach, but equally important, that the laser itself is scaled down dramatically from the bulk Ti:Sapphire laser. This is possible with fiber laser technology, utilising the abundant Yb-based fiber laser technology. Yb-based fiber lasers lie in the same wavelength range, ≈ 1 μm, as the Nd-lasers used for the OPO-based CARS light source in Ganikhanov et al. (2006). This section presents a light source for CARS microspectroscopy capable of delivering simultaneously a near-transform-limited picosecond pulse and a tunable, near-transform-limited femtosecond pulse. The system is kept compact and uncostly through the use of a picosecond fiber laser and a photonic-crystal fiber (PCF) for frequency conversion. We run into the same typical obstacle as in the previous chapter, that with single-laser approaches, a femtosecond pulse is desired to generate a Stokes pulse through nonlinear processes with good efficiency, yet a picosecond pump pulse is desired to attain acceptable spectral resolution.

Section 7.2 describes and characterizes the modelocked fiber laser that was built by us for the purpose; Sec. 7.3 describes how the Stokes pulse is generated and characterizes it; the pump pulse is described

in Sec. 7.4; Sec. 7.5 describes the application of the fiberlaser-based light source to CARS microspectroscopy; Finally, Sec. 7.6 discusses and concludes.

7.2   SESAM-modelocked fiber laser

Setup

The light source in our setup relies on a home-built ytterbium fiber laser mode-locked by a semiconductor saturable-absorber mirror (SESAM). (Herda and Okhotnikov, 2004). The laser operates at 1033.5 nm with a repetition rate of 33.5 MHz. It provides two outputs, "output 1" and "output 2", at average powers of approximately 4 mW (output 1) and 1 mW (output 2).
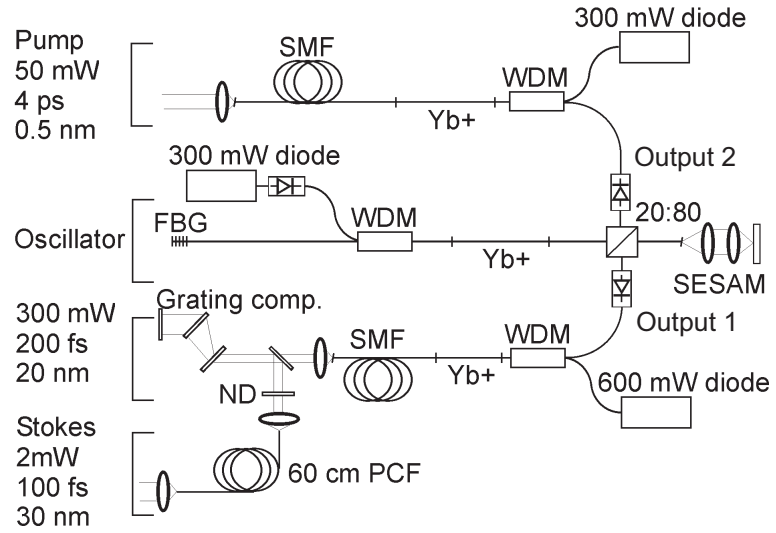

Figure 7.1: Diagram of the light source for CARS microspectroscopy. FBG: Fiber Bragg grating; ND: Variable neutral-density filter; SMF: Single-mode fiber; Yb+: Yb-doped fiber; WDM: Filter wavelength-division multiplexer; PCF: Photonic-crystal fiber; SESAM: Semiconductor saturable-absorber mirror; "20:80": 20:80 polarizing beamsplitter.

A diagram of the laser and the rest of the light source is shown in Fig. 7.1. The oscillator itself consists of a linear cavity made in PM-fibers (mode-field diameter (MFD) = 7 μm). A piece of PM-ytterbium-

doped fiber (MFD 4.8 μm) pumped by a 300 mW laser diode at 976 nm in the cavity functions as the gain medium. A fiber-Bragg grating (FBG) whose reflected spectrum is 0.5 nm-wide and centered at 1033 nm functions as the first cavity end mirror. The grating stabilizes the laser central wavelength and the spectral width. The second cavity mirror is a semiconductor saturable-absorber mirror (SESAM), which modelocks the laser and assures self-starting of the mode-locking. A 20:80 polarizing beamsplitter (PBS) in the cavity functions as the output coupler and provides two outputs from the laser at average powers of approximately 4 mW (output 1) and 1 mW (output 2). The spectral width is 0.5 nm, and the pulse duration immediately after the oscillator is 3 ps, so the pulses are close to the transform-limit. The components spliced onto the oscillator to generate the pump and Stokes pulses will be described in the following sections.
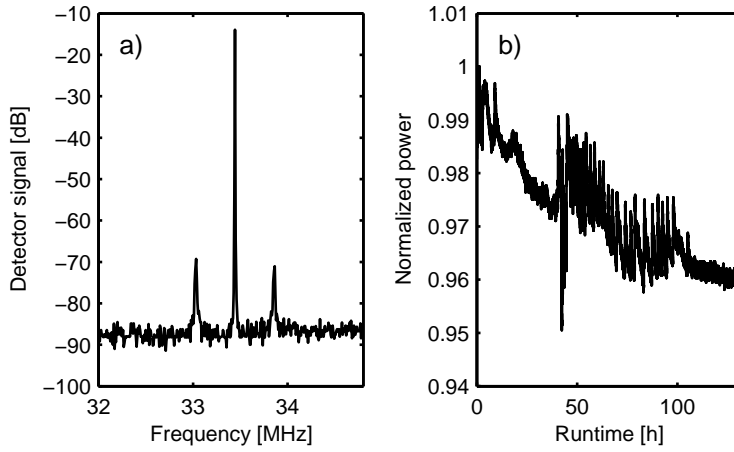
Short-term laser stability

Figure 7.2: (a) RF-spectrum of the fiber laser output; (b) laser output power vs. time, normalized to the initial power.

The short-term power stability of the laser was measured following the approach of von der Linde (1985). In this approach, the intensity autocorrelation function is measured by a two-photon photodiode. The signal is recorded by an RF spectrum analyzer. The RF spectrum then consists of a series of frequency bands, centered at equal multipla of the repetition frequency. Each band consists of a δ-function contribution, which corresponds to the perfect, noise-free pulse train. The second frequency-shifted contribution is the frequency-shifted power spectrum

of the amplitude noise (Fig. 7.2a). The relative root-mean square deviation ΔE of the pulse energy is given as

$$\left(\frac{\Delta E}{E}\right)^2 = \int_{-\infty}^{\infty} P_A(\omega)d\omega, \qquad (7.1)$$

where P_A is the power spectrum of the amplitude noise relative to the total power spectrum. This ratio can be found as the ratio between the area of the main peak and the areas of the side peaks. The areas can be determined somewhat coarsely simply by multiplying their peak value with their widths FWHM (the width at the 3 dB-point). This gives:

$$\left(\frac{\Delta E}{E}\right)^2 = \frac{10^{-6.93} \cdot 0.012\text{MHz}}{10^{-1.39} \cdot 0.001\text{MHz}} = 6.89 \cdot 10^{-5}. \qquad (7.2)$$

Leading to $\Delta E/E = 0.8$ %, which can be interpreted as a measure of the pulse-to-pulse fluctuations.

Long-term laser stability

The long-term stability of the laser is measured simply by measuring the laser power as a function of time with a photodiode over a long period of time. A typical result is shown in Fig. 7.2b. Over the course of 130 hours of continous running, the laser power drops a total of 4 %. This long-term drop in power is in part caused by degradation of the SESAM. It was observed that after several weeks of day-to-day operation, the laser power has steadily dropped even more. The initial power can be restored by moving the SESAM slightly, to focus the laser on a new spot. Apart from this long-term drift, there is some finer structure in Fig. 7.2b, which could maybe be explained as environmental effects.

7.3   Red-shifted Stokes pulse

Output 1 is used to create the Stokes pulse (Bottom part of Fig. 7.1). For the Stokes pulse, we desire a spectrally broad pulse at a longer wavelength than the fundamental laser wavelength. The means of achieving this is as follows. An ytterbium fiber amplifier pumped by a 600 mW laser diode at 974 nm is spliced onto output 1. This amplifies output 1 up to 400 mW after the amplifier. A 5 metre-long piece of standard PM-fiber is spliced onto the amplifier. As the amplified pulse propagates inside this fiber, it undergoes self-phase modulation (SPM) and, after coupling out of the fiber, it has broadened to 15 nm. Average power at this point is 300 mW due to an imperfect splicing. This broadened pulse is then temporally compressed by a pair of transmission gratings (1200 lines/mm) placed in the Littrow configuration, 30

mm apart. The second-order interferometric autocorrelation trace of the temporally compressed pulse, depicted in Fig. 7.3, has a width (FWHM) of 268 fs, which corresponds to a pulse FWHM of 190 fs assuming Gaussian pulse envelope. The time-bandwidth product is 1.06. The imperfect pulse compression is most likely caused by HOD in the 5 m-long SMF. The temporally compressed pulse is sufficiently short
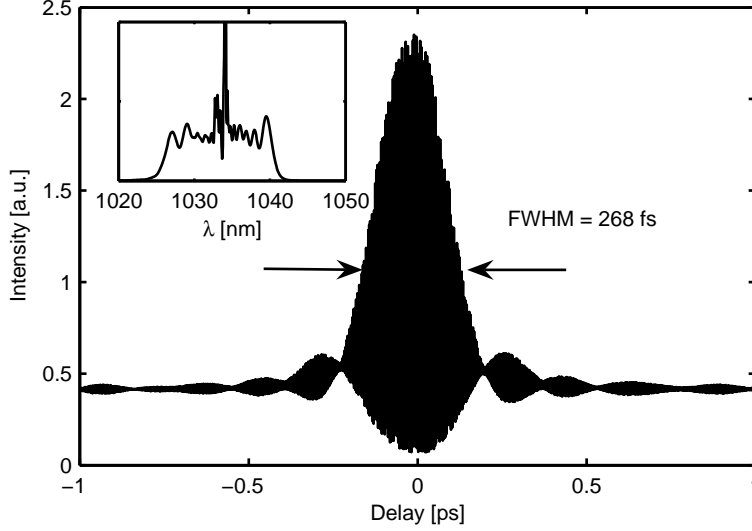

Figure 7.3: Interferometric autocorrellation of output 1 after undergoing SPM and temporal compression. The inset shows the spectrum.

that we can send it through a PCF and generate nonlinear effects, in particular SSFS; we want to create the Stokes pulse along the same lines as we did in Sec. 5.4, redshifting the pulse in a PCF through the SSFS.

The PCF chosen for this application is a 60 cm-long piece of PCF from Crystal Fibre A/S, which has ZDWs at 770 and 1600 nm and a nonlinearity coefficient, γ, of 0.084 $(\text{Wm})^{-1}$. The GVD and group delay of the fiber are shown in Fig. 7.4.

The laser wavelength of 1033.5 nm is thus in the anomalous dispersion regime of the PCF, and the laser pulse in the PCF undergoes SSFS analagous to Sec. 5.4. Although the PCF is not polarization maintaining, we find that the soliton part of the output spectrum is linearly polarized. Example spectra of redshifted solitons is shown in Fig. 7.5. In Fig. 7.6, we show the result of a measurement of the redshifted soliton center wavelength and average power of the soliton
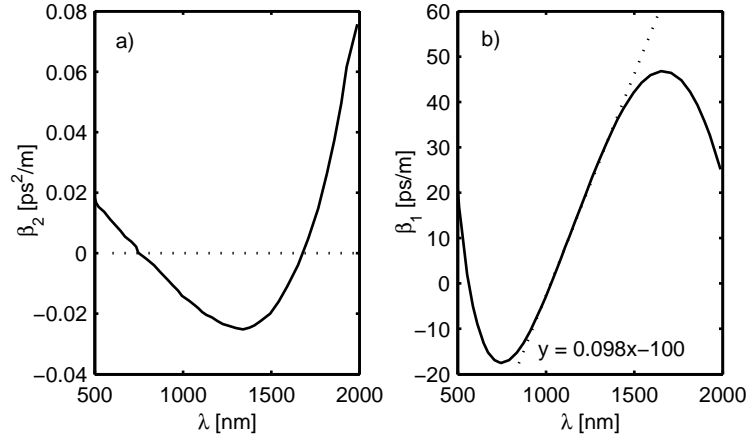
Figure 7.4: (a)GVD vs. wavelength in the PCF; (b) Group delay vs. wavelength, the dashed line is a linear fit to the curve in the 1000 nm -1400 nm region. Data from Schreiber et al. (2005).

itself vs PCF input power. The coupling efficiency in this case was around 12 %. The redshift is almost linear with respect to PCF input power up until 1400 nm. At this wavelength the soliton power is seen to drop. We have noted that these two observations are accompanied by a narrowing of the soliton spectrum. We accredit this to the presence of OH^- in the PCF which absorbs strongly at 1400 nm and perturbs the soliton strongly. In the absence of OH^-, in principle, redshifts up to 1600 nm, the second ZDW should be possible. Another observation is that the formation of multiple solitons sets on, when the fundamental soliton has redshifted to 1300 nm. This is a consequence of the relation $N^2 = (0.321\gamma P_0 \tau_{fwhm}^2)/(|\beta_2|)$; for increased power, the soliton order also increases.

Soliton stability - calculated

The temporal and spectral stability of the redshifted Stokes pulse should be considered. The center wavelength of the redshifted pulses is coupled to the input power (Fig. 7.6) and - because of dispersion in the fiber - so is the delay of the pulses. A fluctuation in laser power therefore manifests itself as a fluctuation in wavelength and delay of the Stokes pulse. From the group delay data of the PCF (Fig. 7.4), a fit to the wavelengths vs. input power data in Fig. 7.6 and the law of propagation of errors, we relate the standard deviation on the soliton center wavelength, $\sigma(\lambda_S)$, and delay, $\sigma(\tau_S)$, to the standard deviation on the
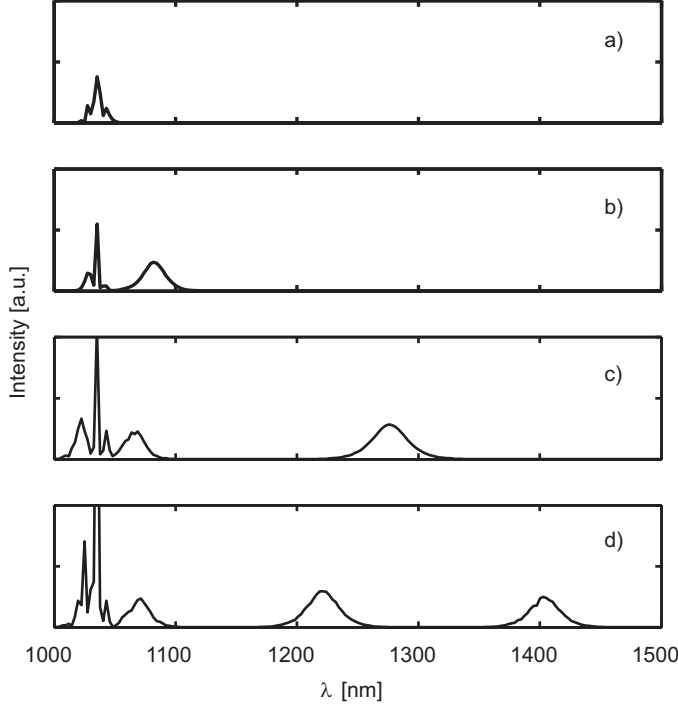
Figure 7.5: Example output spectra of the PCF for increasing input power from a) to d)

intrafiber average laser power, $\sigma(P)$. We find

$$\sigma(\tau_S) \quad = \quad 1.87\frac{[\text{ps}]}{[\text{mW}]}\sigma(P) \qquad\qquad (7.3)$$

$$\sigma(\lambda_S) \quad = \quad 31.8\frac{[\text{nm}]}{[\text{mW}]}\sigma(P). \qquad\qquad (7.4)$$

For typical parameters, $\lambda_S = 1240$ nm and $\sigma(P)/P = 0.01$, these numbers are $\sigma(\tau_S) = 100$ fs and $\sigma(\lambda_S) = 1$ nm. The temporal standard deviation comes close to what can be achieved with inter-locked lasers - in Potma et al. (2002), 21 fs was achieved. From this, we conclude that fast fluctuations are of little importance. There is still some long-term drift in the laser power, though. But this can in principle be compensated for either manually or by a feedback loop that adjusts the PCF input power.
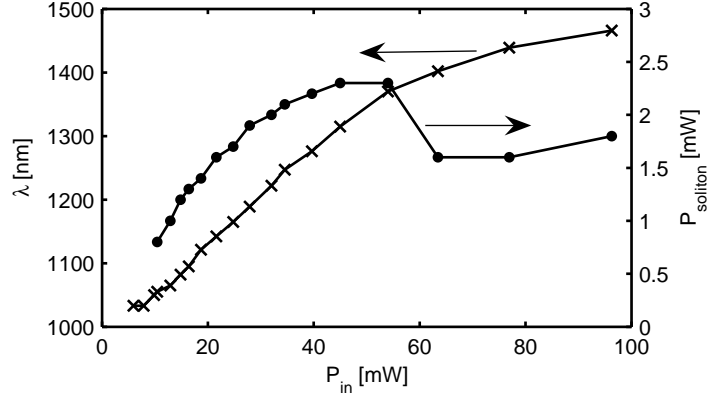
Figure 7.6: Redshifted soliton wavelength (crosses) and power (dots) versus input power.

Soliton stability - measured

In principle, it should be possible to measure the soliton amplitude noise and temporal jitter following von der Linde (1985). This was attempted, but nothing conclusive was observed. It is possible that the soliton mechanism itself serves to stabilize the pulse energy, so that the fluctuations are too small to measure. And that the fluctuations might be on a longer time scale, such that the RF spectrometer has trouble picking them up within a reasonable integration time. The same goes for the temporal fluctuation, which might occur on longer timescales.

7.4   Pump pulse

Output 2 is employed to create the pump pulse for our CARS experiment. The spectral width and duration of output 2 suit our requirements for a pump pulse, so the task at hand is to amplify the pulse to a useful power. To this end, a non-PM ytterbium amplifier pumped by a 300 mW laser diode at 976 nm is employed (top portion of Fig 7.1). The unamplified power of 1 mW makes it possible to achieve amplification to 50 mW average power. A piece of non-PM standard single-mode fiber is spliced onto the amplifier, which serves only as a coarse means of adjusting the interpulse delay between the pump and Stokes pulses. The duration of the pump pulse is measured by second-order interferometric autocorrelation. The autocorrelation trace is shown in Fig. 7.7. FWHM of the trace is determined to be 5.8 ps, corresponding to a

pulse FWHM of 4.1 ps, assuming Gaussian envelope. With a spectral
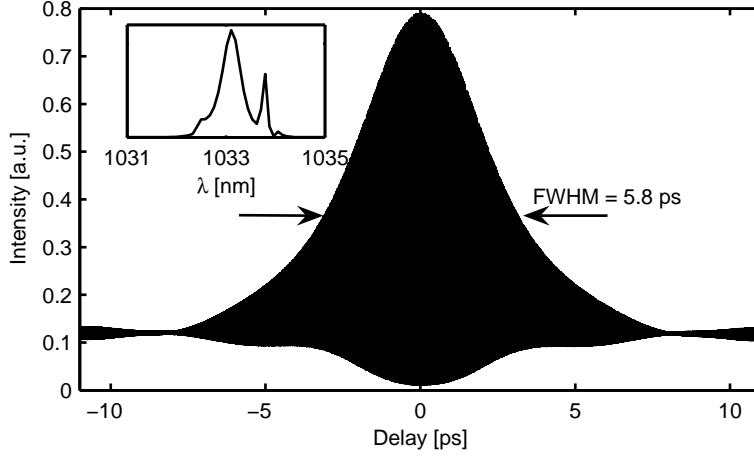FWHM of 0.5 nm, this gives a time-bandwidth product of 0.57.

Figure 7.7: Second-order autocorrelation trace of laser output 2.
The inset shows the spectrum.

7.5   CARS microspectroscopy

The setup for CARS microspectroscopy is depicted in Fig. 7.8.

The CARS field generated in a sample is the sum of a resonant and
a nonresonant part,

$$
\begin{aligned}
E_{aS}(\omega_{aS}) &= (\chi_r^{(3)} + \chi_{nr}^{(3)})E_P^2 E_S(\omega_S) && (7.5)\\
&= \Big(\frac{\chi_r^{(3)}}{\chi_{nr}^{(3)}} + 1\Big)E_{nr}(\omega_{aS}). && (7.6)
\end{aligned}
$$

And the measured CARS intensity is

$$
S_{aS}(\omega_{aS}) = \Big(\frac{|\chi_r^{(3)}|^2}{(\chi_{nr}^{(3)})^2} + 2\frac{\mathrm{Re}[\chi_r^{(3)}]}{\chi_{nr}^{(3)}} + 1\Big)S_{nr}(\omega aS). \qquad (7.7)
$$

By measuring the nonresonant signal, S_{nr}, separately, S_{aS} can be nor-
malized,

$$
\frac{S_{cars} - S_{nr}}{S_{nr}} = \frac{|\chi_r^{(3)}|^2}{(\chi_{nr}^{(3)})^2} + 2\frac{\mathrm{Re}[\chi_r^{(3)}]}{\chi_{nr}^{(3)}}. \qquad (7.8)
$$

And the third-order susceptibility can be modelled as

$$
\chi^{(3)} = \sum_j \frac{A_j}{\nu_j - \nu + i\Gamma_j}. \qquad (7.9)
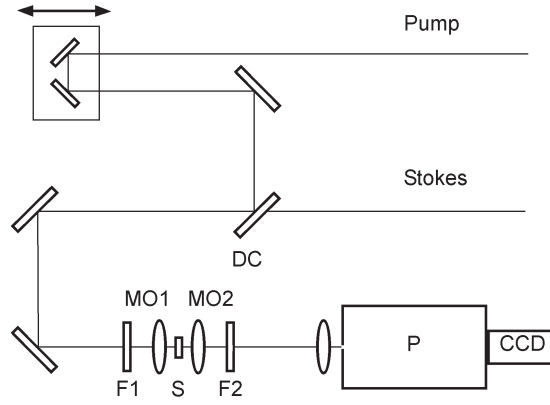$$

Figure 7.8: The setup for CARS microspectroscopy. The pump and Stokes pulses are derived from Fig. 7.1. DC: Dichroic mirror; F: Filter; S: Sample; P: Polychromator; CCD: CCD camera.

The nonresonant susceptibility, $\chi_{nr}^{(3)}$, can be modelled as a real number.

The resolution of the spectrometer was determined with a He-Ne laser to be 0.1 nm or 2.5 cm^{-1}, defined as the FWHM of the He-Ne laser as measured by the spectrometer. As an example of CARS microspectroscopy with the present light source, we acquire a CARS spectrum of benzonitrile. Benzonitrile has a narrow, isolated resonance at 1599 cm^{-1} owing to the ring stretch vibration. The CARS signal from benzonitrile is acquired for 100 s, and the nonresonant signal is subsequently measured as the CARS signal from a glass plate with similar acquisition time. The results of the two measurements are shown in Fig. 7.9a. Figure 7.9b shows the CARS spectrum normalized according to Eq. 7.8. The Raman spectrum of benzonitrile was acquired separately and fitted to Im$[\chi^{(3)}]$ as shown in the inset of Fig. 7.9b. The normalized CARS spectrum was fitted to $a|\chi^{(3)}|^2 + b\text{Re}[\chi^{(3)}]$. A $\chi^{(3)}$ with one resonance was used in both cases. The result of the fit to the Raman spectrum was $\nu_0 = 1599 \pm 2$ cm^{-1} and $\Gamma_0 = 4 \pm 2$ cm^{-1}, and of the fit to the normalized CARS spectrum $\nu_0 = 1592 \pm 3$ cm^{-1} and $\Gamma = 5 \pm 1$ cm^{-1}. The CARS and Raman spectra agree within the uncertainties and the stability of the light source is evidenced by the long acquisition time.
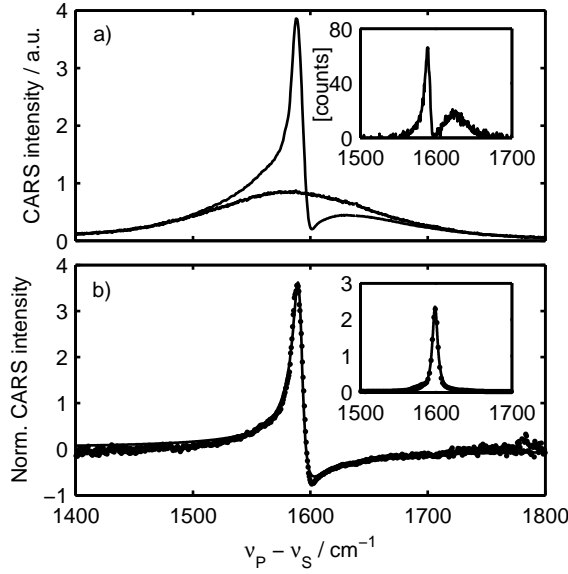
Figure 7.9: CARS microspectroscopy on benzonitrile. a) shows the CARS signal from benzonitrile and the nonresonant background recorded as the CARS signal from a glass plate acquired in 100 s. The inset shows the same spectrum acquired in 1s. b) shows the normalized CARS spectrum along with a fit. The inset shows the Raman spectrum and fit.

7.6 Discussion and conclusion

Discussion

The long acquisition time of 100 s above should be noted. As such, this fiber laser-based light source does not rival Raman spectrometers in terms of speed. Four partial explanations to the long acquisition time can be given. First, our polychromator and CCD are not optimised for the CARS wavelength at 880 nm, the overall efficiency is about 5 %. Second, the pump and Stokes wavelengths employed here (1033 nm-1400 nm) are longer than the ones employed in previous studies (700 nm-1064 nm). It is well known from Raman spectroscopy that signal yield increases with shorter wavelength, the same applies for CARS. Third, due to nonresonant background signal in CARS, normalisation of CARS spectra to the nonresonant signal is required in order to do a meaningful interpretation. For this, a good signal-to-noise level is

nescessary, to obtain that, we have used a long acquisition time. Decent spectra can be obtained quicker as evidenced by the inset in Fig. 7.9. Last, pump and Stokes powers are limited in this study.

For any serious application to be possible, the powers need to be increased. The pump power can relatively easy be scaled up using picosecond fiber amplifiers. In Gomes et al. (2004) amplification of picosecond pulses at 33 MHz-repetition rate up to 700 mW was achieved using a pump-cladding fiber.

The power of the redshifted soliton is governed by the expression $N^2 = (0.321\gamma P_0 \tau_{fwhm}^2)/|\beta_2|$, with $N = 1$ for a fundamental soliton being relevant here. It is seen that to achieve large P_0, the ratio $\gamma/|\beta_2|$ should be small. We have attempted to produce the Stokes pulse in a PCF with larger core (NL-3-850, Crystal Fibre, Denmark) and hence smaller $\gamma = 0.040$ (Wm)$^{-1}$. This yielded approximately a factor of 2 improvement in Stokes power, but the redshift was limited to 1500 cm^{-1} due to our limited laser power. To our knowledge, PCFs are not available with much lower $\gamma/|\beta_2|$-ratios than the ones we have employed. So, development in PCF technology is needed to reach higher Stokes powers. We are aware of a slightly different approach for generating high-power solitons - using hollow-core photonic-bandgap fibers (PBG)s filled with liquid, solitons with peak powers in the megawatt-range can be generated and redshifted (Ouzounov et al., 2003). But in that approach, the redshift is limited by the transmission range of the PBG. Also, the pulse power that is coupled into the PBG should be greater than that required to form a soliton - in this case, the soliton power is higher than what can be achieved with our fiber laser.

A narrower pump spectrum than the one we have employed may be desired for some applications. In that case, pulse amplification combined with spectral compression may prove useful (Limpert et al., 2005).

The Stokes frequency must be extended to permit imaging above 2500 cm^{-1} in the C-H stretch region of the spectrum. The limiting factor for the redshift is the presence of OH$^-$, which absorbs strongly at 1400 nm. This is a technical problem, which is indeed solvable. In newer PCFs, the absorption at 1400 nm is suppressed to a high degree.

A significant improvement of the entire fiber-based source would be to rebuild it in purely PM fibers. Presently, the combination of PM and non-PM fibers as well as mode-mismatch between the Yb-doped fiber and the single-mode fiber leads to significant splicing losses. The less-than-optimal configuration of the present light source is due to the fact, that at the time the splices were done, no splicer with ability to splice PM fibers was available. At the time of writing, a new, all-PM fiberlaser is being built for us by NKT-Research, which should provide higher pump power and greater repetition rate (80 MHz), which should allow for greater Stokes power.

A fairly large concern with this fiber laser-based light source is, that its wavelength range actually negates one of the main advantages of CARS, namely the ability to choose the pump and Stokes wavelengths to lie in the water window of the spectrum, ca. 700 nm-1100 nm (Sec. 3.3, Fig. 3.4). To probe over a 3500 cm^{-1}-wide range, the wavelength regime of our light source is 1033 nm-1600 nm, bound at the low-wavelength limit by the laser center wavelength. This extends well into a spectral range, where especially water starts to absorb strongly. So the light source is clearly not suited for imaging thick samples.

Conclusion

A light source for CARS microspectroscopy based on a home-built fiber laser and a PCF was demonstrated and characterized. Spectral resolution and stability in a CARS microspectroscopy experiment was demonstrated. This light source represents a major reduction of the cost of a light source for CARS microspectroscopy, and it can potentially be made very compact to the point that it will fit onto a small breadboard, providing a mobile light source for CARS microspectroscopy.

Part III

Detection techniques

Chapter 8

Interferometric CARS microscopy

8.1 Introduction

The two major impedements to CARS microscopy is i) the presence of nonresonant background at the anti-Stokes frequency which limits sensitivity and ii) the cross-section for most Raman-active bands is so small that longer signal acquisition times must be used, which makes image acquisition slower. One promising solution to these two problems is to employ interferometric detection of the CARS signal. This chapter starts with introducing the concept of interferometrically-detected CARS microscopy in Sec. 8.2; Sec. 8.3 describes a specialized phase stabilization scheme developed by us for interferometric CARS microscopy; and Sec. 8.4 describes an alternative means of generating a reference pulse devised by us.

8.2 The general idea

Interferometric detection implies mixing the CARS signal with a well-defined, pre-generated signal, a reference pulse, at the same frequency. If the relative phase can be controlled, nonresonant background can be entirely suppressed and signal from (weak) transitions is amplified by making it linear in concentration rather than quadratic.

The underlying principle will be outlined here for picosecond CARS. Picosecond pump and Stokes pulses can be considered quasi-monochromatic, so it suffices to consider each pulse as a δ-function in frequency, and the phase of each pulse can be considered a number rather than a function of frequency. The CARS signal field is then given as

$$E_{aS}e^{i\phi_{aS}} = \chi^{(3)}E_p^2 e^{2i\phi_p}E_S e^{-i\phi_S}, \qquad (8.1)$$

where ϕ_p and ϕ_S are the pump and Stokes phases and E_p E_S and E_{aS} are the (real) pump, Stokes, and CARS fields. The phase of the CARS field is then given as $\phi_{aS} = 2\phi_p - \phi_S$. Mixing the CARS field with a reference field, E_{ref}, with phase ϕ_{ref} on the detector leads to a detected intensity

$$
\begin{aligned}
I &= |E_{aS}e^{i\phi_{aS}} + E_{ref}e^{i\phi_{ref}}|^2 & (8.2) \\
&= E_{aS}^2 + E_{ref}^2 \\
&\quad + E_{aS}E_{ref}(e^{i(\phi_{aS}-\phi_{ref})} + e^{-i(\phi_{aS}-\phi_{ref})}) & (8.3) \\
&= I_{aS} + I_{ref} \\
&\quad + E_p^2 E_S E_{ref}[\mathrm{Re}\chi^{(3)}\cos\Phi + \mathrm{Im}\chi^{(3)}\sin\Phi], & (8.4)
\end{aligned}
$$

where Φ is the relative CARS-reference phase, $\Phi = \phi_{aS} - \phi_{ref}$. Now, examining the last equation, we see first of all, that only the interferometric terms depend on Φ. Hence, by applying a small sinusoidal phase modulation to the reference field, $\sin(\Omega t)$, $\Phi \rightarrow \Phi + \sin(\Omega t)$, the non-interferometric terms can be suppressed by lockin-detection, leaving only the interferometric ones. Secondly, when $\Phi = \pi/2 + p\pi$, the cos-term in Eq. 8.4 vanishes, and similarly, when $\Phi = p\pi$, the sin-term vanishes. Bearing in mind that the nonresonant susceptibility is a real number, the former case corresponds to complete supresion of the nonresonant background. Thirdly, the interferometric terms display linear dependence upon $\chi^{(3)}$, resulting in greater signal from dilute (weak) scatterers compared to that from concentrated (strong) scatterers.

In order to achieve consistency in interferometric CARS measurements, Φ has to be controlled to an accuracy on the order of few degrees, this corresponds to an accuracy in the optical path lengths difference between CARS and reference field of few nm. For this purpose, a Mach-Zender type interferometer might be employed, like the one in Potma et al. (2006). But without some kind of active stabilization scheme, the interferometer will be prone to drift due to thermal, acoustic, and air convection effects. Furthermore, known stabilization schemes often employ phase modulation, rendering them unsuitable for interferometric CARS, because another phase modulation is already in the setup. The development of a stabilization scheme without phase modulation and absolute phase control will be the topic of Sec. 8.3.

The generation of the reference pulse is an important issue. It seems the easiest to generate it by four-wave mixing (FWM) of the pump and Stokes pulses, since CARS itself is a FWM process. In Potma et al. (2006), a nonresonant CARS medium was employed to this end. This is a quite inefficient process, and it would be interesting to investigate an alternative medium for the generation of the reference pulse that

displays higher efficiency, while retaining tunability. This is the topic of Sec. 8.4, where FWM in a PCF is investigated.

Interferometric detection has previously been used in CARS spectroscopy (Hahn and Lee, 1995). Interferometric detection has also been demonstrated in multiplex CARS (Evans et al., 2004; Kee et al., 2006) as have other miscellaneous broadband approaches to CARS (Gershgoren et al., 2003; Greve et al., 2005; Jones et al., 2006; Lim et al., 2006, 2005; Marks et al., 2004; Marks and Boppart, 2004; Ogilvie et al., 2006). The strength of these broadband approaches (microspectroscopy) lie in their ability to acquire spectra rapidly, unlike the narrowband approach used in this chapter (microscopy), which facitilates rapid image acquisition.

8.3 Interferometer stabilization

Introduction

Previously reported interferometer stabilization techniques rely on generating an error signal based on the intensity output of the interferometer. This error signal is in turn processed and fed back to a phase-adjusting element in the interferometer. Gray et al. (1999) developed an active stabilization scheme which employs two detectors to detect the intensity at the output ports of a Michelson interferometer. The difference between these two signals, being proportional to the cosine of the phase difference, was used as an error signal to lock the interferometer at a position close to the center of a particular fringe. A similar technique has also been reported by Jensen et al. (2001). However, this DC-coupled balanced stabilization technique does not permit efficient adjustable phase control. The most commonly used active stabilization technique to achieve phase control is based on applying a phase modulation at a frequency Ω to one of the interfering beams and subsequently detecting the output signals using lock-in techniques at frequencies Ω and 2Ω. By doubling the Ω signal and adding it to the $\pi/2$ -phase-shifted 2Ω signal, an error voltage proportional to the sine of the phase difference between the two beams is generated (Freschi and Frejlich, 1995). Using this technique, Freschi and Frejlich were able to stabilize an interferometer at different phase settings with a precision better than one degree (Freschi and Frejlich, 1995; Barbosa et al., 2002; Iwai et al., 2004).

In either of the above described techniques, the error signal is nonlinear, being proportional to the (co)sine of the phase difference between the interfering beams rather than the phase difference itself. Hence, if the phase difference between the beams jumps beyond $\pm\pi$ radians (due to, say, acoustic noise or external perturbations), the interfer-

ometer gets locked to a neighboring fixed point which is displaced by 2π radians. This is not desirable in applications like interferometric CARS microscopy where multiple wavelengths are being guided through the interferometer and where the absolute phase difference needs to be maintained at a fixed value, *i.e.* Φ will generally be to different multiples of π because there are three different wavelengths involved in the setup.

It is critical that the phase difference between the arms of the interferometer, Φ, can be set to arbitrary values. This is because the Φ as determined by the interferometer will generally not be constant when the pulses propagate. Rather, dispersion in optical elements means that Φ in the sample plane will be offset from Φ by a constant value which, of course, generally is $\neq p2\pi$. There is a very simple way to do away with this problem without designing a new stabilization scheme, and rather use an existing one with nonlinear error signal. If the the stabilization scheme can just lock Φ at a particular value, an offset can be added by using a tunable dispersive element such as a pair of wedge prisms. This approach, however, does not do away with the risk that the interferometer may get locked to $\Phi \pm p\pi$, therefore the development of a new stabilization scheme is still justified.

Experimental setup: Collinear and non-collinear geometry

Figure 8.1 shows a sketch of the experimental setup. A He-Ne laser operating at 632.8 nm is used as a reference (r) source to stabilize the interferometer. A 822 nm laser beam (p-beam) from a tunable intra-cavity doubled optical parametric oscillator (OPO, Levante, APE Berlin: pulse width = 5 ps, and repetition rate = 76 MHz) is chosen as the primary light source; the aim is to stabilize the interference signal from this light source. The beam splitter BS1 splits the beams (r into r1, r2, and p into p1, p2) into the two arms of the interferometer. In the first arm, both the beamlets (r1 and p1) co-propagate and are individually detected at the two output ports after the beam splitter BS2 using a pair of interference filters (F). A mirror mounted on a piezo stack (Model: AE0505D08, Thorlabs Inc.) is used to actively stabilize the interferometer. The second arm of the interferometer is similar to that of the first one except for a wedge prism (WP) placed in the beam path to spatially disperse r2 and p2. The orientation of WP is adjusted so as to allow collinear propagation of p1 and p2 after BS2 (see the inset in Fig. 1); the resulting interference intensity is detected using a photo-diode PD3. At the second output port of the interferometer, the r2-beamlet is reflected at BS2 and exits at angle with respect to to r1 (see the inset in Fig. 8.1). Due to this non-collinear
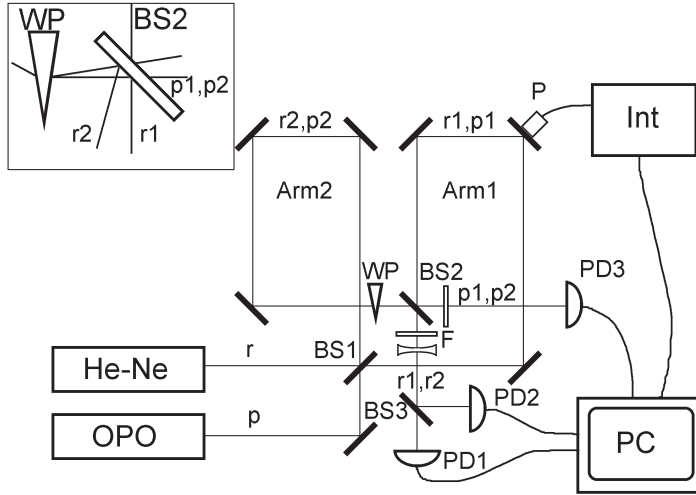
Figure 8.1: Schematic of the stabilized interferometer. He-Ne: Helium-neon reference (r) laser; OPO: Optical parametric oscillator delivering the (p)-beam; BS: Beam splitter; F: Filter; PD: Photo diode; WP: Wedge prism; PC: Personal computer; Int: Integrator circuit; P: Piezo transducer. The angles shown in the inset are exaggarated. Suffixes 1 and 2 denote beamlets that travel through arm 1 and 2, respectively.

geometry of propagation of the reference beamlets, straight line fringes are observed beyond the diverging lens (L). Two distinct points on the fringe pattern that are displaced from each other by one-fourth of the fringe spacing are detected by the photodiodes PD1 and PD2. Note that the reference laser in this scheme has to be of different wavelength than that of the primary light source. Note also that using the wedge prism to misallign the r-beam is only possible for narrowband pulses (picoseconds or longer). The voltage values generated by the photodiodes PD1, PD2 and PD3 are sampled at 5 kHz using a National Instruments data acquisition board (Model: PCI 6221) and the signals are stored in a computer (PC) for further processing.

Stabilization scheme

The first step in the calibration process involves positioning the photodiodes PD1 and PD2 so that the signals detected by them correspond to relative phases at each detector that are different by $\pi/2$. This is done by applying a voltage ramp to the piezo and simultaneously translating

one of the photo-diodes laterally until the plot of PD1 signal versus PD2 signal is an ellipse whose minor or major axis is horizontal. In the second step, the PD1 and PD2 signals are normalized to maximum amplitudes of ± 1. This is done by applying a (linear) voltage ramp to the piezo, the time varying sinusoidal oscillations of PD1 and PD2 signals are analyzed to determine their amplitudes (A1 and A2) and their offset levels (O1 and O2). Subsequently, the signals are normalized to oscillate between ± 1 by subtracting their corresponding offset levels and dividing by their corresponding amplitudes. In the experiment, this calibration process is performed using a home-written C++ program which continually applies a voltage ramp to the piezo, monitors the photo-diode signals and determines the offset values and the amplitudes of oscillations in real-time through an iterative procedure. Provided the photodiodes are in the right positions, this process of calibration is done under two seconds. The calculated offset and amplitude values are used for phase determination.

The phase difference, $\Delta\phi$, between the two interfering beamlets r1 and r2 is determined from the signals at PD1 and PD2 using the following formula:

$$\Delta\phi = \arctan\left(\frac{V_1 - O_1}{V_2 - O_2} \times \frac{A_2}{A_1}\right), \tag{8.5}$$

where V_1 and V_2 are the detected voltages. A phase unwrapping algorithm is also applied on the calculated phase difference so that the phase difference determined by the software corresponds to the optical path change in the interferometer. Note that a phase unwrapping algorithm alone with a sinusoidal error signal would not allow for absolute phase control, because the sine (and cosine) function is not injective over a range of 2π. The tangent on the other hand is. If the desired phase difference is $\Delta\phi_d$, then the error signal, V_{err}, is set to

$$V_{err} = g(\Delta\phi - \Delta\phi_d), \tag{8.6}$$

where g is a constant gain factor; larger values of g lead to faster reaction times of the interferometer. The error signal given in Eq. 8.6 forms the input to a simple operational-amplifier-based integral feedback circuit (Horowitz and Hill, 1989) which in turn generates a compensation signal for driving the piezo.

Results

Using a C++-based GUI software, we can change the gain factor g, set the desired phase difference $\Delta\phi_d$ to an arbitrary value, and perform adjustable phase control. In the following subsections we present some

of the experimental results which highlight the speed and robustness of
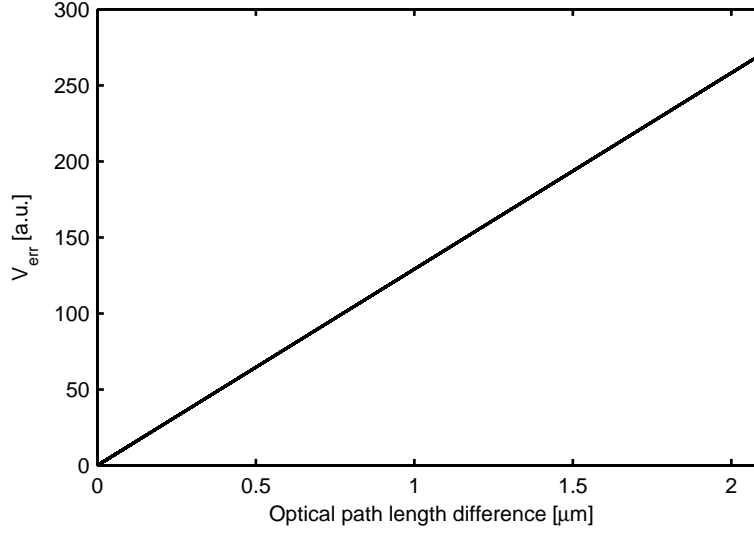this stabilization scheme.

Figure 8.2: The recorded linear dependence of the error signal
V_{err} upon optical path length difference. From Krishnamachari
et al. (2006).

As mentioned in the previous sections, the strength of the current
stabilization scheme is the generation of a linear error signal. To verify
the linearity of the error signal, the optical path difference was changed
by applying a triangular waveform to the piezo. The generated error
signal is plotted with respect to the variation in the optical path length
in Fig. 8.2. As is evident from the figure the linear relationship between
the two quantities is valid for more than 2 μm (which is $> 6\pi$ radians
at 632.8 nm) path length variation.

Fig. 8.3 shows the free-running output of the interferometer. The
output intensities drift due to variations in the optical path difference
between the two arms. To actively stabilize the interferometer, the
integrator output was fed to the piezo with $\Delta\phi_d$ set to zero radians.
Figure 8.4 shows the long term stability of the interferometer. The
freely drifting photodiode outputs settle within 20 ms. Note that the
PD1 and PD2 outputs are $\pi/2$ out-of-phase as required. Figure 8.5
shows the normalized spectra of the OPO interference signal in the ab-
sence and in the presence of the stabilization. In the free-running mode
of the OPO, the output intensity, apart from a slow drift, is influenced
by the acoustic noise of the chillers and the pumps used for cooling the
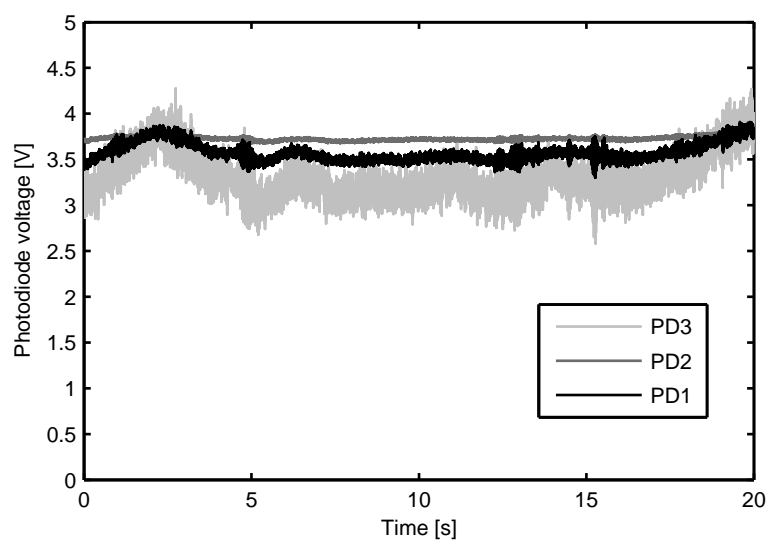
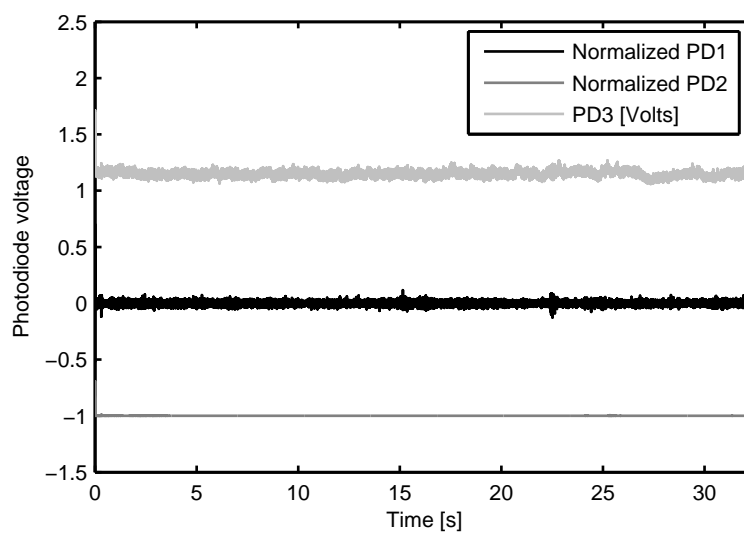Figure 8.3: Unstabilized output of the three photodiodes.

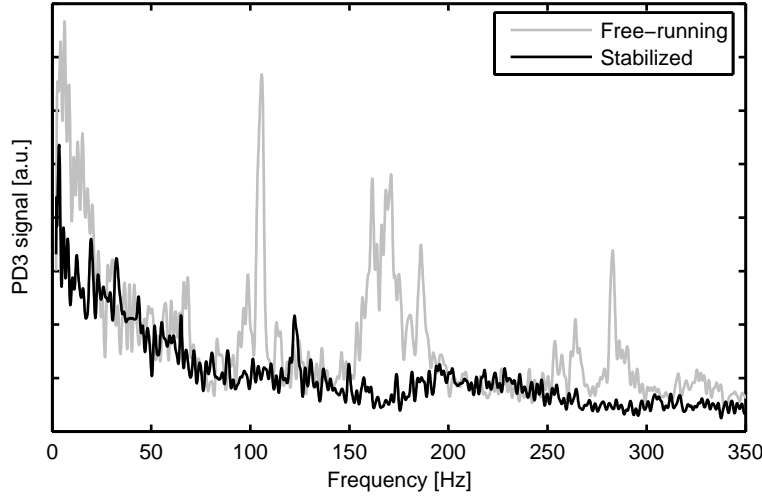Figure 8.4: Stabilized outputs of the three photodiodes.

Figure 8.5: Fourier spectra of the OPO interference output measured at PD3 with and without stabilization.

laser sources in the laboratory. However, these acoustic disturbances are suppressed when the stabilization mechanism is switched on as is evident from Fig. 4. The estimated mean standard deviation of the noise in the stabilized OPO signal corresponds to an optical path variation of $\approx$ 6.5 nm. We note that this limitation is not imposed by the stabilization scheme but rather by the structured acoustic noise spectrum in the laboratory. Another important aspect of any stabilization scheme is the speed with which the states of stabilization can be switched. We determined the optimum response time, *i.e.* the fastest response time for which there was no "overshoot" when changing $\Delta\phi_d$ within π radians, to be 20 ms by adjusting the gain g.

Figure 8.6 demonstrates the real-time phase adjustable feature of the stabilization scheme. Every 2 s the desired phase difference value was increased by 0.2 π radians (at 632.8 nm) with a total phase variation of 5π radians in 50 s. Due to the linear dependence of the error signal, the interferometer can be promptly locked at arbitrary phase values even for phase settings beyond π radians. Figure 8.7 shows the interference output of OPO when the desired phase, $\Delta\phi_d$ is instantly switched at $t = 4$ s from zero radians to π, 2π, 3π, and 4π radians (at 632.8 nm). As is evident, even for phase changes as large as 4π radians, the interferometer gets readily locked. This is possible because the stabilization mechanism is based on a linear error signal proportional to
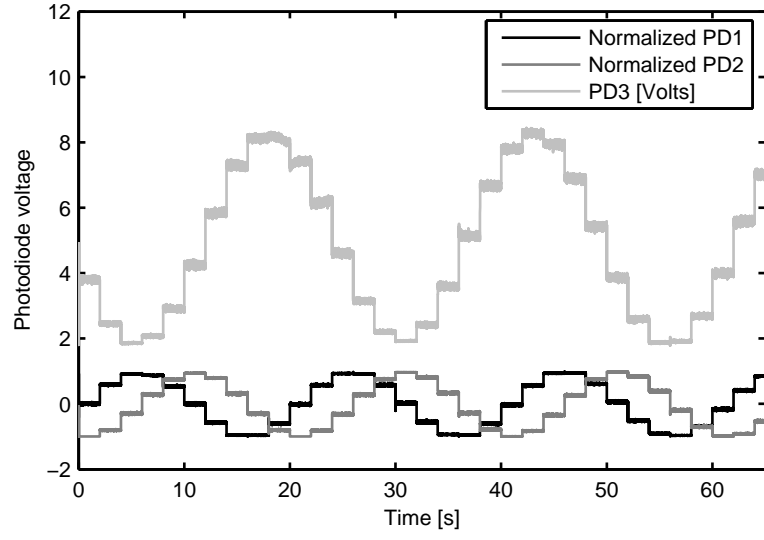
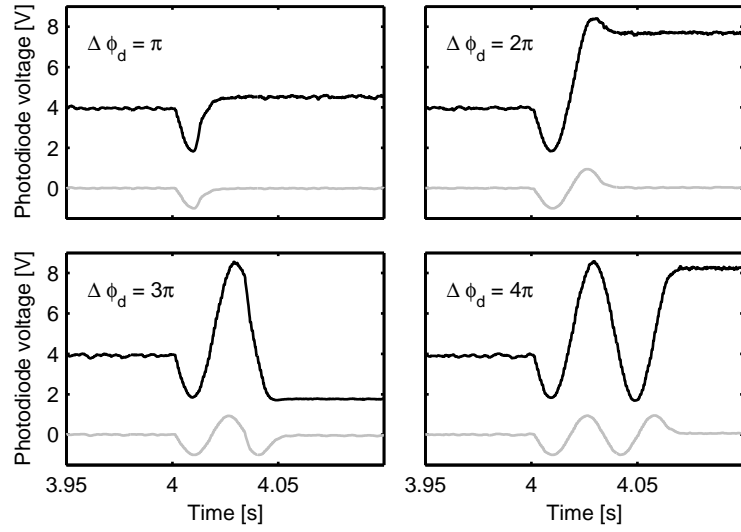Figure 8.6: Demonstration of absolute phase control. Photodiode voltages when $\Delta\phi_d$ is stepped in 0.2π steps.

Figure 8.7: Photodiode voltages for instantaneous changes of ϕ_d. Black line: PD3 (Volts); Grey line: Normalized PD1.

the optical path difference in the interferometer. For comparison, the normalized output at PD1 is also shown, which is 0 before and after each π phase jump. This agrees well with the fact that the normalization is such that the normalized PD1 voltage is a sine function of $\Delta\phi - \Delta\phi_d$. The above results establish the robustness of the stabilization scheme.

The idea of linear error signal generation and the technique for driving the interferometer in collinear and non-collinear geometries simultaneously are general and hence can be used for the stabilization of any interferometric configuration.

Conclusion

This stabilization scheme is simple and robust. The error signal is linear with respect to the changes in the optical path length of the interferometer. It allows for locking the interferometer at arbitrary path differences ranging from a few nanometers to at least 2 μm with switching times down to 20 ms. The shortcoming is that an algorithm must be run on a PC to calculate the arctangent and do the phase unwrapping. The acquisition board was hardware triggered, but increasing sampling frequency by increasing the trigger frequency only works as long as the algorithm executed in each sampling time interval is fast enough. It was found that the software was only fast enough to allow sampling frequencies of $\approx$ 7000 Hz, hence our choice of 5000 Hz. Still, the scheme does eliminate the most pressing problem of interferometric CARS, namely slow phase drift. Fast oscillations in the phase typically arise from knocking on the optical table or the like, but due to the resonance frequencies involved, these fast oscillations die out very rapidly.

The concept of controlling the absolute relative phase of two collinear interfering beams with the help of a reference beam in non-collinear geometry without the need for phase-modulation could have applications not only in CARS microscopy. Precision interferometric lithography might be one such field, where phase-modulation is unwanted. In phase-shifting interferometry, it is nessecary to be able to adjust the phase difference between collinear beams from the two arms in an interferometer to an arbitrary value.

Stabilization for interferometric CARS

In the examples above, it was only shown, how the phase between the two parts of a single split beam can be controlled. This was only for demonstrative purposes. The construction of the interferometer was motivated by the prospect of controlling the phase Φ (Eq. 8.4) in interferometric CARS microscopy, which is a 3-colour experiment. For
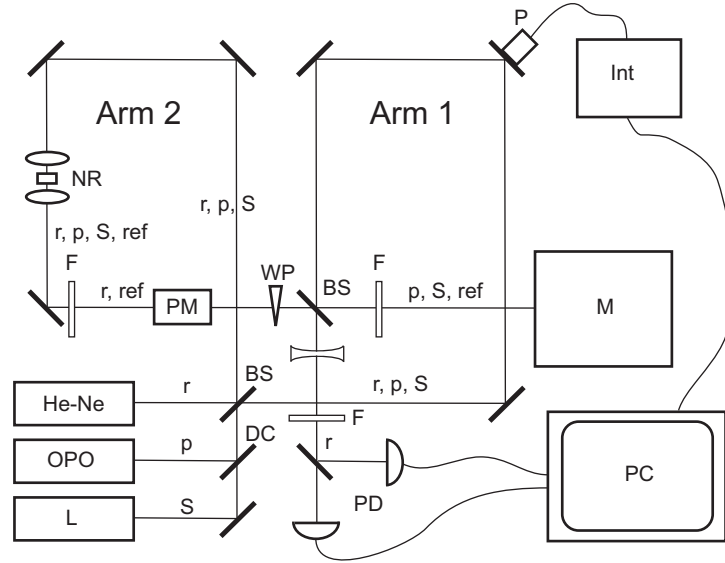
Figure 8.8: Proposed schematic of CARS microscopy employing the stabilization scheme of Sec. 8.3. He-Ne: Helium-neon reference (r) laser; OPO: Optical parametric oscillator delivering the pump-pulse (p); L: Laser delivering the Stokes pulse (S); NR: Nonresonant medium in which the anti-Stokes reference (ref) is generated; BS: Beam splitter; DC: Dichroic mirror; F: Filter; PD: Photo diode; WP: Wedge prism; PC: Personal computer; Int: Integrator circuit; P: Piezo transducer; PM: Phase modulator; M: Microscope.

the adaption of the the interferometer to interferometric CARS, a few changes need to be made from Fig. 8.1. For use in interferometric CARS, the interferometer would look like Fig. 8.8

   Pump and Stokes pulses propagate in arm 1, the reference anti-Stokes in arm 2. A nonresonant sample is now added to Arm 2, in which the reference signal at the anti-Stokes frequency is generated. A phase modulator is also added to arm 2 to modulate ϕ_{ref} and hence Φ to facilitate lockin-detection of the interferometric anti-Stokes signal in the microscope.

8.4 PCF-generated reference pulse

Introduction

The study of nonlinear optics in fibers has focussed mainly on the generation of wide supercontinua. Less emphasis has been put on narrow-band frequency conversion of picosecond pulses. The development of efficient PCF-based conversion schemes for the generation of spectrally tunable, picosecond pulses would be of considerable interest for picosecond CARS spectroscopy.

FWM (Sec. 2.5) in optical fibers is a promising mechanism for frequency conversion of ps-pulses. In standard fibers, anti-Stokes generation has been used to parametrically shift the frequency around the telecommunication wavelength.(Agrawal, 1995; Marhic et al., 1996) FWM in PCFs (Sharping et al., 2001) can exhibit much larger anti-Stokes shifts than in standard fibers (Husakou and Herrmann, 2002; Wabnitz, 2006; Andersen et al., 2004). Using PCFs, anti-Stokes shifts over several tens of nanometers was demonstrated around 1550 nm (Wabnitz, 2006; Kwok et al., 2005; Zhang and Demolan, 2005) and several hundred nm around 800 nm. (Andersen et al., 2004).

This earlier work has mainly focussed on pulses that are too long to be of interest in CARS spectroscopy. In this section we show that anti-Stokes shifts of several hundred nm are exhibited in a short PCFs for ~ 10 ps pulses. It is emphasized that the anti-Stokes generation takes place without competing nonlinear effects or temporal broadening. We demonstrate that the coherence between the generated anti-Stokes pulse and the pump and Stokes pulses is retained after the fiber by applying it to interferometric CARS microscopy (Sec 8.2).

In previous picosecond interferometric CARS studies, the local oscillator was generated with low efficiency in a nonresonant liquid sample. (Potma et al., 2006) In addition, phase drift in the interferometer may compromise the accuracy of the technique unless an active stabilization scheme is being used, like the one in Sec. 8.3. A simple and stable CARS interferometer can be constructed by employing the efficiently generated anti-Stokes radiation in the PCF as the local oscillator, taking advantage of favourable phase-matching conditions in the PCF.

FWM in PCFs

We study the case where picosecond pump and Stokes pulses are co-propagating in the PCF. Referring to Sec. 2.5, the generation of signal at the anti-Stokes frequency, $\omega_{as} = 2\omega_p - \omega_S$, is governed by the wave-vector mismatch, $\Delta\beta$. In the limiting case of no pump depletion and at low pump power (so the nonlinear phase can be ignored), the reference

signal power can be written as (Agrawal, 1995)

$$P_{aS} = G_a P_S, \tag{8.7}$$

where G_a is the single-pass gain, from Eq. 2.48, it is obtained that

$$G_a = P_{aS}(L)/P_S(0) = (\gamma P_p)^2 \frac{\sin^2(\Delta\beta L/2)}{(\Delta\beta/2)^2}. \tag{8.8}$$

P_p and P_S are the pump and Stokes peak powers and L the fiber length. If a short length of PCF is used, that leads to a broad range of $\Delta\beta$ or, equivalently, frequencies, for which phase-matched FWM can occur. If the GVD, $\beta_2(\omega)$, of the PCF is known, we can obtain the wavelength dependence of β_1 and β_0 by integration.

$$\beta_1(\omega) = \beta_1(\omega_0) + \int_{\omega_0}^{\omega} \beta_2(\omega')d\omega' \tag{8.9}$$

$$\beta_0(\omega) = \beta_0(\omega_0) + \int_{\omega_0}^{\omega} \beta_1(\omega')d\omega' \tag{8.10}$$

In practice, this is done by first fitting a high-order polynomium to the known β_2-curve,

$$\beta_2 = \sum_{n=0}^{9} a_n(\omega - \omega_0)^n. \tag{8.11}$$

The integration of β_2 can then be done analytically,

$$\beta_1(\omega) = \sum_{n=0}^{9} \frac{1}{(n+1)} a_n(\omega - \omega_0)^{n+1} \tag{8.12}$$

$$\beta_0(\omega) = \sum_{n=0}^{9} \frac{1}{(n+1)} \frac{1}{(n+2)} a_n(\omega - \omega_0)^{n+2} \tag{8.13}$$

Note that the above expressions for β_1 and β_0 are not the absolute values. Absolute determination is not possible, with prior knowledge only of β_2. Rather, the values are relative values to $\beta_1(\omega_0)$ and $\beta_0(\omega_0)$. But this fact is irrelevant in the present context. In determining $\Delta\beta$, the zero'th and first orders cancel out. Once $\beta_0(\omega)$ is known, it can be established, for which combinations of pump, Stokes and anti-Stokes wavelengths the phase-matching criterion is fulfilled. In practice, this is done by a home-written C++ program, that calculates $\Delta\beta$ for different combinations of ω_p and ω_S.

We use a 16 mm-long piece of single-mode polarization-maintaining PCF (Crystal Fibre A/S, Denmark) with zero-dispersion wavelengths (ZDW)s at 780 nm and 1100 nm. This fiber has a nonlinear coefficient
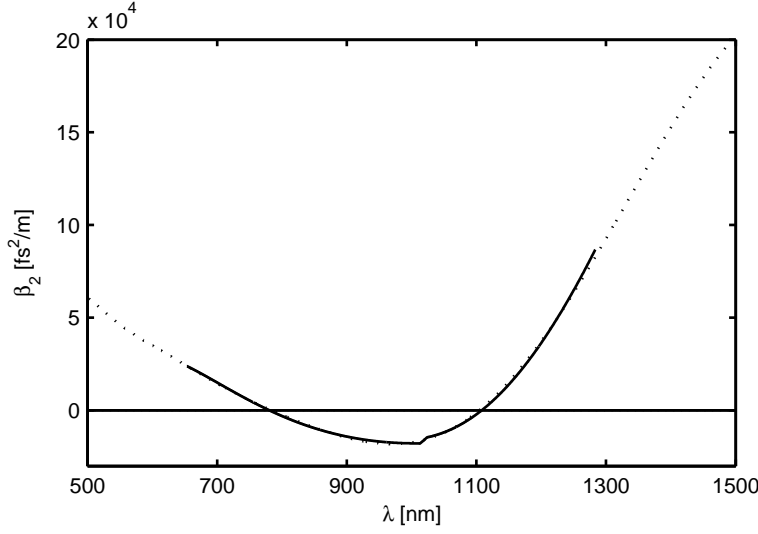
Figure 8.9: Measured dispersion curve of the PCF (solid) and extrapolated fit of Eq. 8.11 thereto (dashed). Measured data are from Crystal Fibre A/S.

a_0	-9454	fs^2/m
a_1	-1.167e5	fs^3/m
a_2	4.833e5	fs^4/m
a_3	-5.96e5	fs^5/m
a_4	5714	fs^6/m
a_5	8.654e5	fs^7/m
a_6	-1.064e6	fs^8/m
a_7	5.975e5	fs^9/m
a_8	-1.655e5	fs^{10}/m
a_9	1.824e4	fs^{11}/m

Table 8.1: Coefficients in the expansion $\beta_2 = \sum_{n=0}^{11} a_n(\omega - \omega_0)^n$ with $\omega_0 = 1.77$ corresponding to 1064 nm.

$\gamma = 0.095 \ (\text{Wm})^{-1}$ and the core diameter is 1.7 μm. The dispersion curve and the fit of Eq. 8.11 is shown in Fig. 8.9. The measured data were appended manually prior to computing the fit. The coefficients thus obtained are listed in table 8.1. The phase-matching curve for FWM in this fiber is shown in Fig. 8.10. Figure 8.11 shows the single-pass gain as a function of pump wavelength and Stokes wavelength, respectively. In the present case, we use the less-than-optimal approach
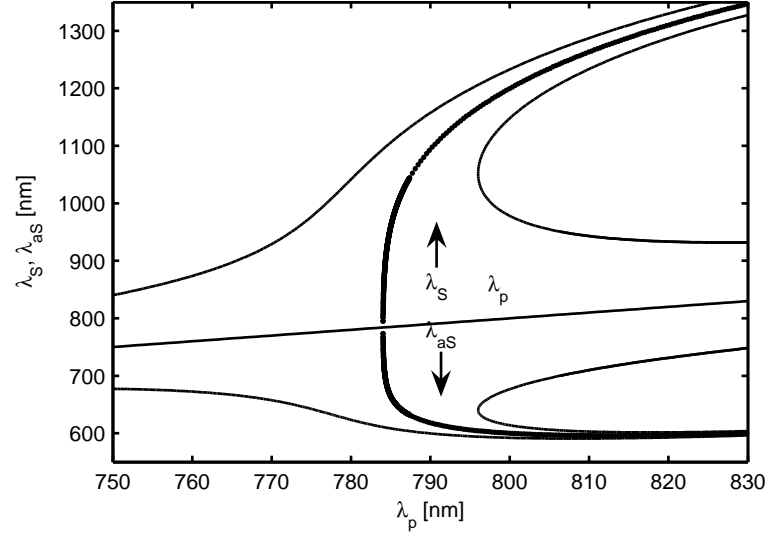
Figure 8.10: Phase-matching for FWM in the PCF. The thick line corresponds to $\Delta\beta = 0$, the thin line to $|\Delta\beta L/2| = \pi/2$.

of keeping the Stokes wavelength fixed while varying the pump wavelength. It would be more optimal to keep the pump wavelength fixed near the ZDW, because this gives the broadest gain curve.

If dispersion and nonlinear effects besides FWM are to be neglegted as in this case, the PCF should be sufficiently short. Spectral broadening of the pulses is expected to occur for a nonlinear interaction length $L_{nl} = 1/(\gamma P)$ of $\sim$100 mm. The dispersion length, $L_D = \tau_0^2/|\beta_2| \sim 10^4$m for all pulses, shows that chirp effects are negligible. The efficiency of FWM increases with PCF length. The group delay walkoff, $L(\beta_1(\lambda_1) - \beta_1(\lambda_2))$, is what ultimately sets the limit for the efficiency. And it is also, what defines the applicability of the generated anti-Stokes pulse as reference pulse in interferometric CARS microscopy; if the reference pulse is significantly delayed with respect to the pump and Stokes pulses, that will result in poor overlap between the reference pulse and the CARS signal, reducing the interference between the two. The group delay, $\beta_1(\omega)$ of the PCF is plotted in Fig. 8.12. From $\beta_1(\omega)$, the relative delays between the involved pulses can be found, which is shown in Fig. 8.13. The criterion, which the PCF length should fulfill is that the resulting interpulse delays are much smaller than the pulse durations. This is clearly fulfilled for the present 16 mm-length of the PCF, for which the largest of the involved relative delays is $\tau_{aS} - \tau_p \approx$ 200 fs.
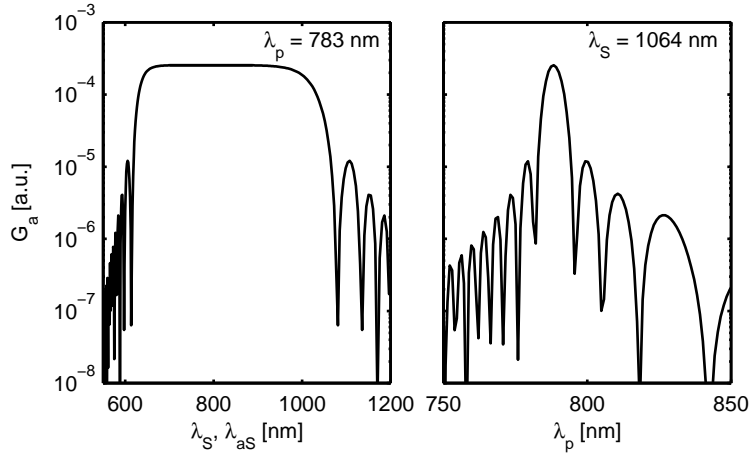
Figure 8.11: Examples of single-pass gains for (left) fixed pump wavelength and (right) fixed Stokes wavelength. Both are calculated in the limit of no pump depletion.
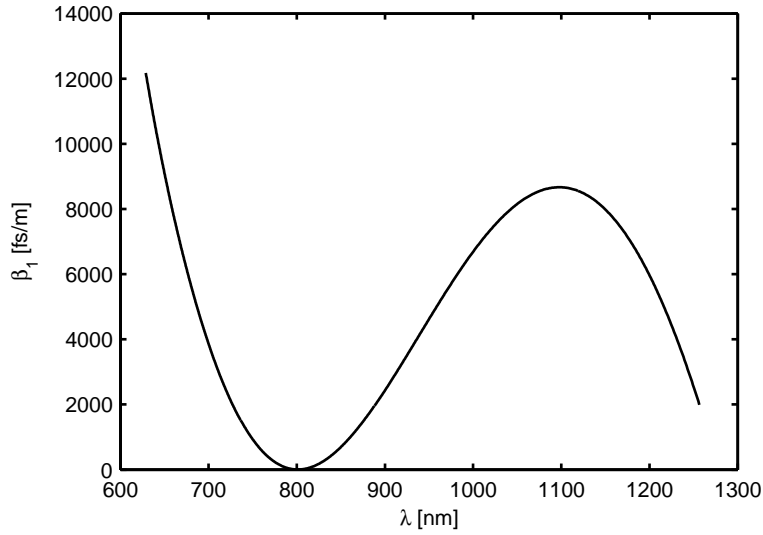

Figure 8.12: β_1 of the PCF. Numbers are relative to the value of β_1 at the ZDW.

Results

The Stokes beam is derived from a 76 MHz, 7-ps modelocked Nd:Vandate laser at 1064 nm. A ps-synchronously pumped optical parametric os-
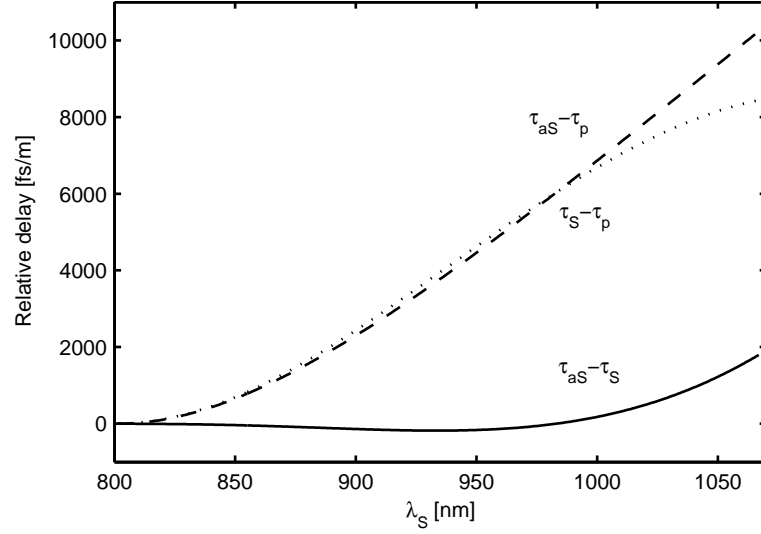
Figure 8.13: Relative delays of the Stokes (S), anti-Stokes (aS) and pump (p) pulses taking part in a FWM process in the PCF.

cillator provides the tunable pump beam (775 - 820 nm) for the CARS process. Both the pump and Stokes are coupled into the PCF with a microscope objective. Using 40 mW at 816.3 nm and 60 mW Stokes power at 1064 nm in the fiber, we typically generate 1 μW of anti-Stokes signal at 662 nm. This is 3 orders of magnitude greater than what has been reported using a nonresonant CARS sample. Similar efficiencies are obtained over a range for tuning the pump pulse 40 nm close to the ZDW, which corresponds to a 600 cm^{-1} range of pump-Stokes frequency differences. The single-pass gain G_a has significant magnitude, even when λ_p is so that $|\Delta\beta L/2| > \pi/2$. The results are summarized in Fig. 8.14. The inset shows that the anti-Stokes pulse is generated exclusively, without generation of other spectral features.

We note that the generation of a well-defined spectral feature in a PCF without generation of additional features is atypical for pulses of duration of a few picoseconds. PCFs have attracted interest mainly as a means of generating supercontinua. PCF-generated supercontinua are known to be noisy under certain conditions (Dudley and Coen, 2002), when picosecond pumping is used. That particular noise is of no concern here, as it does not arise from FWM.
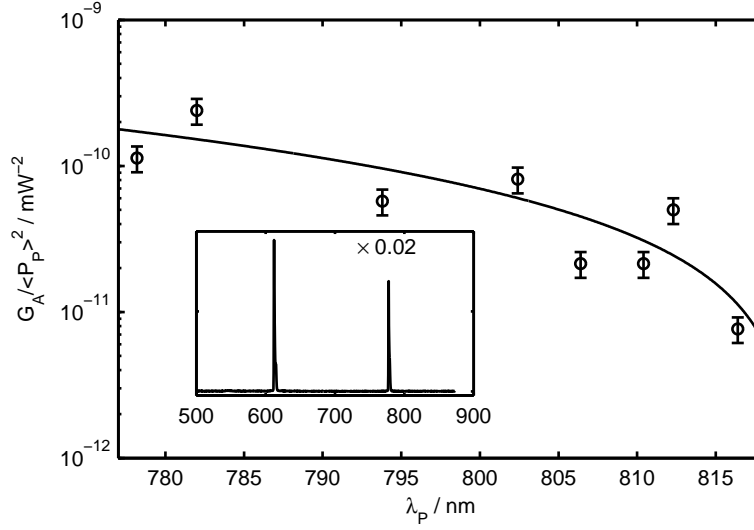
Figure 8.14: Single-pass gain in the PCF normalized to average pump power squared. The solid line is a guide for the eye. The inset shows a representative pump (778 nm) and anti-Stokes (613 nm) spectrum after the PCF. The Stokes at 1064 nm is not shown.

Interferometric CARS microscopy

To demonstrate the utility of the PCF-generated anti-Stokes reference field for CARS microscopy, we record interferometric images of dodecane droplets in water. To demonstrate microscopy, we use a setup that is different from the actively stabilized setup discussed in Sec. 8.3. In this section, we will take advantage of the fact that all three pulses needed for interferometric CARS, pump, Stokes, and reference, exit the PCF spatially and temporally overlapped, and the reference pulse has a specific phase relative to the pump and Stokes, because it is generated from those pulses by FWM. This functions as a passive phase stabilization scheme, so that in this case, active stabilization is not needed. The experimental setup is shown in Fig. 8.15. After the PCF, the pump, Stokes and anti-Stokes reference are collinearly coupled into a laser scanning microscope. A pair of BK7 wedge plates provides a means for tuning Φ due to their group delay dispersion. The CARS signal at the detector is given as:

$$
\begin{aligned}
I_{aS} \quad \propto \quad & 2(\mathrm{Re}\chi_r^{(3)} + \chi_{nr}^{(3)})E_{ref}E_p^2 E_S \cos(\Phi) + 2\mathrm{Im}\chi_r^{(3)} E_{ref} E_p^2 E_S \sin(\Phi) \\
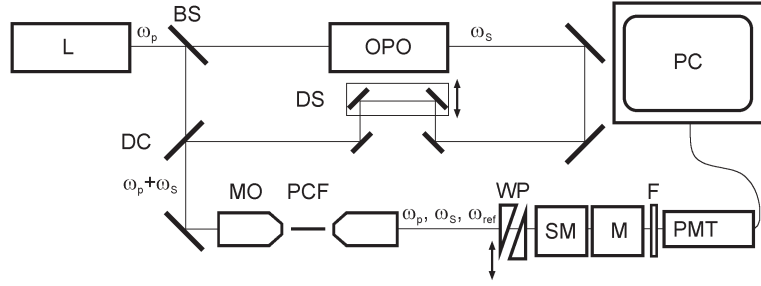& [+\mathrm{non-interferometric\ terms}],
\end{aligned}
$$

Figure 8.15: Experimental setup. L: Laser (PicoTrain, High-Q Lasers); OPO: Optical parametric oscillator (Levante, APE Berlin); BS: Beam splitter; DS: Delay stage; DC: Dichroic mirror; MO: Microscope objective (0.66 NA, Leica Achro 40×); PCF: Photonic-crystal fiber; WP: Wedge prism pair (10°, BK7); M: Microscope (FluoView 300, Olympus).

The wedge prisms introduce an additional delay of 170 to 670 fs between the pump and Stokes, and 120 to 480 fs between the reference and the pump. This is negligible compared to the pulse durations. Changing the wedge position to change Φ by $\pi/2$ changes interpulse delays only by few fs. A similar setup has been reported previously (Hahn and Lee, 1995), in that report, a 10 Hz nanosecond laser system was used, making their setup better suited for CARS spectroscopy of gases than microscopy. Setting the pump wavelength to 816.3 nm and the Stokes to 1064 nm, a Raman shift of 2852 cm^{-1} is selected, coinciding with the CH_2 vibration frequency of dodecane. The CARS signal from the dodecane droplets is predominantly resonant signal, while the surrounding water produces only nonresonant signal. The signal intensity from the dodecane droplet is

$$S \propto |\chi_r^{(3)}|^2 I_p^2 I_S + |E_{ref}|^2 + 2\epsilon \mathrm{Im}\chi^{(3)} E_p^2 E_S E_{ref} \sin \Phi \qquad (8.14)$$

where ϵ is a constant that accounts for imperfect interference between the reference and anti-Stokes fields. It has been assumed that the reference and resonant signals are much stronger than the nonresonant signals so that terms containing $\chi_{nr}^{(3)}$ can be neglected. Fig. 8.16 shows the average interferometric signal from dodecane as a function of the wedge position. The points oscillate around a value slightly higher than 1. This agrees with Eq. 8.14, from which it is expected that the points oscillate around $1 + |\chi_r^{(3)}|^2 I_p^2 I_S^2 / |E_{ref}|^2$. This result underlines that phase coherence between the incident pulses and the anti-Stokes reference generated in the PCF is retained.
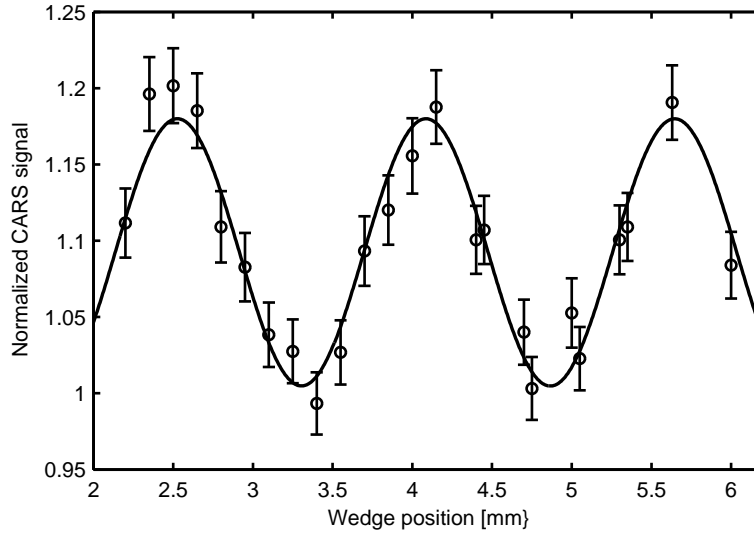
Figure 8.16: Average signal inside a dodecane droplet normalized to average signal in the surrounding water versus wedge position. The solid line is a sinusoidal fit to the points. Errorbars denote estimated inaccuracies.

Images for various settings of Φ are shown in Fig. 8.17. The series of images shows the recurring maxima and minima of the intensity of the central dodecane droplet. The images are reproducible for each position of the wedge, indicating that no phase drift occurs. There is some noise in the images, due to the low power in the sample plane, which again was due to an element in the microscope, which reflected poorly in the NIR.

Possible improvements

Although not used here, the interferometric terms can, in principle, be separated from the non-interferometric terms by using phase modulation of one of the fields combined with lock-in detection (Potma et al., 2006). Although in this case, that is not really practical, because the three beams would have to be split and recombined to do that. Alternatively, the phase modulation could be done by mounting on of the wedge prisms on a shaker, but this would limit the frequency of the phase modulation.

An impediment to the FWM in the PCF was the low quality of the beam profile from both the laser and the OPO. That simply made coupling into the PCF more difficult and less efficient, resulting in an
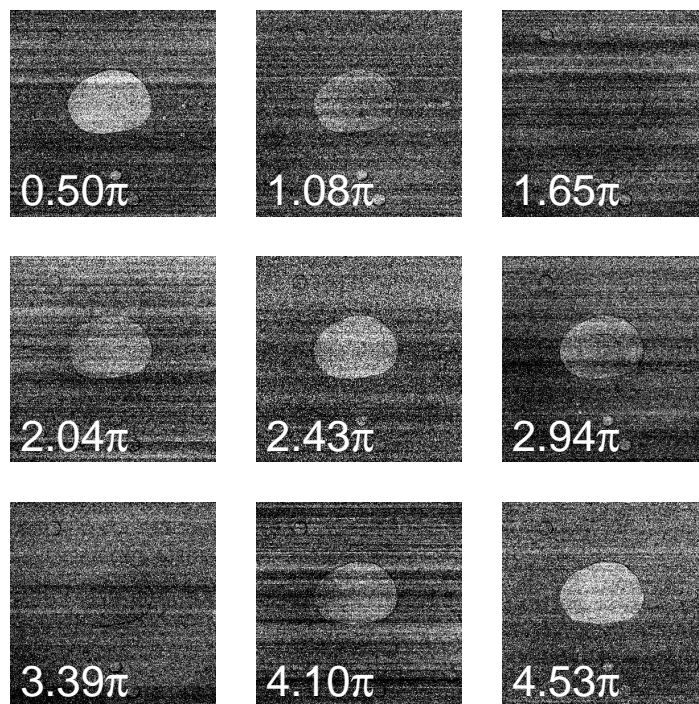
Figure 8.17: Interferometric CARS images of a dodecane droplet in water. The labels denote Φ. Each image is 256×256 pixels or 175×175 μm. Acquisition time was 2.6 s/image. Pump and Stokes powers at the sample were 2.0 and 4.1 mW, respectively.

unnessecarily large heat load and thermal stress on the PCF. This could be a reason for the quite large noise in the measurements.

A significantly wider tuning range could be obtained, if a laser system were employed, where the pump wavelength could be held fixed near the ZDW, while the Stokes wavelength were tuned, as is apparent from Fig. 8.11. In the laser system that was available, this was not possible, the Stokes wavelength was fixed at 1064 nm, the laser wavelength.

It is possible that PCFs are destined for a more prominent role in future optical setups when it comes to picosecond wavelength conversion. If focussing purely on efficient frequency conversion, several improvements can be made compared to the approach detailed above. Sharping et al. (2007) recently succeeded in demonstrating a synchronously pumped OPO based on a short PCF. They achieved 50 mW of converted average power and 200 nm tunability. The converted pulses maintained their short duration.

When pump, Stokes, and anti-Stokes co-propagate in the PCF, the group delay dispersion (GDD) will eventually pull the pulses apart and halt their interaction *i.e.* the FWM process. GDD therefore poses a limitation on the effectiveness of the scheme of PCF-based anti-Stokes generation. In Fig. 8.13, the calculated interpulse delays in the PCF are plotted for fixed pump wavelength at the ZDW. It can be seen that the Stokes and anti-Stokes delays are almost equal. For the present length of the PCF, 16 mm, the pump-Stokes and pump-anti-Stokes interpulse delay is on the order 100 fs, which is negligible compared to the pulse durations.

In time, fiber-optical parametric oscillators (FOPO)s could come to be a viable alternative to bulk picosecond tunable sources, such as Ganikhanov et al. (2006).

Conclusion

In conclusion, we demonstrated that spectrally well-defined wavelength-tunable picosecond pulses at the anti-Stokes wavelength can be efficiently and exclusively generated in a PCF from the pump and Stokes pulses. Phase coherence is retained, which permits a simple form of interferometric CARS microscopy, absent of any phase drift. If required, our simplified scheme can be improved by implementing phase modulation and lock-in detection through mounting one of the wedge prisms on a shaker. Our anti-Stokes generation scheme can also be easily incorporated in a Mach-Zender-type setup for CARS interferometry (Potma et al., 2006), constituting an efficient alternative to the previously used liquid samples for anti-Stokes generation.

Part IV

Summary and perspectives

Chapter 9

Summary and perspectives

9.1 Summary

The aim of this thesis has been to investigate how the special properties of PCFs can be used in creating simple and compact light sources for CARS microspectroscopy.

Two single-laser light sources providing the two excitation beams for CARS microspectroscopy have been realized, the first (i) based on an fs-laser, the second (ii) on a ps-laser. i) is based on a Ti:sapphire fs oscillator at 800 nm running at 76 MHz. It relies on spectral compression of the laser pulse in a PCF to generate a ps pump pulse. The fs Stokes pulse is generated by redshifting the laser pulse in a PCF through SSFS. The spectrally compressed pump significantly improves spectral resolution and signal-to-background ratio in CARS, although its residual chirp makes interpretation of CARS spectra more difficult. With the soliton Stokes pulse, it is possible to cover the entire Raman spectrum, but a problem is that the Stokes power is limited by PCF parameters. ii) is based on a home-built ytterbium ps fiber laser at 1033 nm running at 33.5 MHz. Here, the laser pulse itself is used directly as pump pulse, while the fs Stokes pulse is created by SSFS as in the first setup. This setup provides better spectral resolution than the first one and delivers CARS spectra, that can be interpreted, although the intrinsic limit on the Stokes power also poses a limitation here.

Two results on interferometric CARS microscopy were presented. First, a phase stabilization scheme was presented which does not rely on phase modulation and makes it possible to control the absolute phase between pump and Stokes pulses and a reference pulse. Second, it was demonstrated how FWM in a PCF can generate a ps reference pulse by mixing the ps pump and Stokes pulses, which resulted in reference pulses three orders of magnitude more intense than previously reported

approaches where the reference pulse was generated in highly polariz-
able liquids.

9.2   Perspectives

SSFS

No matter the elegance of the SSFS and its ability to produce tunable,
transform-limited fs pulses over a wide wavelength range, it seems that
the intrinsic limit on the soliton peak power is going to impede the
applicability. Possible routes for increasing the peak power might be to
employ liquid-filled PBG fibers or to make the soliton propagate in a
higher-order transverse mode, which has higher β_2 than the fundamen-
tal mode. Presently, however, the well-defined temporal characteristics
of the redshifted soliton makes it well-suited for time-resolved CARS
measurements (Sidorov-Biryukov et al., 2006).

Continuum generation

Although continuum generation has played no major role in this thesis,
it is possible that PCF-generated continua could come to play a role in
future light sources for CARS microspectroscopy and microscopy. With
pulse shapers (Weiner, 2000) becoming ever more popular as means of
synthesizing complex pulse shapes and phases, it seems plausible that
the fields of continuum generation and pulse shaping could be merged.
Continuum generation could generate the range of frequencies that is
required for CARS. The continuum in Fig. 5.1 for example does so;
it spans approximately 700 nm - 900 nm (≈ 3000 cm^{-1}) and is phase
stable because it is generated by SPM, so a pulse shaper could compen-
sate the nonlinear phase and tailor it to fit as a light source for CARS.
Several possibilities of pulse shaping exist: Selective excitation by a
sinusoidal spectral phase (Dudovich et al., 2002), narrowband probing
by a π-phase gate (Oron et al., 2002), or splitting the continuum into
two pulses and performing the measurement in the time-domain (von
Vacano and Motzkus, 2006).

Fiber-based light sources

So far, most reports about applications of CARS imaging have come
from groups relying on the traditional light sources: Two inter-locked
Ti:sapphire lasers or a ps-laser and an OPO. It seems that CARS imag-
ing itself is still quite challenging, so an optimal light source, rather
than a compact one, is needed. So, as long as fiber-based light sources
can not demonstrate similar performance as traditional light sources,

it is unlikely that they will become wide-spread. The first fiber-based light source to gain some spread is likely to be OPO-based, *i.e.* similar to the one described in Ganikhanov et al. (2006), but with the Nd-laser replaced by a fiber laser. Fiber lasers suitable for that purpose can indeed be made. Further on, it is possible that the OPO also will become fiber-based, taking advantage of the possibility for broadband phasematching in PCFs (Sharping et al., 2007).

Fiber-based frequency-converting elements may still have some potential in CARS imaging setups, although the light source itself might still be a traditional one. Of the PCF-based approaches for frequency conversion described in this thesis, the one deemed most likely to become widespread is the efficient generation of ps reference pulses for interferometric CARS microscopy by FWM in a PCF.

CARS imaging

Most reported applications of CARS in cells have been limited to studies of the orientation, distribution, and transport of water and lipids due to the high concentrations and strong CARS signal given off by these molecules (Potma et al., 2001; Cheng et al., 2003; Kennedy et al., 2005; Li et al., 2005; Nan et al., 2006a). But it should be emphasized, that these applications represent niches that are difficult to address in other ways. Several other reported applications have relied on the combination of CARS microscopy with fluorescence microscopy, second-harmonic genereration, or sum-frequency generation (Wang et al., 2005; Fu et al., 2007; Huff and Cheng, 2007). So at present, studies relying exclusively on CARS imaging seem limited to a select few applications. But with the ability of CARS microscopy to generate images of C-H bonds at video rate (Evans et al., 2005), it could become a useful tool in combination with other imaging techniques. For example, CARS in combination with fluorescence microscopy on a fluorescently labelled cell makes it possible to obtain real-time structural information from the CARS signal, while the fluorescent signal can provide specific information.

It is possible that the interpretation of CARS spectra could improve. For example, the maximum-entropy method for obtaining phase information from CARS spectra has proved quite succesful (Vartainen et al., 2006; Rinia et al., 2006).

More advanced pump and Stokes pulses could also help to increase the potential of CARS imaging. In special cases, frequency-modulation of the pump pulse can eliminate nonresonant signal (Ganikhanov et al., 2006). A generally applicable approach of shaping the pump pulse into a sinc-function can decrease the nonresonant signal in CARS microspectroscopy significantly (Pestov et al., 2007). In CARS microscopy, he-

terodyne-detected CARS (Potma et al., 2006) is a generally applicable method to eliminate nonresonant signal.

In the author's view, the latter two are the most promising routes towards improving the sensitivity of CARS microspectroscopy and microscopy, respectively, because they are generally applicable and provide direct measurements of $|\chi_r^{(3)}|^2$ and $\text{Im}[\chi_r^{(3)}]$, respectively.

9.3 Acknowledgements

Appendix A

List of Abbreviations

Acronym	Abbreviated phrase
CARS:	Coherent anti-Stokes Raman scattering
fs:	Femtosecond
FWHM:	Full width at half maximum
FWM:	Four-wave mixing
GVD:	Group velocity dispersion
HOD:	Higher-order dispersion
MCARS:	Multiplex CARS
NA:	Numerical aperture
NIR:	Near-infrared
OPO:	Optical parametric oscillator
PCF:	Photonic crystal fiber
PM:	Polarization-maintaining
ps:	Picosecond
RWA:	Rotating-wave approximation
S/N:	Signal to noise
SPM:	Self-phase modulation
ZDW:	Zero-dispersion wavelength

Appendix B

Matlab script 1

```
%NLPol.m calculates the nonlinear third-order polarization
%at 2wP-wS with a given third-order susceptibility chi for
%given complex envelopes E_P and E_S.
%Conversion factors: 1cm-1=3e-5fs-1,

%Parameters:
t0=1333;
tau0_P = 64 %TFL FWHM of E_P^2 in fs
Phi2_P = 43000; %2nd-order spectral phase of pump in fs^2
nu_P = 12350; %Freq. of pump in cm-1
tau0_S = 50; %TFL FWHM of E_S^2 in fs
Phi2_S = 0; %2nd-order spectral phase of Stokes in fs^2
nu_S = 9496; %Freq. of Stokes in cm-1
P0_P = 1; %peak power of TFL pump in watts
P0_S = 1; %peak power of TFL Stokes in watts
N=128;%N=2^p
t=linspace(-20000,20000,N*1024); %time axis in fs
nu=N*1024/40000*1/(1024*N)*[(0:512*N) -(512*N-1):-1]; %freq axis
                                                      %in fs-1

%Functions
Gamma_P0 = 1/(0.3607*(tau0_P*sqrt(2))^2);
Gamma_P = Gamma_P0/(1+(2*Gamma_P0*Phi2_P).^2)...
-i*(2*Gamma_P0*Phi2_P)*Gamma_P0/(1+(2*Gamma_P0*Phi2_P).^2);
E_Pt=(sqrt(P0_S*Gamma_P/pi)*exp(-Gamma_P*(t+t0).^2))...
.*exp(i*2*pi*(nu_P*3e-5).*(t-t0));
E_Pt=E_Pt.*exp(i*4700000*conj(E_Pt).*E_Pt);

Gamma_S0 = 1/(0.3607*(tau0_S*sqrt(2))^2);
```

```
Gamma_S = Gamma_S0/(1+(2*Gamma_S0*Phi2_S).^2)...
-i*(2*Gamma_S0*Phi2_S)*Gamma_S0/(1+(2*Gamma_S0*Phi2_S).^2);
E_St=(sqrt(P0_S*Gamma_S/pi)*exp(-Gamma_S*(t).^2))...
.*exp(i*2*pi*(nu_S*3e-5).*(t));

G_n0nu = 1; %Green's function for a virtual level
G_10nu = 1./(nu-0.554/(2*pi)+i*1.14e-3/2) ...
+ 1./(nu-0.532/(2*pi)+i*7.5e-4/2); %Green's functions for real
                                    %levels
G_m0nu = 1; %Green's function for a virtual level

%Calculate consequtively higher orders of the density matrix
%elements:
rhon0_1 = G_n0nu.*fft(E_Pt);
rhon0_1 = ifft(rhon0_1);
rho10_2 = G_10nu.*fft(conj(E_St).*rhon0_1);
rho10_2 = ifft(rho10_2);
rhom0_3 = G_m0nu.*fft(rho10_2.*E_Pt);
rhom0_3 = ifft(rhom0_3);

%...and plot
P3=rhom0_3;
figure;
subplot(2,1,2),plot(t,real(P3));
P3=fft(P3);
subplot(2,1,1);
plot(-nu_P+nu(1:(512*N+1))/3e-5,conj(P3(1:(512*N+1)))...
.*P3(1:(512*N+1)));
spectrum = [-nu_P+nu(1:(512*N+1))/3e-5; conj(P3(1:(512*N+1)))...
.*P3(1:(512*N+1))];
set(gca, 'XLim', [2600 3300]);
E_St=conj(E_St).*E_St;
E_St=E_St/max(E_St);
FWHM_S=t(max(find(E_St>0.5)))-t(min(find(E_St>0.5)))
E_Pt=conj(E_Pt).*E_Pt;
E_Pt=E_Pt/max(E_Pt);
FWHM_P=t(max(find(E_Pt>0.5)))-t(min(find(E_Pt>0.5)))
```

Appendix C

Matlab script 2

```
%Splitfourier.m simulates the propagation of pulses in
%optical fibers by numerically solving the NLSE with
%the split-step Fourier method.

%Definitions
N=2; %N*1024 = size of arrays
tmin=-20000; %time axis in fs
tmax=20000;
t=linspace(tmin,tmax,1024*N);
t=t';
omega=2*pi*1024*N/(tmax-tmin)*[(0:(512*N))/(1024*N) ...
((-512*N+1):-1)/(1024*N)];
omega=omega';
P0=3000*4; %Peak power in W
gamma=0.09; %nonlinearity parameter in W^-1m^-1
E_P0=sqrt(P0);
alpha=0; %Absorption
tau_FWHM=100; %Transform-limited FWHM af |E|^2 in fs
Gamma_P0=1/(0.3607*(tau_FWHM*sqrt(2))^2);
ksix_P=50*4; %a linear chirp parameter, T = 50*ksix_P
beta2=0; %GVD in fs^2/m
beta3=0; %TOD in fs^3/m
beta4=0; %FOD in fs^4/m
Gamma_P=Gamma_P0/(1+ksix_P.^2)-i*ksix_P*Gamma_P0/(1+ksix_P.^2);
E_t=(sqrt(Gamma_P/pi)*exp(-Gamma_P*(t).^2)); %initial condition
E_t=E_P0*E_t/sqrt(max(conj(E_t).*E_t)); %normalize envelope
err=1e-3;    %max error
n_max=500000;  %max steps
q=1; %step counter
```

```
dz=0.0005; %initial guess for stepsize
z_start=0; %startposition i m
z_end=0.001; %slutposition i m
z=z_start;
E_log = [];

%Propagation of the wave packet with Cash-Karp embedded Runge-Kutta
%See NR Sec. 16.2 (p 719);  a,b,c,c* parameters, page 722
%With one pulse only, usually >95% off all steps are accepted!
a=[0, 1/5, 3/10, 3/5, 1, 7/8];
b=[0                0            0            0            0;
    1/5             0            0            0            0;
    3/40            9/40         0            0            0;
    3/10            -9/10        6/5          0            0;
    -11/54          5/2          -70/27       35/27        0;
    1631/55296      175/512      575/13824    44275/110592 253/4096];
c=[37/378; 0; 250/621; 125/594; 0; 512/1771];
cs=[2825/27648; 0; 18575/48384; 13525/55296; 277/14336; 1/4];
dc=c-cs;
k=zeros(length(E_t),6);

while (z<z_end)                        %loop until final position is reached
for p=1:6
    E_t_b=E_t+k(:,1:5)*b(p,:)';
    k(:,p)=dz*(i*gamma*conj(E_t_b).*E_t_b.*E_t_b) ...
+ifft((dz*(i*beta2/2*omega.^2-i*beta3/6*omega.^3 ...
+i*beta4/24*omega.^4).*fft(E_t_b)));
end
D=k*dc;                    %error estimate, NR (16.2.6)
D=sqrt(conj(D).*D);
errmax=max(abs(D));
Dtarget=err.*dz.*k*c;       %error target NR (16.2.9), the allowed
                            %error becomes relative to the increment
Dtarget=sqrt(conj(Dtarget).*Dtarget);
errtarget=max(abs(Dtarget));
if (errmax<errtarget)       %accept the new step?
    E_t=E_t+k*c;            %YES! advance the solution
    z=z+dz;
    dznew=0.9*dz*(errtarget/errmax).^(0.2);   %enlarge the step size,
                                              %to aim for the desired
                                              %precision

    dz=min([dznew 5*dz]);   %not too large strides
    if (z_end-z<dz)
```

```
        dz=z_end-z;            %make sure that we end at the
                               %right time
    end
    disp(['z= ' num2str(z) '; dz= ' num2str(dz) ' ...
errmax= ' num2str(errmax) '; PASS!']);
else                          %NO! reduce step size and
                              %try again
    dznew=0.9*dz*(errtarget/errmax).^(0.25);
    dz=max([dznew 0.1*dz]); %not too small steps
    disp(['z= ' num2str(z) '; dz= ' num2str(dz) ' ...
errmax= ' num2str(errmax) '; FAIL!']);
end
if (z + dz) > (q*z_end/100)
    if (z-dz) < (q*z_end/100)
        q=q+1;
        E_log = [E_log E_t];
    end
end
end

%Plot the results
E_omega=fft(E_t);
Spectrum=conj(E_omega).*E_omega;
figure;
subplot(1,2,1),plot(omega/2/pi/3e-5,Spectrum);
subplot(1,2,2),plot(t,conj(E_t).*E_t);
clear E_t_b a b c cs k D G Dtarget;
```

Appendix D

Bibliography

Agrawal, G. P. (1995). *Nonlinear Fiber Optics*. Academic Press, Inc.

Aguergaray, C., T. Andersen, D. Schimpf, O. Schmidt, J. Rothhardt, T. Schreiber, J. Limpert, E. Cormier, and A. Tünnermann (2007). Parametric amplification and compression to ultrashort pulse duration of resonant linear waves. *Opt. Express 15*(9), 5699–5710.

Andersen, T., D. Hilligsøe, C. Nielsen, J. Thøgersen, K. Hansen, S. Keiding, and J. Larsen (2004). Continous-wave wavelength conversion in a photonic crystal fiber with two zero-dispersion wavelengths. *Opt. Express 12*(17), 4113–4122.

Barbosa, M., I. de Oliveira, and J. Frejlich (2002). Feedback operation for fringe-locked photorefractive running hologram. *Opt. Comm. 201*, 293–299.

Bertie, J. E., M. K. Ahmed, and H. H. Eysel (1989). Infrared intensities of liquids. 5. optical and dielectric constants, integrated intensities, and dipole moment derivatives of h_2o and d_2o at 22 °c. *J. Phys. Chem. 93*, 2210–2218.

Birks, T., J. Knight, and P. Russell (1997). Endlessly single-mode photonic crystal fiber. *Opt. Lett. 22*, 961–963.

Born, M. and E. Wolf (1999). *Principles of Optics*. Cambridge University Press.

Cheng, J.-X., L. D. Book, and X. S. Xie (2001). Polarization coherent anti-Stokes Raman scattering microscopy. *Opt. Lett. 26*(17), 1341–1343.

Cheng, J.-X., S. Pautot, D. A. Weitz, and X. S. Xie (2003). Ordering of water molecules between phospholipid bilayers visulatlized by coherent anti-Stokes Raman scattering microscopy. *Proc. Nat'l. Acad. Sci. 100*(17), 9826–9830.

Cheng, J.-X., A. Volkmer, L. D. Book, , and X. S. Xie (2002). Multiplex Coherent Anti-Stokes Raman Scattering Microspectroscopy and Study of Lipid Vesicles. *J. Phys. Chem. B 106*, 8493–8498.

Denk, W., J. H. Strickler, and W. W. Webb (1990). Two-photon laser scanning fluorescence microscopy. *Science 248*(4951), 73–76.

Denk, W. and K. Svoboda (1997). Photon upmanship: Why multiphoton imaging is more than a gimmick. *Neuron 18*, 351–357.

Dudley, J. M. and S. Coen (2002). Coherence properties of supercontinuum spectra generated in photonic crystal and tapered optical fibers. *Opt. Lett. 27*(13), 1180–1182.

Dudovich, N., D. Oron, , and Y. Silberberg (2002). Single-pulse coherently controlled nonlinear Raman spectroscopy and microscopy. *Nature 418*, 512–514.

Duncan, M. (1984). Molecular discrimination and contrast enhancement using a scanning coherent anti-Stokes Raman microscope. *Opt. Comm. 50*(5), 307–312.

Duncan, M., J. Reintjes, and T. Manuccia (1982). Scanning coherent anti-Stokes Raman microscope. *Opt. Lett. 7*(8), 350–352.

Evans, C., E. Potma, M. Puoris'haag, D. Cote, C. Lin, and X. Xie (2005). Chemical imaging of tissue in vivo with video-rate coherent anti-Stokes Raman scattering microscopy. *Proc. Nat'l. Acad. Sci. 102*(46), 16807–16812.

Evans, C., E. Potma, and X. Xie (2004). Coherent anti-Stokes Raman scattering spectral interferometry: determination of the real and imaginary components of the nonlinear susceptibility $\chi^{(3)}$ for vibrational microscopy. *Opt. Lett. 29*(24), 2923–2925.

Fermann, M., V. Kruglov, B. Thomsen, J. Dudley, and J. Harvey (2000). Self-similar propagation and amplification of parabolic pulses in optical fibers. *Phys. Rev. Lett. 84*(26), 6010–6013.

Freschi, A. and J. Frejlich (1995). Adjustable phase control in stabilized interferometry. *Opt. Lett.*.

Fu, Y., H. Wang, R. Shi, and J. Cheng (2007). Second harmonic and sum frequency generation imaging of fibrous astroglial filaments in ex vivo spinal tissues. *Biophys. J. 92*(9), 3251–3259.

Fu, Y., H. Wang, R. Shi, and J.-X. Cheng (2006). Characterization of photodamage in coherent anti-Stokes Raman scattering microscopy. *Opt. Exp. 14*(9), 3942–3951.

Ganikhanov, F., S. Carrasco, X. S. Xie, M. Katz, W. Seithz, and D. Kopf (2006). Broadly tunable dual-wavelength light source for coherent anti-Stokes Raman scattering microscopy. *Opt. Lett. 31*(9), 1292–1294.

Ganikhanov, F., C. Evans, B. Saar, and X. Xie (2006). High-sensitivity vibrational imaging with frequency modulation coherent anti-Stokes Raman scattering (FM CARS) microscopy. *Opt. Lett. 31*(12), 1872–1874.

Gershgoren, E., A. Bartels, J. Fourkas, R. Tobey, M. Murnane, and H. Kapteyn (2003). Simplified setup for high-resolution spectroscopy that uses ultrashort pulses. *Opt. Lett. 28*(5), 361–363.

Gomes, L., L. Orsila, T. Jouhti, and O. Okhotnikov (2004). Picosecond SESAM-based ytterbium mode-locked fiber lasers. *IEEE J. Quantum Electron. 10*, 129–136.

Gray, M., D. McClelland, M. Barton, and S. Kawamura (1999). A simple high-sensitivity interferometric position sensor for test mass control on an advanced LIGO interferometer. *Opt. Quant. Electron. 31*, 571–582.

Greve, M., B. Bodermann, H. Telle, P. Baum, and E. Riedle (2005). High-contrast chemical imaging with gated heterodyne coherent anti-Stokes Raman scattering microscopy. *Appl. Phys. B 81*, 875–879.

Hahn, J. and E. Lee (1995). Measurement of nonresonant third-order susceptibilities of various gases by the nonlinear interferometric technique. *J. Opt. Soc. Am. B 12*(6), 1021–1027.

Hashimoto, M., T. Araki, and S. Kawata (2000). Molecular vibration imaging in the fingerprint region by use of coherent anti-Stokes Raman scattering microscopy with a collinear configuration. *Opt. Lett. 25*(24), 1768–1770.

Heinrich, C., S. Bernet, and M. Ritch-Marte (2004). Wide-field coherent anti-Stokes Raman scattering microscopy. *Appl. Phys. Lett. 84*(5), 816–818.

Hellerer, T., A. Enejder, , and A. Zumbusch (2004). Spectral focussing: High spectral resolution spectroscopy with broad-bandwidth laser pulses. *Appl. Phys. Lett. 85*(1), 25–27.

Herda, R. and O. Okhotnikov (2004). Dispersion compensation-free fiber laser mode-locked and stabilized by high-contrast saturable absorber mirror. *IEEE J. Quant. El 40*(7), 893–899.

Hopt, A. and E. Neher (2001). Highly nonlinear photodamage in two-photon fluorescence microscopy. *Biophys. J. 80*, 2029–2036.

Horowitz, P. and W. Hill (1989). *Art of Electronics* (2 ed.). Cambridge University Press, New York.

Huff, T. and J. Cheng (2007). In vivo coherent anti-Stokes Raman scattering imaging of sciatic nerve tissues. *J. Microscopy 225*, 544–552.

Husakou, A. V. and J. Herrmann (2002). Supercontinuum generation, four-wave mixing and fission of higher-order solitons in photonic-crystal fibers. *J. Opt. Soc. Am. B 19*(9), 2171–2182.

Inchauspe, C. G. and O. Martinez (1997). Quartic phase compensation with a standard grating compressor. *Opt. Lett. 22*(15), 1186–1188.

Ivanov, A., A. Podshivalov, and A. Zheltikov (2006). Frequency-shifted megawatt soliton output of a hollow photonic-crystal fiber for time-resolved coherent anti-Stokes Raman scattering microspectroscopy. *Opt. Lett.* (22), 3318–3320.

Iwai, H., C. F. Yen, G. Popescu, A. Wax, K. Badizadegan, R. Dasari, and M. Feld (2004). Quantitative phase imaging using stabilized phase-shifting interferometry. *Opt. Lett. 29*, 2399–2401.

Jackson, J. D. (1998). *Classical Electrodynamics.* John Wiley & Sons, Inc.

Jensen, K., R. Larson, S. Bergeson, and E. McCormack (2001). Exploring closed-loop feedback control using experiments in optics. *arXiv:physics*. http://www.citebase.org/cgi-bin/citations?id=arXiv.org:physics/0106091.

Jones, G., D. Marks, C. Vinegoni, and S. Boppart (2006). High spectral-resolution coherent anti-Stokes Raman scattering with interferometrically detected broadband chirped pulses. *Opt. Lett. 31*(10), 1543–1545.

Kano, H. and H. Hamaguchi (2005a). Near-infrared coherent anti-Stokes Raman scattering microscopy using supercontinuum generated from a photonic crystal fiber. *Appl. Phys. B 80*, 243–246.

Kano, H. and H. Hamaguchi (2005b). Ultrabroadband (> 2500 cm^{-1}) multiplex coherent anti-Stokes Raman scattering microspectroscopy using a supercontinuum generated from a photonic crystal fiber. *Appl. Phys. Lett. 86*(12), 121113.

Kano, H. and H. Hamaguchi (2005c). Vibrationally resonant imaging of a single living cell by supercontinuum-based coherent anti-Stokes Raman scattering microscoptroscopy. *Opt. Express 13*(4), 1322–1327.

Kano, H. and H. Hamaguchi (2006a). *In-vivo* multi-nonlinear optical imaging of a living cell using a supercontinuum light source generated from a photonic crystal fiber. *Opt. Express 14*(7), 2798–2804.

Kano, H. and H. Hamaguchi (2006b). Vibrational imaging of a J-aggregate microcrystal using ultrabroadband multiplex coherent anti-Stokes Raman scattering microspectroscopy. *Vib. Spec. 42*, 135–139.

Kee, T., H. Zhao, and M. Cicerone (2006). One-laser interferometric broadband coherent anti-Stokes Raman scattering. *Opt. Express 14*(8), 3631–3640.

Kee, T. W. and M. T. Cicerone (2004). Simple approach to one-laser, broadband coherent anti-Stokes Raman scattering microscopy. *Opt. Lett. 29*(23), 2701–2703.

Kennedy, A., J. Sutcliffe, and J. Cheng (2005). Molecular composition and orientation in myelin figures characterized by coherent anti-Stokes Raman scattering microscopy. *Langmuir 21*, 6478–6486.

Knight, J., J. Arriaga, T. Birks, A. Ortigosa-Blach, W. Wadsworth, and P. Russell (2000). Anomalous dispersion in photonic crystal fiber. *IEEE Phot. Tech. Lett. 12*(7), 807–809.

Knight, J., T. Birks, P. Russell, and D. Atkin (1996). All-silica single-mode optical fiber with photonic crystal cladding. *Opt. Lett. 21*(19), 1547–1549.

Knight, J., T. Birks, P. Russell, and D. Atkin (1997). All-silica single-mode optical fiber with photonic crystal cladding: errata. *Opt. Lett. 22*(7), 484–485.

Koester, H. J., D. Baur, R. Uhl, and S. W. Hell (1999). Ca^{2+} fluorescence imaging with pico- and femtosecond two-photon excitation: Signal and photodamage. *Biophys. J. 77*, 2226–2236.

König, K., T. Becker, P. Fischer, I. Riemann, and K. Halbhuber (1999). Pulse-length dependence of cellular response to intense near-infrared laser pulses in multiphoton microscopes. *Opt. Lett. 24*, 113–115.

König, K., H. Liang, M. Berns, and B. Tromberg (1995). Cell damage by near-ir microbeams. *Nature 377*, 20–21.

König, K., P. So, W. Mantulin, and E. Gratton (1997). Cellular response to near-infrared femtosecond laser pulses in two-photon microscopes. *Opt. Lett. 22*, 135.

Krishnamachari, V., E. Andresen, S. Keiding, and E. Potma (2006). An active interferometer-stabilization scheme with linear phase control. *Opt. Express 14*(12), 5210–5215.

Kubota, H., K. R. Tamura, and M. Nakazawa (1999). Analyses of coherence-maintained ultrashort optical pulse trains and supercontinuum generation in the presence of solition-amplified spontaneous-emission interaction. *J. Opt. Soc. Am. B 16*(12), 2223–2232.

Kwok, C., S. Lee, K. Chow, C. Shu, C. Lin, and A. Bjarklev (2005). Widely tunable wavelength conversion with extinction ratio enhancement using PCF-based NOLM. *IEEE Photon. Tech. Lett. 17*, 2655–2657.

Li, L., H. Wang, and J. Cheng (2005). Quantitative coherent anti-Stokes Raman scattering imaging of lipid distribution in coexisting domains. *Biophys. J. 89*(5), 3480–3490.

Lim, S., A. Caster, and S. Leone (2005). Single-pulse phase-control interferometric coherent anti-Stokes Raman scattering spectroscopy. *Phys. Rev. A 72*, 041803.

Lim, S., A. Caster, O. Nicolet, and S. Leone (2006). Chemical imaging by single pulse interferometric coherent anti-Stokes Raman scattering microscopy. *J. Phys. Chem. B 110*, 5196–5204.

Limpert, J., N. Deguil-Robin, I. Manek-Hönninger, F. Salin, T. Scheiber, A. Liem, F. Röser, H. Zellmer, A. Tünnermann, A. Coujaud, C. Hönninger, and E. Mottay (2005). High-power picosecond fiber amplifier based on nonlinear spectral compression. *Opt. Lett. 30*(7), 714–716.

Limpert, J., T. Gabler, A. Liem, H. Zellmer, and A. Tünnermann (2002). SPM-induced spectral compression of picosecond pulses in a single-mode Yb-doped fiber amplifier. *Appl. Phys. B 74*, 191–195.

Limpert, J., F. Roser, T. Schreiber, and A. Tünnermann (2006). High-power ultrafast fiber laser systems. *IEEE J. Sel. Top. Quant. Electron. 12*(2), 233–244.

Limpert, J., T. Schreiber, T. Clausnitzer, K. Zöllner, H. Fuchs, E. Kley, H. Zellmer, and A. Tünnermann (2002). High-power femtosecond Yb-doped fiber amplifier. *Opt. Express 10*(4), 628–638.

Manoharan, R., K. Shafer, L. Perelman, J. Wu, K. Chen, G. Deinum, M. Fitzmauice, J. Myles, J. Crowe, R. Dasiri, and M. Feld (1998). Raman spectroscopy and fluorescence photon migration for breast cancer diagnosis and imaging. *Photochem. Photobiol. 67*, 15–22.

Marhic, M., N. Kagi, T.-K. Chiang, and L. Kazovsky (1996). Broadband fiber optical parametric amplifiers. *Opt. Lett. 21*(8), 573–575.

Marks, D. and S. Boppart (2004). Nonlinear interferometric vibrational imaging. *Phys. Rev. Lett. 92*(12), 123905.

Marks, D., C. Vinegoni, J. Bredfeldt, and S. Boppart (2004). Interferometric differentiation between resonant coherent anti-Stokes Raman scattering and nonresonant four-wave-mixing processes. *Appl. Phys. Lett. 85*(23), 5787–5789.

Mukamel, S. (1995). *Principles of Nonlinear Optical Spectroscopy*. Oxford University Press.

Müller, M. and J. M. Schins (2002). Imaging the Thermodynamic State of Lipid Membranes with Multiplex CARS Microscopy. *J. Phys. Chem. B 106*, 3715–3723.

Müller, M., J. Squier, C. D. Lange, and G. Brakenhoff (2000). CARS microscopy with folded BoxCARS phasematching. *J. Micr. 197*, 150–158.

Nan, X., E. Potma, and X. Xie (2006a). Nonperturbative chemical imaging of organelle transport in living cells with coherent anti-Stokes Raman scattering microscopy. *Biophys. J. 91*(2), 728–735.

Nan, X., E. O. Potma, and X. S. Xie (2006b). Nonperturbative chemical imaging of organelle transport in living cells with coherent anti-Stokes Raman scattering microscopy. *Biophys. J. 91*, 728–735.

Nielsen, C., B. Ortac, T. Schreiber, J. Limpert, R. Hohmuth, W. Richter, and A. Tünnermann (2005). Self-starting self-similar all-polarization maintaining Yb-doped fiber laser. *Opt. Express 13*(23), 9346–9351.

Oberthaler, M. and R. Höpfel (1993). Special narrowing of ultrashort laser pulses by self-phase modulation in optical fibers. *Appl. Phys. Lett. 63*(8), 1017–1019.

Ogilvie, J., E. Beaurepaire, A. Alexandrou, and M. Joffre (2006). Fourier-transform coherent anti-Stokes Raman scattering microscopy. *OL 31*(4), 480–482.

Oron, D., N. Dudovich, and Y. Silberberg (2002). Single-Pulse Phase-Contrast Nonlinear Raman Spectroscopy. *Phys. Rev. Lett. 89*(27), 273001.

Osvay, K. and I. N. Ross (1999). Efficient tuneable bandwidth frequency mixing using chirped pulses. *Opt. Comm. 166*, 113–119.

Oudar, J.-L., R. W. Smith, and Y. Shen (1979). Polarization-sensitive coherent anti-Stokes Raman spectroscopy. *Appl. Phys. Lett. 34*(11), 758–760.

Ouzounov, D., F. Ahmad, D. Müller, N. Venkataraman, M. Gallagher, M. Thomas, J. Silcox, K. Koch, and A. Gaeta (2003). Generation of megawatt optical solitons in hollow-core photonic band-gap fibers. *Science 301*, 1702–1704.

Pestov, D., R. Murawski, G. Ariunbold, X. Wang, M. Zhi, A. Sokolov, V. Sautenkov, Y. Rostovtsev, A. Dogariu, Y. Huang, and M. Scully (2007). Optimizing the laser-pulse configuration for coherent Raman spectroscopy. *Science 316*, 265–268.

Planas, S., N. P. Manus, C. B. Cruz, and H. Fragnito (1993). Spectral narrowing in the propagation of chirped pulses in single-mode fibers. *Opt. Lett. 18*(9), 699–701.

Potma, E., C. Evans, and X. Xie (2006). Heterodyne coherent anti-Stokes Raman scattering (CARS) imaging. *Opt. Lett. 31*(2), 241–243.

Potma, E. O., W. P. de Boeij, P. J. van Haastert, and D. A. Wiersma (2001). Real-time visualization of intracellular hydrodynamics in single living cells. *Proc. Nat'l. Acad. Sci. 98*(4), 1577–1582.

Potma, E. O., D. Jones, J.-X. Cheng, X. Xie, and J. Ye (2002). High-sensitivity coherent anti-Stokes Raman scattering microscopy with two tightly synchronized picosecond lasers. *Opt. Lett. 11*(10), 659–661.

Press, W. H., S. A. Teukolsky, W. T. Vetterling, and B. P. Flannery (1992). *Numerical Recipes in C* (2 ed.). Cambridge University Press.

Raoult, F., A. Boscheron, D. Husson, C. Sauteret, A. Modena, V. Malka, F. Dorchies, and A. Migus (1998). Generation of narrow-bandwidth picosecond pulses by frequency doubling of femtosecond chirped pulses. *Opt. Lett. 23*(14), 1117–1119.

Richards-Kortum, R. and E. Sevick-Muraca (1996). Quantitative optical spectroscopy for tissue diagnosis. *Annu. Rev. Phys. Chem. 47*, 555–606.

Rinia, H., M. Bonn, and M. Müller (2006). Quantitative multiplex CARS spectroscopy in congested spectral regions. *J. Phys. Chem. B 110*, 4472–4472.

Russell, P. (2003). Photonic Crystal Fibers. *Science 299*, 358–362.

Sakurai, J. (1994). *Modern Quantum Mechanics*. Addison Wesley Publishing Company.

Schreiber, T., T. Andersen, D. Schimpf, J. Limpert, and A. Tünnermann (2005). Supercontinuum generation by femtosecond single and dual wavelength pumping in photonic crystal fibers with two zero dispersion wavelengths. *Opt. Express 13*, 9556–9569.

Sharping, J., M. Fiorentino, A. Coker, and P. Kumar (2001). Four-wave mixing in microstructure fiber. *Opt. Lett. 26*(14), 1048–1050.

Sharping, J., M. Foster, A. Gaeta, J. Lasri, O. Lyngnes, and K. Vogel (2007). Octave-spanning, high-power microstructure fiber-based optical parametric oscillators. *Opt. Express 15*(4), 1474–1479.

Sidorov-Biryukov, D., E. Serebryannikov, and A. Zheltikov (2006). Time-resolved coherent anti-Stokes Raman scattering with a femtosecond soliton output of a photonic-crystal fiber. *Opt. Lett. 31*(15), 2323–2325.

Stolen, R. and C. Lin (1978). Self-phase-modulation in silica optical fibers. *Phys. Rev. A 17*(4), 1448–1453.

Vartainen, E., H. Rinia, M. Müller, and M. Bonn (2006). Direct extraction of Raman line-shapes from congested CARS spectra. *Opt. Express 14*(8), 3622–3630.

Veitas, G. and R. Danielius (1999). Generation of narrow-bandwidth tunable picosecond pulses by difference-frequency mixing of stretched pulses. *J. Opt. Soc. Am. B 16*(9), 1561–1565.

von der Linde, D. (1985). Characterization of the noise in continuously operating mode-locked lasers. *Appl. Phys. B 39*, 201–217.

von Vacano, V. and M. Motzkus (2006). Time-resolved two color single-beam cars employing supercontinuum and femtosecond pulse shaping. *Opt. Comm. 264*, 488–493.

Wabnitz, S. (2006). Broadband parametric amplification in photonic crystal fibers with two zero-dispersion wavelengths. *J. Lightwave Tech. 24*(4), 1732–1738.

Wang, H., Y. Fu, P. Zickmund, R. Shi, and J. Cheng (2005). Coherent anti-Stokes Raman scattering imaging of axonal myelin in live spinal tissues. *Biophys. J. 89*(1), 581–591.

Washburn, B. R., J. A. Buck, and S. E. Ralph (2000). Transform-limited spectral compression due to self-phase modulation in fibers. *Opt. Lett. 25*(7), 445–447.

Weiner, A. (2000). Femtosecond pulse shaping using spatial light modulators. *Rev. Sci. Instrum. 71*, 1929–1960.

Zhang, A. and M. Demolan (2005). Broadband wavelength converter based on four-wave mixing in a highly nonlinear photonic crystal fiber. *Opt. Lett. 30*(18), 2375–2377.

Zhu, X., J.-F. O. Cormier, and M. Piche (1996). Study of dispersion compensation in femtosecond lasers. *J. Mod. Opt 43*(8), 1701–1721.

Zumbusch, A., G. R. Holtom, and X. S. Xie (1999). Three-Dimensional Vibrational Imaging by Coherent Anti-Stokes Raman Scattering. *Phys. Rev. Lett. 82*(20), 4142–4145.